FINAL SCIENTIFIC REPORT

TO: OFFICE OF NAVAL RESEARCH GLOBAL

GRANT NO. __N62909-16-1-2079_,

SCIENTIFIC REPORT

FOR THE PERIOD ___April 30, 2016- May 1, 2020_____

RESEARCH TITLE:

Single-Element Passive Time Reversal Mirror in Shallow Water Acoustics

PRINCIPAL INVESTIGATOR(S) *(name, department, institute*)

Boris Katsnelson, Dept of Marine Geosciences, University of Haifa

COOPERATING INVESTIGATOR(S) *(name, department, institute)*

Publications resulting from the research

a. Number of papers:

Published or accepted for publication: ___7____

Submitted: _____

In preparation: __2_____

b. List of published/accepted papers

1. Godin O. A., B. G. Katsnelson, Jixing Qin, M. G. Brown,N. A. Zabotin, and Xiaoqin Zang . Application of Time Reversal to Passive Acoustic Remote Sensing of the Ocean (2017). Acoustical Physics, Vol. 63, No. 3, pp. 309–320
2. Qin J., Katsnelson B., Godin O., Zhenglin Li (2017) Geoacoustic Inversion Using Time Reversal of Ocean Noise Chinese Physics Letters 34(9):094301
3. Tsuwei Tan, O.Godin, A.Lefebvre, W.Beaute, B.Katsnelson, M.Yarina (2018) Characterization the seabed by using noise interferometry and time warping. POMA, v.35, 070001.
4. Katsnelson B., V.Grigorev., J.Lynch (2018) Variability of phase and amplitude fronts due to horizontal refraction in shallow water The Journal of the Acoustical Society of America v.143, 193-208
5. Godin, O. A., Katsnelson, B Tan, T. W., (2019) Normal mode dispersion and time warping in the coastal ocean. The Journal of the Acoustical Society of America 146(3): EL205-EL211
6. Tan, T. W., Godin, O. A., Katsnelson, B., & Yarina, M (2020) "Passive geoacoustic inversion in a dynamic environment on a continental shelf" JASA EL, EL453-EL4596
7. Katsnelson B., O.Godin, Qianchu Zhang (2020) Observations of Acoustic Noise Bursts Accompanying Nonlinear Internal Gravity Waves on a Continental Shelf off New Jersey. (Accepted for Journal of Geophysical Research, Oceans).

c. Meeting abstracts

1. Katsnelson B. Spatio-temporal fluctuations of the sound signals in shallow water in the presence of variable bathymetry. Conf: “Acoustic and environmental variability, fluctuations and coherence”. Cambridge, England, 12-13 Dec, 2017

2. Katsnelson B., Zhongtao Hu. (2017) Sound field in a coastal wedge in area of thermocline's contact with bottom. Proceedings of II Conference on Acoustics, N-Novgorod, Russia, 6-9 June,
3. Katsnelson B., A.Lunkov (2017) Mode coupling and redistribution of the sound intensity over depth at download propagation, in the area of thermocline contact with bottom. Acoustics'17, Boston, JASA, v.141, No.5, Pt.2, P.3487
4. Katsnelson. B. (2017) Variability of the sound field interference pattern due to horizontal refraction in shallow water. Acoustics'17, Boston, JASA, v.141, No.5, Pt.2, P.3657
5. Tan T., O. A. Godin, A. Lefebvre, W. Beaute, B. G. Katsnelson, and M. Yarina, "Characterizing the seabed by using noise interferometry and time warping," in Proceedings of 176 Meetings on Acoustics ASA, 2018, vol. 35, no. 1: ASA, p. 070001.
6. Tan T. W., O. A. Godin, B. Katsnelson, and M. Yarina, "Passive acoustic characterization of the ocean bottom using a horizontal array of hydrophones," The Journal of the Acoustical Society of America, vol. 144, no. 3, pp. 1973–1974, 2018.
7. Yarina M., B. Katsnelson, J. Qin, O. A. Godin, and T. W. Tan, "Geoacoustic inversion using cross correlation function of low-frequency ambient noise in the Shallow Water 2006 Experiment," The Journal of the Acoustical Society of America, vol. 144, no. 3, pp. 1973–1973, 2018.
8. Katsnelson B, OA Godin, Q Zhang (2019) Variations of Acoustic Noise Intensity Accompanying Internal Wave Soliton. OCEANS 2019-Marseille, 1-4
9. Katsnelson B., O. A. Godin, Qianchu Zhang (2019), Strong variations of the acoustic noise spectra accompanying internal wave solitons. Proceedings UACE 2019, Greece, p.391-396
10. Katsnelson B., O. A. Godin, Qianchu Zhang (2019) Physical mechanisms of generation of the noise bursts associated with nonlinear internal tides in shallow water. 178th Meeting ASA, The Journal of the Acoustical Society of America 146 (4), 2986-2986
11. Katsnelson B., O. A. Godin, Qianchu Zhang (2019) Variations of acoustic noise intensity accompanying internal wave solitons. 177th Meeting ASA, J. Acoust. Soc. Am., Vol. 145, No. 3, Pt. P.1670
12. Katsnelson B., O.A.Godin, Tsu Wei Tan, A.Malykhin (2019) Time warping and acoustic characterization of the seafloor in horizontally inhomogeneous ocean. 177th Meeting ASA, J. Acoust. Soc. Am., Vol. 145, No. 3, Pt. P.1770

13. Yarina M., B. Katsnelson, (2019) Mode Selection of Wideband Acoustic Signals Using Time-Frequency (Warping) Analysis for Single Hydrophone. Comparison with Array Filtering in Variable Medium: 2019 IEEE International Conference (COMCAS)
14. Tan Tsu Wei, O. A. Godin, B. Katsnelson, M. Yarina (2019) Using ambient noise to evaluate the acoustic Green's function for a passive geoacoustic inversion in a dynamic shallow-water environment. 177th Meeting ASA, J. Acoust. Soc. Am., Vol. 145, No. 3, Pt. P.1670
15. Godin O., B.Katsnelson, Tsu Wei Tan (2019) Application of the time-warping transform for separation of acoustic normal modes in horizontally inhomogeneous waveguide. 26th Congress on sound and vibration, Montreal, 2019

B.

Summary of results & achievements

In given period the following research was carried out:

i. Within the framework of application of Time Reversal Mirror (TRM) to noise cross correlation function (CCF) for experiments were used: data of the Florida strait (FS) experiment, carried in shallow water area and experiment Shallow Water 2006 (SW06), carried out on the NJ shelf of USA. In the FS experiment there were three single hydrophones for records of noise. CCFs for two pairs of receivers were used as object for TRM methodology, results demonstrate realistic values of sediment parameters and good enough agreement with other authors. In experiment SW06 data processing and analysis of the noise signals recorded by single hydrophones (SHRUs) and HVLA array (SHARK) in Shallow Water 2006 experiment was done. The main goals of data processing are Cross Correlation Function (CCF) and Autocorrelation function (ACF) which were obtained using different parameters of data processing algorithms. Below some results for calculation of CCF and ACF using model and real data are presented. On the base of CCF TRM methodology was applied for estimation of waveguide parameters. Numerical simulations are firstly performed, in which strong focusing occurs in the

vicinity of one hydrophone when Green's function (GF) is back-propagated from the other hydrophone, with the position and strength of the focus being sensitive to sound speed and density in the bottom.

We next extracted the GF from the noise cross-correlation function measured by two hydrophones with 8025-m distance in the Shallow Water '06 experiment. After realizing the TRM process, sound speed and density in the bottom are inverted by optimizing focusing of the back-propagated GF. Parameters of sediment are in agreement with direct measurements (where this comparison was possible). Results were published in Chinese Phys.Letters 2017 and Acoustical Physics, 2017.

ii. New methodology used for data processing and analysis of CCF is the so called Warping Transform (WT) which allow us to carry out effective mode filtering of wideband signal using single hydrophone only. Demonstration of effectiveness of WT is carried out for experimental data obtained on the SWARM'95 experiment which was conducted in NJ shelf (the same place as SW06). It is shown that effect of horizontal refraction (focusing/defocusing in horizontal plane in the presence of nonlinear internal waves) can be registered and estimated quantitatively using only single hydrophone. Mode filtering using vertical line array gives the same results. Results were presented at IEEE COMCAS conference and published in the corresponding IEEE issue.

iii. Simple, analytically solvable models of normal mode propagation in the coastal ocean are developed and applied to study the effect of the seafloor bathymetry on modal travel times. Within the adiabatic approximation, horizontal inhomogeneity of the waveguide is found to change the modal dispersion curves in a way that helps separation of the modal components of the acoustic field using the time-warping transform. It is shown that moderate seafloor slopes can lead to surprisingly large errors in retrieved geoacoustic parameters and cause a positive bias in bottom sound speed estimates if horizontal refraction is ignored. Results were published in JASA EL, 2019.

iv. Empirical Green's functions are obtained for 31 paths in a highly dynamic coastal ocean by cross-correlation of ambient and shipping noise recorded in the Shallow Water 2006 experiment on a horizontal line array and a single hydrophone about 3600m from the array. Using time warping, group speeds of three low-order normal modes are passively measured in the 10–110Hz frequency band and inverted for geoacoustic parameters of the

seabed. It is demonstrated that, despite very strong sound speed variations caused by nonlinear internal waves, noise interferometry can be successfully used to acoustically characterize the seafloor on a continental shelf. Results were published in JASA EL, 2020.

v. As one more manifestation of the noise in shallow water, anomalously large, transient fluctuations of acoustical noise intensity (up to four-five orders of magnitude above the background in a wide frequency band) were observed with single-hydrophone receiver units (SHRUs) and on the L-shaped horizontal and vertical line array of hydrophones (HVLA) “Shark” (belonging to Woods Hole Oceanographic Institution) in the Shallow Water 2006 experiment. The present study investigated temporal and spatial properties of these noise bursts. The site of the experiment (the New Jersey Atlantic shelf) is characterized by strong internal gravity wave activity, including tidally generated nonlinear internal waves (NIWs). As NIWs move from the shelf break towards the coast, they form trains consisting of up to twelve separate, localized, soliton-like waves with up to 25–35 m displacement of isopycnal surfaces. The NIW trains consecutively cross the positions of five SHRUs and the HVLA Shark that are located about 5–8 km from each other along a line perpendicular to the coast. We found that the bursts of acoustic noise were observed when an NIW train passed through locations of the corresponding acoustic receivers. Turbulence of the water flow, saltation and bedload of marine sediments were the dominant causes of the acoustic noise bursts caused by NIWs at different frequency bands. On near-bottom hydrophones, the most energetic part of the observed noise bursts was generated by collisions of suspended sediment particles with each other, the sensor, and the seafloor. Results were directed to Journal of geophysical Research.

vi. Some 3D effect in shallow water waveguide was discovered using data of SW06. The variability of the interference pattern of a narrow-band sound signal in a shallow water waveguide in the horizontal plane in the presence of horizontal stratification, in particular due to linear internal waves, is studied. It is shown that lines of constant phase (a phase front) and lines of constant amplitude/envelope (an amplitude front) for each waveguide mode may have different directions in the spatial vicinity of the point of reception. The angle between them depends on the waveguide's parameters, the mode number, and the sound frequency. Theoretical estimates and data processing methodology for obtaining

these angles from experimental data recorded by a horizontal line array are proposed. The behavior of the angles, which are obtained for two episodes from the Shallow Water 2006 (SW06) experiment, show agreement with the theory presented. Results were published in JASA, 2018.

TABLE OF CONTENTS

I. APPLICATION OF TIME REVERSAL TO PASSIVE ACOUSTIC REMOTE SENSING OF THE OCEAN

In this chapter we combine, following (Roux and Kuperman, 2005) signal processing techniques based on noise interferometry (NI) and time-reversal mirrors (TRM), and we show that the combined use of these techniques allows purely passive measurements of ocean ambient noise to be used as the basis for ocean acoustic remote sensing. The first signal processing technique employed here is to compute, from concurrent measurements of ocean ambient noise at locations *A* and *B*, the *A*-*B* noise cross-correlation function (NCCF), which yields and approximation to the transient acoustic Green's function $G_{AB}(t)$ that describes propagation from *A* to *B* (Lobkis et al, 2001, Wapenaar, 2004, Godin, 2006). ($G_{BA}(-t)$ is also recovered (Godin, 2006), but reciprocity violation is not exploited here.)

In the second processing step employed here the NCCF is time-reversed and back-propagated from location *B*, thereby producing a focus at location *A*. This process is often described as implementation of a time-reversal-mirror (TRM); TRMs have been extensively used in active source experiments for a variety of applications in underwater acoustics (Jackson et al, 1991, Kuperman et al, 1998, Kim et al, 2001, Zverev et al, 2008)
and other fields (Fink, 1992). A large diversity of paths is desirable in TRM applications because increasing path diversity leads to a sharpening of the focus in the back-propagated field at the original source point and a reduction of spurious focal side lobes [Kim et al, 2001, Fink, 1992). The earlier work combining NI and TRMs (Roux et al, 2005) was performed in and environment in which the range-to-depth ratio was small and the ray path geometry was very simple. In that work path diversity was achieved by making use of measurements on a vertical array. In contrast, in our work only two receivers are used in an environment in the Florida Straits in which the range-to-depth ratio is large; path diversity is achieved due to the many multipaths connecting the two receivers.

In the third processing step employed here, we address the inverse problem by searching over a suitable environmental model parameter space to find the combination of model parameters that optimally focuses the back-propagated sound field at receiver location *A*. We apply the three-step signal processing technique to the ambient noise recorded at two locations in 100 meter-deep water in the Straits of Florida (Brown et al, 2014, Godin et al, 2014).

Beside in the following paragraphs experiment Shallow Water O^ will be analyzed, where set of single hydrophones (SHRUs) and hydrophones on vertical/Horizontal line array (SHARK) will be used for calculation of the cross correlation function (CCF).

1.1 Florida strait experiment

In this Section we first motivate the feasibility of implementing a single-element TRM using full-wave numerical simulations. We then investigate time-reversal and back-propagation of the

NCCFs that were measured in the Straits of Florida. Next paragraph presents the results of using a single-element passive TRM for remote sensing of seafloor at the site of the Florida Straits experiment.

A. Numerical simulations of a single-element time-reversal mirror

In this work, acoustic fields due to a point source in an oceanic waveguide are modeled in the source-receiver vertical plane assuming that the environment is translationally invariant with respect to the transverse horizontal coordinate. Acoustic pressure is first calculated in the frequency domain in a wide-angle parabolic approximation using the code RAM developed by M. D. Collins (Collins et al, 1996). Subsequently, time-domain acoustic pressure $p(x, z, t)$ is Fourier-synthesized from the frequency-domain results $P(x, z, \omega)$. Numerical back-propagation of an acoustic field $p_1(t)$ is implemented by multiplying the results $P(x, z, \omega)$ of RAM calculations by the complex conjugate of the spectrum of $p_1(t)$.

Figure 1 shows the results of a numerical simulation of a single-element acoustic TRM in a shallow-water waveguide. In this simulation, the waveguide is a 100 m deep water layer between a free surface and the ocean bottom, which is modeled as a fluid half-space with higher sound speed c_b = 1750 m/s and density $\rho_b = 1.9\ \rho_w$ than the sound speed c_w = 1537.4 m/s and density ρ_w of seawater. Sound attenuation in the bottom is α_b = 0.3 dB/wavelength. The waveguide parameters and geometry of the problem were chosen to approximate those encountered in a recent noise interferometry experiment in the Straits of Florida (Brown et al, 2014, Godin et al, 2014).

The wave field generated by a near-bottom point source in water is propagated to a point either 5.015 km or 9.760 km away, time-reversed, and propagated in the opposite direction. Figure 1 shows the peak intensity I, which is defined as the maximum in time of the amplitude of the acoustic pressure p on a dB scale: $I(x,z) = 20\log_{10} E$, where $E = \max_{t>0} \left| p(x,z,t)/p_0 \right|$, p_0 is an arbitrary normalization constant, z is depth, and x is the horizontal coordinate in the vertical plane through the sound source and the TRM. The peak intensity of the back-propagated field has a strong maximum at the source position and weaker additional maxima; the undesirable additional maxima become less pronounced with increasing signal bandwidth and horizontal separation of the TRM from the source (Fig. 1.1).

In an unbounded homogeneous environment, a single-element TRM generates a spherical wave, and no focusing occurs anywhere. It is remarkable that a single-element TRM is sufficient to focus the back-propagated field at the source in a shallow-water oceanic waveguide. The physics behind this result becomes clear if one recalls that the wave field due to a point source in the waveguide can be represented as the field in a homogeneous environment due to the actual source and a linear array of image sources, which describe the waves reflected from the waveguide's boundaries.

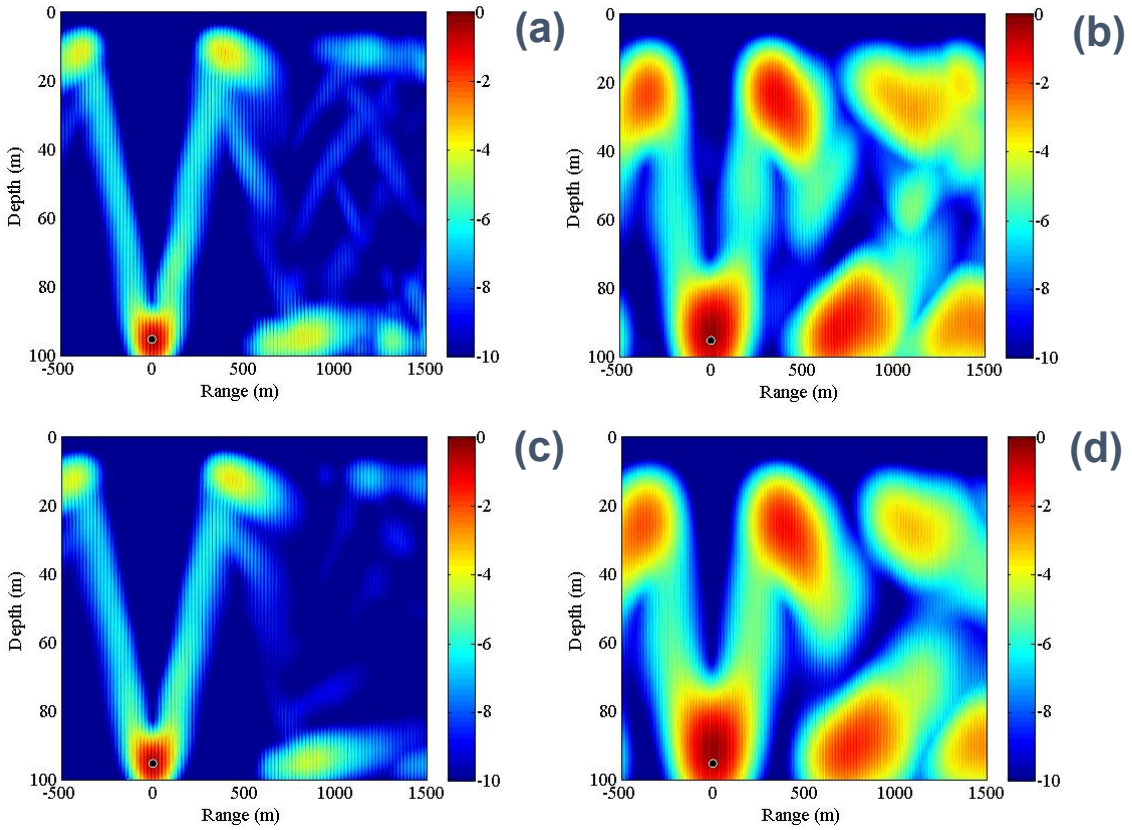

Fig. 1.1. Numerical simulation of a single-element time-reversal mirror (TRM) in a shallow-water waveguide. Peak intensity of the back-propagated acoustic field in the vertical cross-section of the waveguide is shown on a logarithmic scale. The intensity is normalized by its maximum value in each panel. The signal received by the TRM is modeled as the field of a compact source located at zero range and 95 m depth. The TRM is located at the same depth at the band 20–200 Hz [panels **(a)** and **(c)**] or 20–70 Hz [panels **(b)** and **(d)**]. The source-to-TRM range is 5.015 km in panels **(a)** and **(b)**, and 9.760 km in panels **(c)** and **(d)**.

Under conditions of the Florida Straits experiment, at least 10 and 20 surface reflections contribute significantly to the field 5.0 and 9.8 km from the source, respectively [17]. Hence, a single-element TRM in the waveguide operates much like multi-element TRM in an unbounded homogeneous environment.

In practice, the physical parameters that define an oceanic waveguide, which are necessary for calculating the back-propagated field, are known only approximately. A mismatch between the actual waveguide parameters and the parameters assumed in back-propagating a time-reversed signal shifts and blurs the main focus, while making the spurious additional foci more pronounced (Fig. 1.2b–e) as compared to the no-mismatch case (Fig. 1.2a). To better reveal the position and spatial structure of the back-propagated field foci, the quantity $J(x,z) = -10\log_{10}\left(1 - 0.99\,E(x,z)/E_0\right)$, where $E_0 = \max\limits_{x,z} E(x,z)$, is shown in Fig. 2. The

normalized peak intensity J takes values from 0 at the field nodes to 20 in the main focus. We model the seafloor as a sediment layer of thickness h = 20 m with the sound speed c_s = 1550 m/s and density $\rho_s = 1.3\rho_w$ overlaying a half-space with c_b = 1800 m/s and density $\rho_b = 2.2\ \rho_w$. The acoustic attenuation in the bottom is $\alpha_s = \alpha_b$ = 0.1 dB/wavelength. Numerical simulations show that the shift of the main focus from the source position is sensitive to mismatches in the sediment layer sound speed (Figs. 2b, c) and the water column sound speed. There is also some, albeit smaller, sensitivity to variations of the bottom density (Figs. 1.2d, e). The simulations suggest that waveguide parameters can be determined from the requirement that the TRM focuses the wave field at the position of the sound source or, by extension, of the virtual source created through noise interferometry.Of course, the simple simulations described above do not account for the many uncertainties and complications that are present in field experiments. To investigate feasibility of time-reversal of NCCFs of acoustic noise in the ocean, we use the data obtained in the noise interferometry experiment in the Straits of Florida [17, 18]. In this experiment, ambient noise on the continental shelf in the Florida Straits was continuously recorded for 6 days by three autonomous systems. The systems were deployed in December 2012 approximately along the 100 m isobath 15 km off the Florida Keys. The horizontal separations between instruments were 5.01± 0.02 km and 9.76 ± 0.02 km for the 1–2 and 2–3 instrument pairs, respectively. Seafloor slope perpendicular to the paths between the instruments was of the order of 10^{-2}. Each system had a single hydrophone, which was located 5 m off the seafloor. During the experiment, tides with a total range of about 1 m were recorded by a tide gauge. Temperature variations with depth and sound speed gradients were rather weak, with the sound speed c = 1537.4 ± 2.4 m/s throughout the water column [17, 18]. Tidally induced ocean-depth variations lead to a loss of coherence between the noise sampled by the hydrophones, with the effect increasing exponentially with sound frequency [17]. Therefore, only the low-frequency part of the noise spectrum below about 80 Hz proved to be useful for noise interferometry.

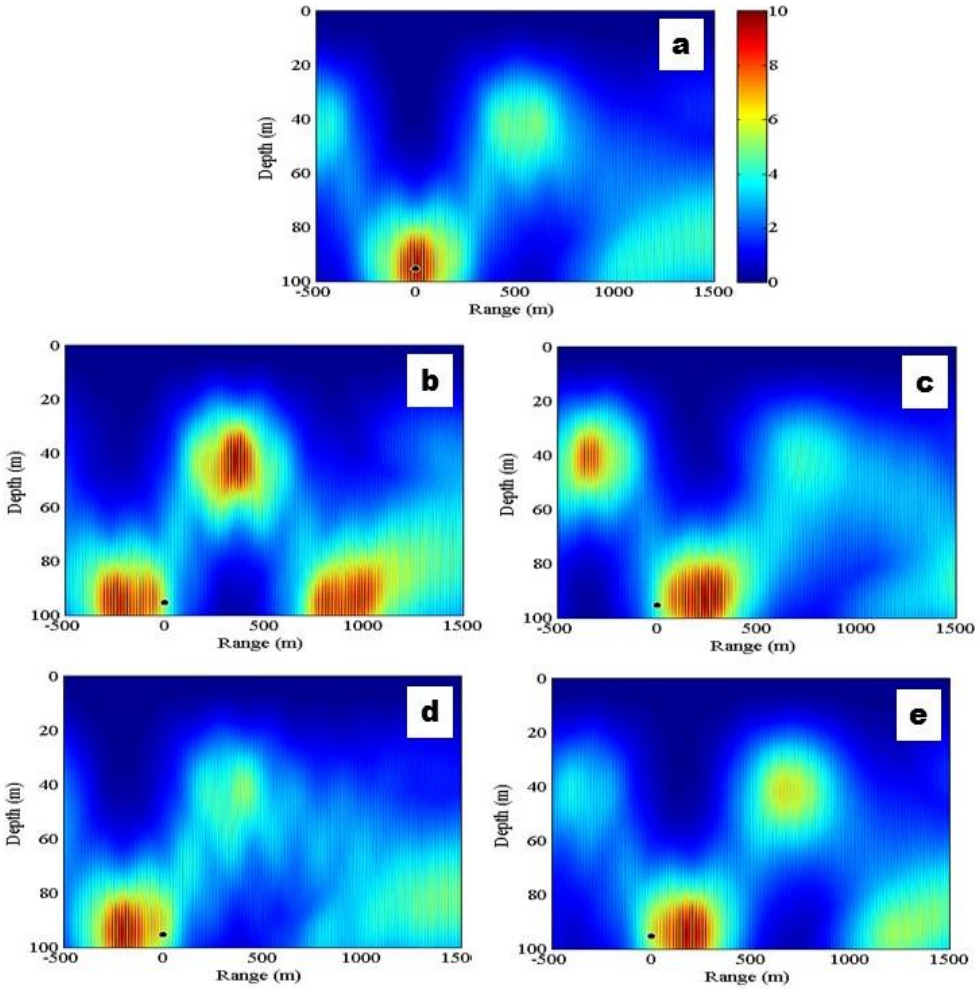

Fig. 2. Sensitivity of the peak intensity of the back-propagated field to geoacoustic parameters in a coastal ocean. The normalized peak intensity of the back-propagated acoustic field in the vertical cross-section of the waveguide is shown for five different seafloor models. The sediment layer sound speed c_s and density ρ_s are: **(a)** 1550 m/s and $1.3\rho_w$; **(b)** 1540 m/s and $1.3\rho_w$; **(c)** 1560 m/s and $1.3\rho_w$; **(d)** 1550 m/s and $1.2\ \rho_w$; and **(e)** 1550 m/s and $1.4\ \rho_w$. The signal received by the single-element TRM is modeled as the field of a compact source located at the point shown by a black circle in the waveguide with c_s = 1550 m/s and $\rho_s = 1.3\rho_w$. The source frequency band is 20–70 Hz; the source-to-TRM range is 5.015 km. Note shifts of the focus of the time-reversed field from the sound source position in panels **(b)** – **(e)**.

B. Noise interferometry experiment

The cross-correlation functions of ambient and shipping noise in the Straits of Florida were evaluated by averaging over a large number of data segments [17, 18]. The relative drifts of clocks between instruments 1 and 2 and instruments 2 and 3 were determined as in Ref. 18 and removed before averaging. Simultaneous measurements of pressure fluctuations on each instrument were split into non-overlapping segments of 625 s duration. About 800 data segments were available

for each instrument. Several data-processing steps were taken to make the noise field more diffuse, as opposed to the field dominated by a few localized noise sources. To suppress contributions of strong, transient sources, we excluded the data segments, in which the noise level exceeded the average level by more than two standard deviations. To further equalize contributions of various sources and to suppress the effects of a rapid variation of the noise power spectrum with frequency, the noise spectra were pre-whitened and normalized in each data segment [17, 18]. This is equivalent to evaluating NCCF as a Fourier transform of the noise coherence function, rather than the cross-spectrum [21].

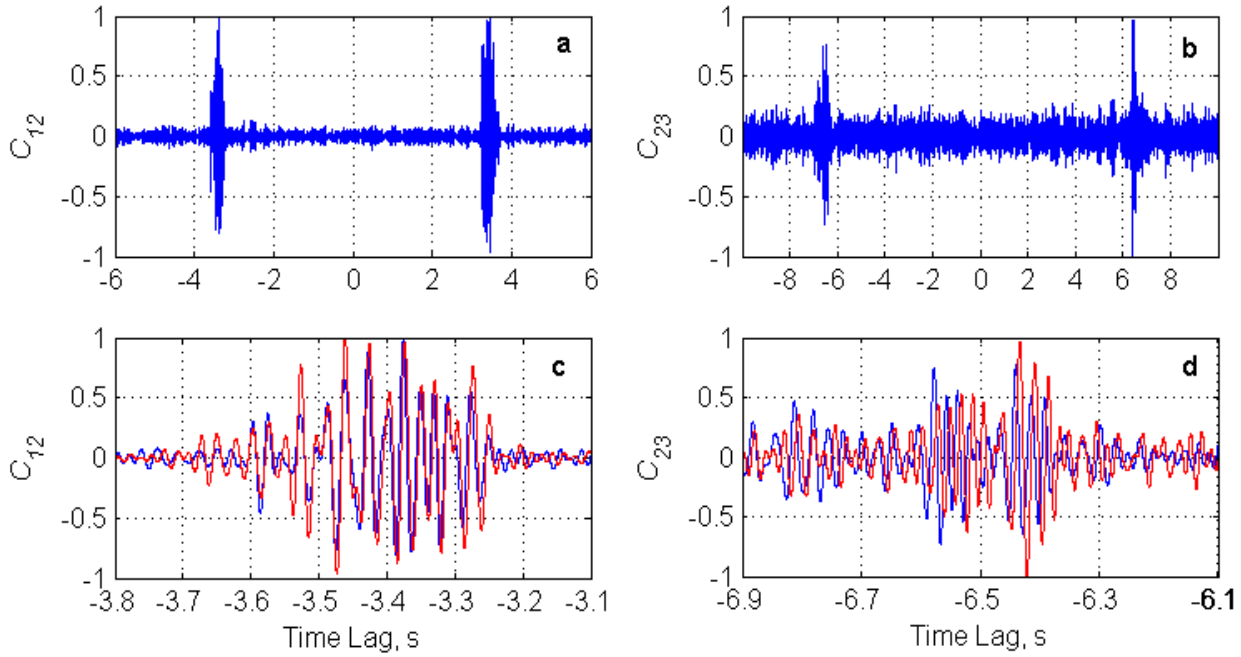

Fig. 1. 3. Cross-correlation functions of ambient noise in the Straits of Florida. **(a)** Measured cross-correlation functions $C_{12}(t)$ for the 1-2 instrument pair in the 20–70 Hz frequency band. **(b)** Same as **(a)** but for the 2-3 instrument pair. **(c)** Fine structure of the cross-correlation function $C_{12}(t)$ at negative time delays (blue) and of the time-reversed cross-correlation function $C_{12}(-t)$ at $t > 0$ (red). **(d)** Same as **(c)** but for the 2-3 instrument pair.

Figure 3 shows measured NCCFs for the 1–2 and 2–3 instrument pairs. Deterministic components of the NCCFs, which approximate the Green's functions, are manifested as large peaks around the time delays of ±3.4 s and ±6.6 s for the 1–2 and 2–3 instrument pairs, respectively (Figs. 3a, b). The difference between the fine structures of the NCCFs at positive and negative time delays (Figs. 3c, d) can be attributed to the noise directivity in the vertical plane being different at propagation in opposite directions between the instruments. In addition to these "signals," the NCCFs contain random "noise" (Figs. 3c, d) because of the finite averaging time.

The “noise” also contributes to slight deviations of the NCCF from being an even function of the time delay t. As expected [22, 23], the signal-to-noise ratio decreases with increasing range.

C. Passive time-reversal mirror

To realize a passive TRM, one numerically back-propagates either the negative time-delay part of NCCF $C_{ij}(t)$ from hydrophone j toward hydrophone i or the time-reversed positive time-delay part of $C_{ij}(t)$ from hydrophone i toward hydrophone j. With passive TRM, there is no compact sound source the wave field of which is being time-reversed. Instead, the hydrophone j serves as a virtual source.

Back-propagation of measured $C_{12}(t)$ is illustrated in Fig. 4 for several environmental models, which differ by the assumed geoacoustic parameters of the ocean bottom. In Fig. 4, we model the seafloor as a homogeneous sediment layer of thickness h with the sound speed c_s, wave attenuation α_s, and density ρ_s overlying a homogeneous fluid half-space with the sound speed c_b, wave attenuation α_b, and density ρ_b. Shear rigidity of the seafloor is not accounted for in this simplified environmental model.

Figure 4 shows normalized peak intensity J of back-propagated noise cross-correlations for eight environmental models. (J is defined in Section 2A.) The models differ by varying four most geoacoustic parameters, h, c_s, ρ_s or c_b, one at a time, resulting in eight back-propagation scenarios (Fig. 4a–h). Passive time-reversal with a single-element TRM proves to be rather robust. When two hydrophones are separated by 5.01 km, or about 50 ocean depths, strong focusing of numerically back-propagated noise cross-correlation functions (NCCFs) occurs even for environmental models that are rather different from each other. As in numerical simulations (Fig. 2), position of the main focus of the back-propagated NCCF proves to be sensitive to the environmental parameters (Fig. 4). Thus, the position of the focus can be used to characterize the environment.

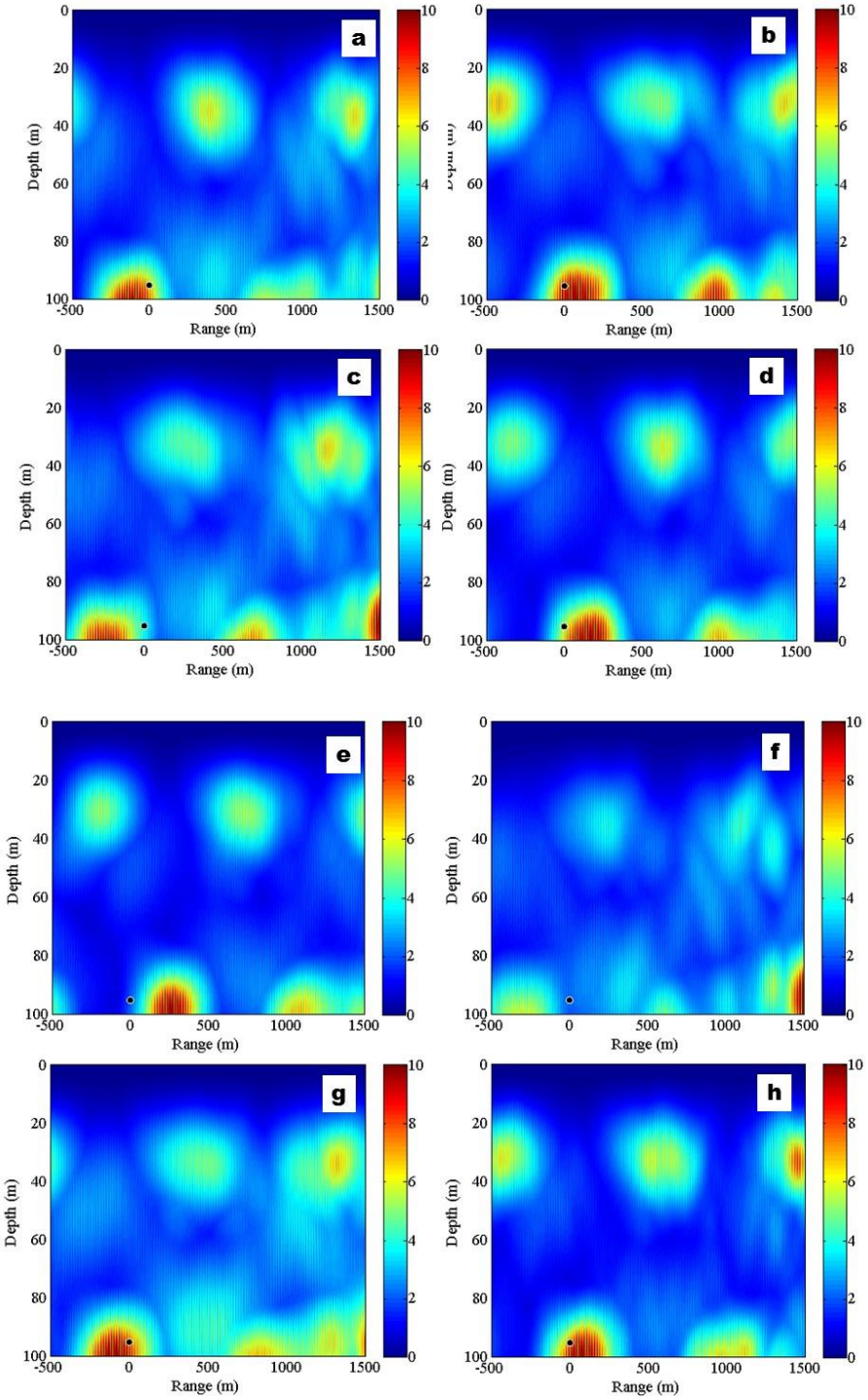

Fig. 1.4. Time-reversal of the acoustic noise cross-correlation function $C_{12}(t)$ measured in the Straits of Florida. The negative time-delay part of the cross-correlation function of noise recorded by instruments 1 and 2 is back-propagated assuming eight different environmental models. The normalized peak intensity of the back-propagated acoustic field in the vertical cross-section of the waveguide is shown by color. The black dot indicates position of the virtual sound source. Geoacoustic parameters in the eight environmental models are: **(a)** h = 20 m, c_s = 1540 m/s, $\rho_s = 1.3\rho_w$, and c_b = 1800 m/s; **(b)** h = 20 m, c_s = 1560 m/s, $\rho_s = 1.3\rho_w$, and c_b = 1800

m/s; **(c)** h = 20 m, c_s = 1551 m/s, $\rho_s = 1.1\rho_w$, and c_b = 1800 m/s; **(d)** h = 20 m, c_s = 1551 m/s, $\rho_s = 1.5\rho_w$, and c_b = 1800 m/s; **(e)** h = 15 m, c_s = 1551 m/s, $\rho_s = 1.3\rho_w$, and c_b = 1800 m/s; **(e)** h = 15 m, c_s = 1551 m/s, $\rho_s = 1.3\rho_w$, and c_b = 1800 m/s; **(f)** h = 25 m, c_s = 1551 m/s, $\rho_s = 1.3\rho_w$, and c_b = 1800 m/s; **(g)** h = 20 m, c_s = 1551 m/s, $\rho_s = 1.3\rho_w$, and c_b = 1750 m/s; and **(h)** h = 20 m, c_s = 1551 m/s, $\rho_s = 1.3\rho_w$, and c_b = 1900 m/s. In all models, $\rho_b = 2.2\ \rho_w$, α_s = 0.1 dB/wavelength, and α_b = 0.8 dB/wavelength.

D. Inverse problem

In order to find an environmental model which is consistent with noise measurements, we model the seafloor as a homogeneous sediment layer overlying a homogeneous fluid half-space and search for the layer thickness and sound speeds, densities, and wave attenuation values in the layer and the half-space that minimize the horizontal displacement of main focus of the back-propagated field from the virtual sound source. Geoacoustic inversions were performed in a two-stage process using an exhaustive search in a discretized parameter space. First, parameters of homogeneous sediment layer and subbottom (half-space) were found by minimizing the horizontal shift of the main focus of the back-propagated field from the virtual source position. Geoacoustic parameters were allowed to vary within the following bounds: $0 < h < 40$ m, 1500 m/s $< c_s <$ 2000 m/s, $1 < \rho_s /\rho_w < 2$, 1500 m/s $< c_b <$ 2500 m/s, $1.5 < \rho_b /\rho_w < 3$, $0 < \alpha_{s,\,b} < 1$ dB/wavelength. At the second stage, values of three most sensitive geoacoustic parameters (namely, thickness, sound speed, and density of the sediment layer) were refined by repeating the exhaustive search on a finer grid in a narrow range of the parameter values.

When using the negative time-delay part of $C_{12}(t)$ as the dataset, such a geoacoustic inversion gives h = 20 m, c_s = 1551 m/s, ρ_s/ρ_w = 1.3, α_s = 0.1 dB/wavelength, c_b = 1800 m/s, ρ_b /ρ_w = 2.2, α_b = 0.8 dB/wavelength. The relative intensity J of the back-propagated field for this environmental model is shown in Fig. 5a. Despite various experimental errors and an idealized environmental model, back-propagation of the measured NCCF from a location of one hydrophone gives a field with a pronounced focus in the vicinity of the other hydrophone. Remarkably, back-propagation of the positive time-delay part of $C_{12}(t)$ in this environment also leads to focusing at the hydrophone position (Fig. 5b). The quality of focusing of time-reversed NCCF in the experiment (Fig. 5a, b) is comparable to that achieved in back-propagation of the Green's function in numerical simulations (Fig. 2a).

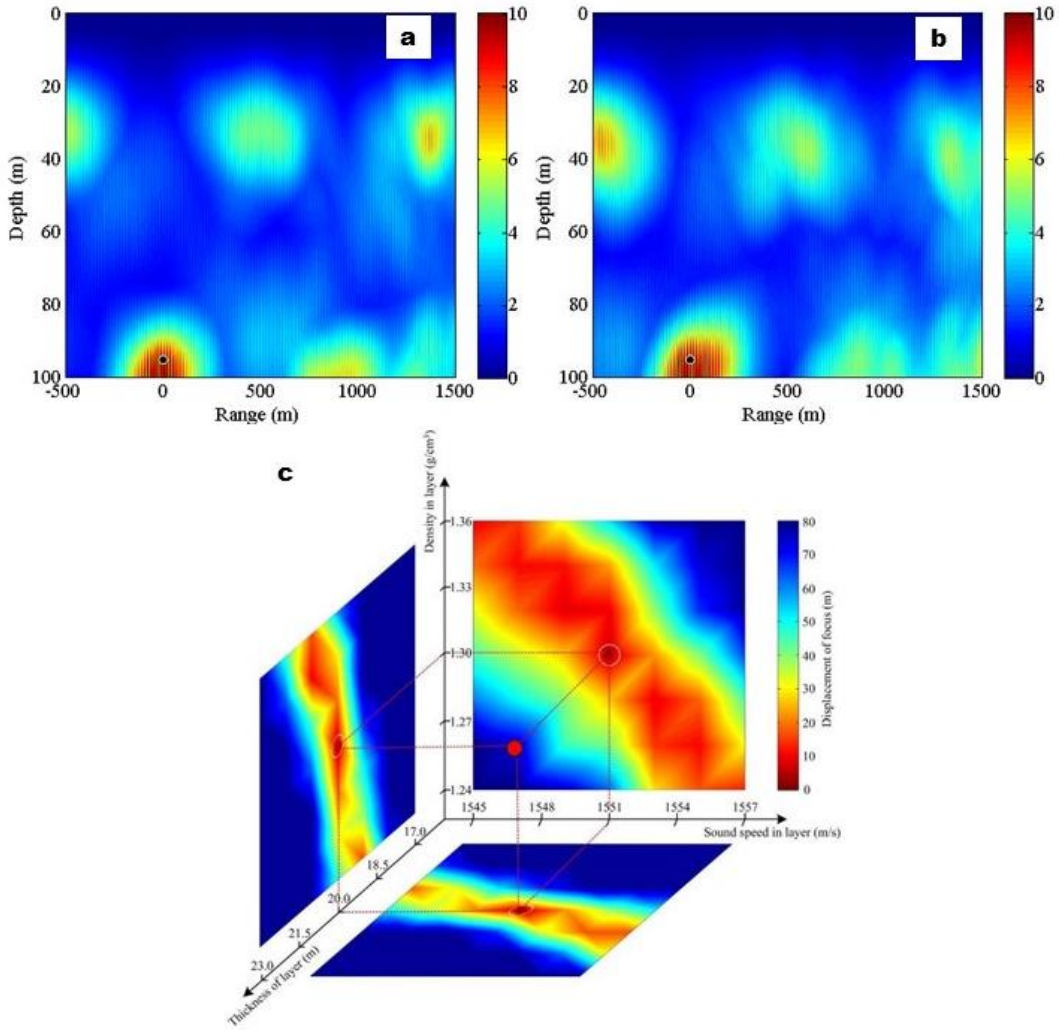

Fig. 1.5. Time-reversal of the acoustic noise cross-correlations measured in the Straits of Florida. The negative **(a)** and positive **(b)** time-delay parts of the cross-correlation function $C_{12}(t)$ of noise recorded by instruments 1 and 2 are back-propagated in the environmental model obtained through a geoacoustic inversion. The normalized peak intensity of the back-propagated acoustic field in the vertical cross-section of the waveguide is shown by color. The black dot indicates position of the virtual sound source. Panel **(c)** shows the absolute value of the horizontal displacements of the main focus from the virtual sound source, which are caused by deviations of the sound speed, density, and thickness of the sediment layer from their optimal values. The plot is obtained by back-propagating the negative time-delay part of $C_{12}(t)$.

Accuracy of the geoacoustic inversion is limited by the uncertainty in the horizontal positions of the hydrophones (~10 m in the experiment) and by sensitivity of the focusing to individual environmental parameters. Sound attenuation was found to affect primarily the strength of foci of

the time-reversed field; the position of the main focus does not provide reliable constraints on α_s and α_b within the plausible range 0 – 1 dB/wavelength of their values. In the vicinity of the optimal values of the environmental parameters, 10 m displacement of the main focus results from variations $\delta h \sim 0.2$ m, $\delta c_s \sim 1$ m/s, or $\delta\rho_s/\rho_w \sim 0.01$ in the sediment layer parameters (Fig. 1.5c). Thus, these parameters are strongly constraint by the data. Sensitivity to c_b is an order of magnitude less than to c_s; the ratio ρ_b/ρ_w cannot be reliably restricted within the 2.2 – 2.5 range. A more accurate evaluation of geoacoustic parameters of the ocean bottom beneath the sediment layer requires extending noise interferometry to lower frequencies. Within the stated uncertainties of the geoacoustic inversion, our environmental model is consistent with the geoacoustic parameters obtained by waveform matching using ray and normal mode representations of the noise cross-correlations.

Additional information on the sensitivity of the inverse problem solution to various geoacoustic parameters is provided by Fig. 4, which shows back-propagation results for environments, where one of the four most sensitive environmental parameters, h, c_s, ρ_s or c_b, is increased or decreased compared to its optimal values. Increase and decrease of the sediment sound speed shift the main focus of the time-reversed acoustic field horizontally in opposite directions (Figs. 4a, b), with the range from the TRM to the focus varying almost linearly with the c_s perturbation within the approximately ±0.7% range of c_s variations that is considered here. The shift of the focus is accompanied by nonlinear distortions of the focus shape and the contrast between the main and spurious foci (cf. Figs. 4a, b and 5a). Effects due to perturbations of the sediment density (Fig. 1.4c, d) are similar to that of c_s except that the relative changes in ρ_s, which are needed to produce a comparable shift of the focus, are much larger than relative changes in c_s. Figures 1.4g and 1.4h show that sensitivity of the back-propagated field focusing to variations of the half-space sound speed c_b is an order of magnitude weaker than to variations of c_s despite the sediment layer being thinner than the acoustic wavelength in the frequency band 20–70 Hz of C_{12} measurements.

In contrast to c_s, ρ_s, and c_b perturbations, plausible ±5 m changes in the thickness of the sediment layer have a strongly nonlinear effect on the position of the main focus (Figs. 4e, f). While a 5 m decrease in h shifts the pattern of foci by about 250 m without pronounced changes in the contrast between the main and spurious foci (cf. Figs. 1.4e and 1. 5a), a 5 m increase in h removes the main focus from the vicinity of the virtual source (Fig. 1.4f).

Note that use of the position of the main focus of the back-propagated field to determine unknown geoacoustic parameters leads to a rather robust setting of the inverse problem. The main focus can be continuously tracked, and an optimal solution of the inverse problem can be found, even when the initial environmental model in the optimization process gives the main focus at a point that is shifted from the virtual source by several ocean depths and as far as 15% of the true distance between the TRM and the virtual source.

Our approach to passive remote sensing has similarities to some noise-interferometry approaches advanced in other contexts. Single-element passive TRM can be viewed as an

extension of "time-exposure acoustics" to the oceanic waveguide or extension of the compressed cross-correlation function technique to the case of multi-mode propagation. As almost any method of inverting measured acoustic fields for environmental parameters, our application of passive TRM to ocean remote sensing can be viewed as a particular implementation of matched field processing (MFP) [26]. In this context, distinguishing features of our approach are use of ambient noise cross-correlations instead a field of a compact sound source and the choice of the MFP cost function as a horizontal displacement of the main focus of the back-propagated field from the location of a virtual sound source.

Feasibility of passive TRM was previously demonstrated in a deep ocean using multi-element hydrophone arrays. When combined with noise interferometry, focusing of the time-reversed field is expected when a series of requirements is fulfilled: 1) passive TRM has a wide aperture and many elements; 2) the noise field is perfectly diffuse; 3) the NCCF is a superposition of the deterministic Green's functions $G_{AB}(t)$ and $G_{BA}(-t)$; and 4) the environmental parameters are stationary in time and are known exactly. Our results indicate that some of these requirements are unnecessary and can be relaxed in shallow-water waveguides, which makes ocean remote sensing with passive TRM possible and, arguably, practical. We have found that, even with a single-element passive TRM (i.e., just two noise-recording hydrophones), the focusing is robust enough to compare various environmental models and retrieve good estimates of the geoacoustic parameters of the seafloor in the coastal ocean. It should be emphasized that success of a passive TRM does not rely on the noise field being perfectly diffuse; underwater noise never is. Under realistic assumptions about noise sources in the ocean, NCCF consists of the same ray or normal arrivals as the superposition of the Green's functions $G_{AB}(t)$ and $G_{BA}(-t)$; the ray travel times and phases of individual normal modes are the same in the NCCF and in the Green's functions, while amplitudes of the rays or normal mode components of NCCF are determined by noise directionality and are generally different from those generated by a point source [4, 24, 27]. However, an accurate reproduction of the Green's functions kinematic structure (i.e., the ray travel times and normal mode phases) is sufficient for the time-reversed field to focus at the location of the virtual source.

As discussed in Section 2C, signal-to-noise ratio (SNR) in NCCF measurements is considerably smaller for the 2–3 instrument pair than for 1–2 pair. (SNR in C_{12} and C_{23} measurements can be evaluated as the ratio of the magnitude of NCCF peaks and $2^{1/2}$ times the average magnitude of the NCCF estimate around zero time lag in Figs. 3a and 3b, respectively.) SNR decrease with range is due to the fact that NCCF magnitude, i.e., "signal," slowly decreases with range in a waveguide as does magnitude of the Green's function, while "noise" remains the same. Moreover, tidal variations of ocean depth and, possibly, other variations of the acoustic propagation conditions during the noise averaging period lead to a loss of noise coherence, which is predicted to rapidly grow with range and wave frequency. The coherence loss decreases SNR and narrows the effective frequency band of the passive TRM.

Relative peak intensity J of the back-propagated NCCF $C_{23}(t)$ is shown in Fig. 6 for the optimal environmental model that we derived from back-propagation of $C_{12}(t)$. One of the parameters, ρ_s, of the environmental model was adjusted in Fig. 6 to make the main focus stronger. Note strong focusing of the back-propagated field at the position of the virtual source in Fig. 6b, which is obtained by time-reversing the positive time delay part of $C_{23}(t)$. When the passive TRM employs the negative time delay part of $C_{23}(t)$, the focus in the vicinity of the virtual source proves somewhat weaker than the spurious focus around 1100 m range (Fig. 6a). This is a consequence of the lower SNR in the $C_{23}(t)$ measurement. Compared to the TRM at 5.01 km range, passive TRM at the range of 9.76 km, or about 100 ocean depths, gives considerably broader main foci (cf. Fig. 1.6 and Fig. 1.5a, b). We attribute the difference to the lower SNR and to decrease in the effective frequency band of the back-propagated field at the longer range.

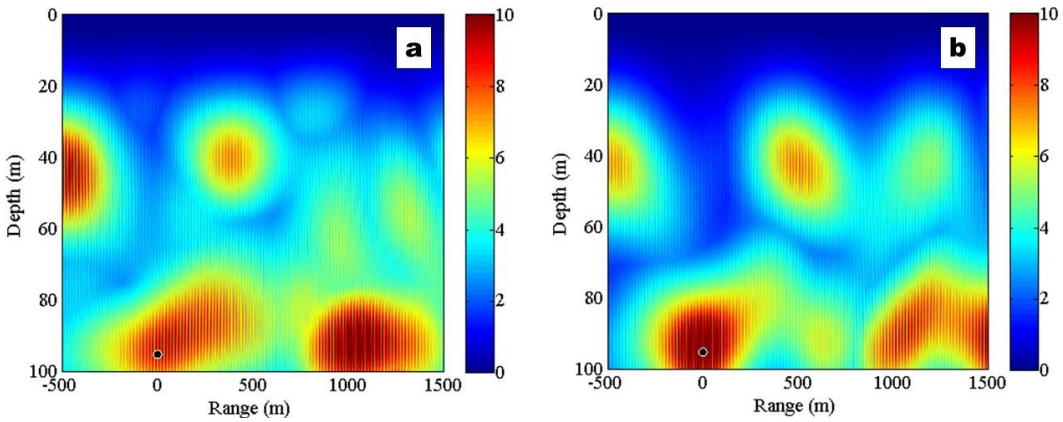

Fig. 1.6. Time-reversal of the acoustic noise cross-correlation function $C_{23}(t)$ measured in the Straits of Florida. The negative **(a)** and positive **(b)** time-delay parts of the cross-correlation function of noise recorded by instruments 2 and 3 are back-propagated assuming the following geoacoustic parameters: h = 20 m, c_s = 1551 m/s, $\rho_s = 1.55\rho_w$, $\alpha_s = 0$, c_b = 1800 m/s, $\rho_b = 2.2\ \rho_w$, and $\alpha_b = 0.8$ dB/wavelength. The normalized peak intensity of the back-propagated acoustic field in the vertical cross-section of the waveguide is shown by color. The black dot indicates position of the virtual sound source.

An additional reason for the poorer focusing in Fig. 1.6 compared to Fig. 1.5a, b lies in an actual difference between propagation conditions on the paths between the 1–2 and 2–3 instrument pairs, which is not reflected in our simplified environmental model. We assumed constant ocean depth of 100 m. This is a reasonable approximation for the path between instruments 1 and 2, where ocean depth varied between 97 m and 101 m. However, it is not realistic to treat the ocean as range-independent on the path between the 2–3 instrument pair, where ocean depth varied between 86 m and 100 m. Further research is necessary to determine the extent to which an account for the range-

dependent bathymetry improves passive TRM performance at longer ranges and whether it allows one to avoid adjustments to geoacoustic parameters.

We have shown that an acoustic time-reversal mirror can be realized in a coastal ocean environment at a distance that is large compared to the ocean depth using ambient noise recorded on only two hydrophones. In numerical simulations, strong focusing occurs in the vicinity of one hydrophone when the cross-correlation function is back-propagated from the other hydrophone, with the position and strength of the focus being sensitive to density and sound speed in the bottom. Values of these parameters at an experimental site in the Straits of Florida have been estimated by optimizing focusing of the back-propagated cross-correlation functions. The results of the geoacoustic inversion are consistent with values of the seafloor parameters evaluated independently by other means.

Our results indicate that passive time-reversal works in shallow-water oceanic waveguides at ranges of at least 50 ocean depths. Such ranges are of practical interest for remote sensing of the water column and the ocean bottom. Passive acoustic techniques do not contribute to noise pollution in the ocean and are inherently environmentally friendly. Robustness of the passive time-reversal and the promise of using single-element TRMs suggest that a low-cost ambient-noise-based ocean-monitoring system is feasible. With N hydrophones generating a network of $N(N-1)/2$ single-element TRMs, the amount of gathered oceanographic data rapidly increases with N. Further work is necessary to study exploitation of other characteristics of the back-propagated NCCFs, including the time history of the field at the focus point, for retrieving additional environmental information, and to quantify the sensitivity of the technique to current velocity and variations of water temperature.

1.2. Geoacoustic inversion using TRM of ocean noise in Shallow Water 2006 experiment

Wave propagation in oceans is usually influenced significantly by bottom properties, especially for shallow water or transitional areas. Due to the difficulty and high cost of direct measurement for the bottom parameters, geoacoustic inversion as an important

kind of indirect method has received considerable attention in underwater acoustics. A variety of inversion methods have been developed in recent years, (Fallat et al, 2000) and most of them are based on active schemes. In the active inversion methods, physical properties of the environment affecting acoustic propagation can be retrieved from observations of signals generated by powerful controlled sound sources.(Baggeroer et al, 1993)] Passive acoustic inversion method employs the ubiquitous ambient noise as a replacement of the designated probing signals(Siderius et al, 2006) For the passive method, acritical issue is Green’s function (GF) retrieval. The process by which approximations to GFs between twolocations are estimated by cross-

correlating time series of ambient noise recorded at those locations is widely referred to as noise interferometry (NI). The underlying theory has been well developed.

It is well known that if a pulse signal is radiated at one point and the field is recorded at multiple distant locations, then retransmitting the timereversed recorded signals at those locations results in a wave field that focuses at the original sound generation point (Jackson et al, 1991) This process is referred to as implementation of a time reversal mirror (TRM). (Roux and Kuperman, 2005) firstly demonstrated that the GFs obtained from noise cross-correlation functions (NCCFs), rather than measured responses to active source transmissions, can be used to successfully implement a TRM. The time reversal of ocean noise makes one of the receivers act as a virtual source. In this Letter, we combine the NI and TRM techniques to invert ocean bottom parameters passively. Firstly, numerical simulations are performed to verify that bottom parameters can be determined from the requirement that the TRM focuses the wave field at the position of the sound source or, by extension, of the virtual source created through NI. Secondly, we extract the GF from the NCCF measured by two single hydrophones in the Shallow Water ’06 (SW06) experiment. Thirdly, combined with the extracted GF, the TRM is used to search for the optimal sound speed and density in the bottom.

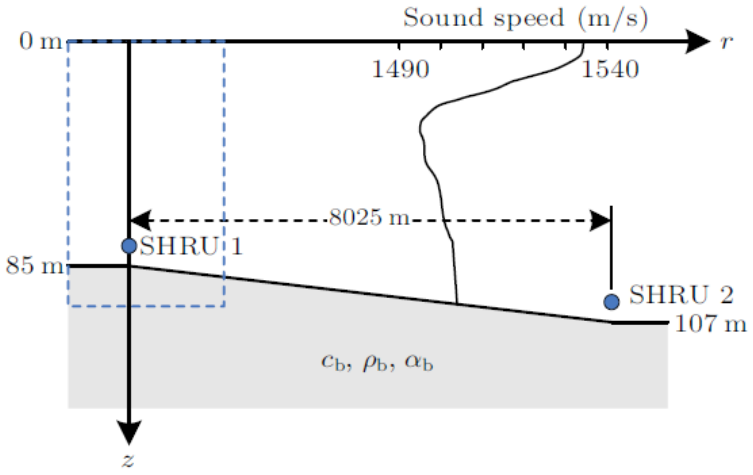

Fig. 1.7 Geometry of the ocean environment between SHRU 1 and SHRU 2 in the SW06 experiment.

We consider the ocean environment as shown in Fig. 1.7, which is the same as one part of the SW06 experiment. In the experiment, five single hydrophone receiving units (SHRUs) were positioned on the across shelf path. We choose the waveguide between SHRU 1 and SHRU 2 to analyze. The water depth at the position of SHRU 1 is 85 m, and that at the position of SHRU 2 is 107 m. We assume that the bathymetry between the two receivers varies linearly. Both of the SHRUs are located 7m above the bottom, and the
horizontal distance between them is 8025 m. The bottom is modeled as a uniform fluid halfspace in this work. The averaged sound speed profile measured in the experiment is used in the following simulations.

Let a point sound source be located at the position of SHRU 1, to emit a signal s0(t) with a spectrum S(f). The spectrum has the form

$$S(\omega) = \begin{cases} 1, 10\text{ Hz} \le \frac{\omega}{2\pi} \le 70\text{Hz} \\ 0, \text{elsewhere} \end{cases} \tag{1.1}$$

In the frequency domain, the acoustic pressure at the position of SHRU 2 is given by

$$P(r_2, \omega) = S(\omega)G(\omega) \tag{1.2}$$

where $G(\omega)$ is the frequency-domain GF between the points of SHRUs 1 and 2. Next, reverse the received time-domain signal and reradiate it. The acoustic pressure received at the position of SHRU 1 is

$$P(r_1, \omega) = S^*(\omega)G^*(\omega)G(\omega) \tag{1.3}$$

where * denotes the complex conjugation. The focusing field is expected at the point of SHRU 1 if there are sufficient multi-paths connecting the two points. We calculate the frequency-domain acoustic pressure $P(r, z, \omega)$ using a wide-angle parabolic equation model RAM.[20] Subsequently, time-domain pressure $p(r, z, t)$ is Fourier-synthesized from $P(r, z, \omega)$. $E(r, z) = \left|\max_{t>0}[p(r, z, t)]\right|^2$. The normalized peak intensity $J(r, z) = -10\log\left[1 - \frac{0.99E(r,z)}{E_0}\right]$ with $E_0 = \max_{r,z}[E(r, z)]$ is given in the dashed rectangular area around SHRU 1 as shown in Fig. 1.7 in the following results. Figure 1.8(a) shows the simulation result using the bottom parameters with the sound speed of 1750 m/s, the density of 1.9 g/cm^3, and the attenuation of 0.02 dB/wavelength. A sharpened focus can be observed in Fig. 1.8(a) exactly at the position of SHRU 1. If the bottom parameters for wave propagating from SHRU 1 to SHRU 2 are different from those for back-propagating, the main focus will shift and blur, or the spurious additional foci will become more pronounced. From Figs. 1.8(b)–8(d), we can see that the main-focus shift of the back-

propagating wave is sensitive to mismatches of sound speed and density in the bottom. The simulation results suggest that bottom parameters can be estimated from the position of focusing sound field generated by the TRM. It should be emphasized that the focusing position is insensitive to the bottom attenuation coefficient, which is considered as a constant of 0.02 dB/wavelength in this study.

For noise data recorded by SHRUs 1 and 2 in the SW06 experiment, we evaluate the NCCF from a Fourier transform of the cross spectrum, which is calculated by summating over a large number of data segments in 5.7 d. There are 10% data segments with the highest noise level that are discarded to suppress contributions of strong, localized and transient sources.

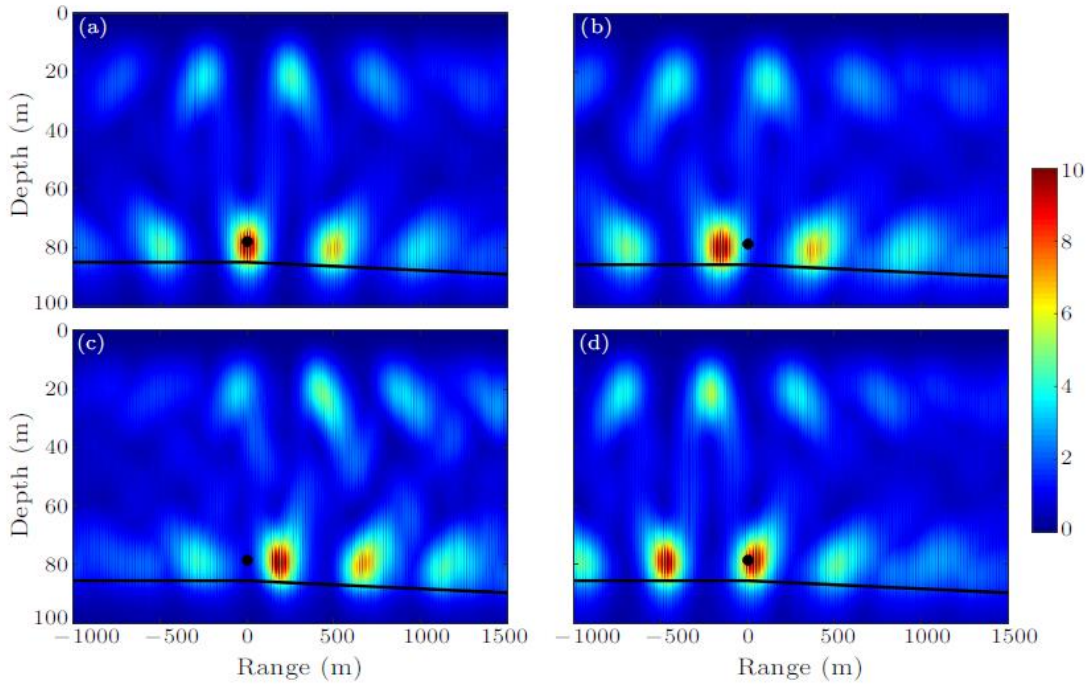

Fig. 1.8. Sensitivity for the position shift of focusing wave field generated by the TRM to the bottom parameters. The sound speed is 1750 m/s and the density is 1.9 g/cm^3 in the bottom for forward wave propagating. The sound speed and density for back-propagating are (a) 1750 m/s and 1.9 g/cm^3, (b) 1700 m/s and 1.9 g/cm^3, (c) 1850 m/s and 1.9 g/cm^3, and (d) 1750 m/s and 1.5 g/cm^3. In each panel, the black dot denotes the position of the sound source, and the bathymetry is indicated by a thick black line.

To equalize contributions of various sources, the noise spectra are normalized in each data segment. Figure 1.9(a) shows the final result in the frequency band of 10–70 Hz, in which there are two peaks around the time delays of _5.5 s, respectively. The NCCF is approximately proportional to the sum of forward and backward GFs between SHRU 1 and SHRU 2, i.e., C(t) =

A[G(t) + G(□t)], where A is a constant. An unexpected smaller peak also appears in Fig.1.9(a) because some signals are probably treated as noise. In the following we choose the negative time delay part

of NCCF as GF, which is the waveform in the dashed box in Fig. 1.9(a). The fine structure of the backward GF is given in Fig. 1.9(b). In principle, we could obtain the same GF from the positive time delay part of NCCF if the noise field is perfectly diffuse.

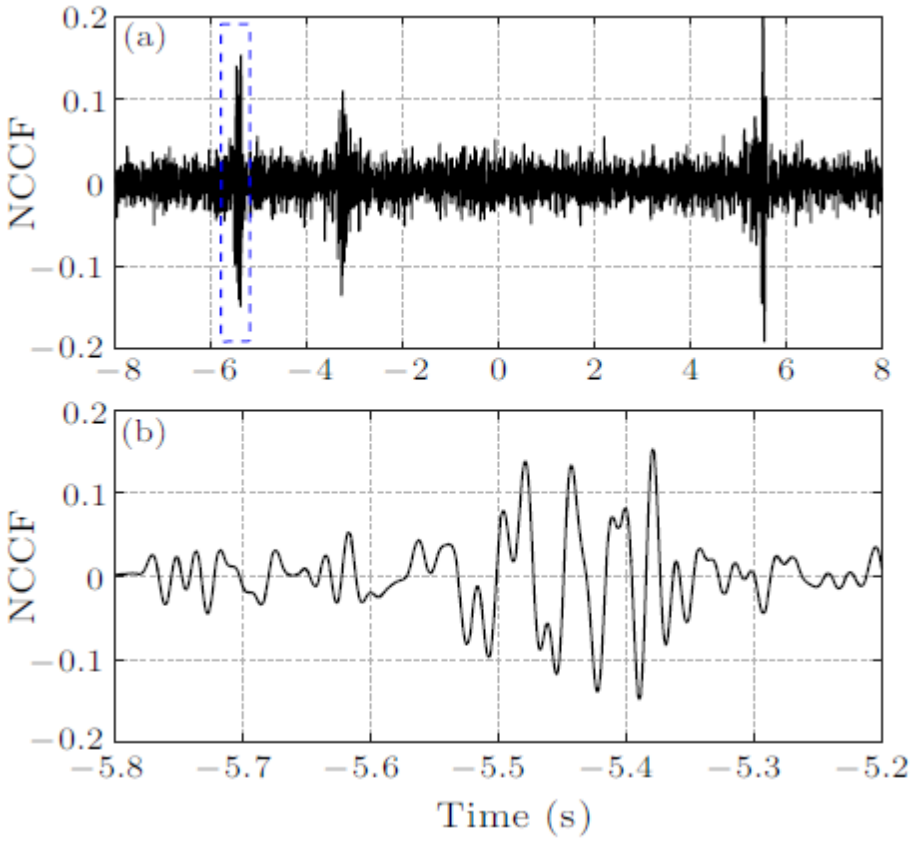

Fig. 1.9. The noise cross-correlation function (NCCF) for SHRUs 1 and 2 in the SW06 experiment (a) and the fine structure of negative time delay part (b). The frequency band is in the range of 10–70 Hz.

In the following we realize a passive TRM using the GF retrieved from the ambient noise to invert bottom parameters. The process of implementing TRM is almost the same as the above numerical simulations. The only difference is the absence of a source in the waveguide. Instead, SHRU 1 serves as a virtual source. At the position of SHRU 2, the retrieved GF is firstly time-reversed, then we reradiate the reversed signal and make it propagate toward SHRU 1 by calculating the backward GF numerically. Next the quantity $J(r,z)$ is plotted around SHRU 1 to

find a focus. We model the bottom as a uniform fluid halfspace and search for the bottom parameters that minimize the displacement of main focus from the virtual sound source. In the geoacoustic inversion, the searching region for bottom sound speed is from 1650 to 1900 m/s. For a given sound speed c_b, the corresponding density ρ_b is obtained by the Hamilton sediment empirical relationship for continental terrace

$$c_b = 2330.4 - 1257.0\rho_b + 487.7\rho_b{}^2 \quad (1.4)$$

Figure 1.10 gives the displacements of main focus from the virtual sound source SHRU 1, which are caused by deviations of bottom parameters from their true values. The minimum appears at the sound speed of 1770 m/s, which is the optimal value for the environment between SHRU 1 and SHRU 2. The optimal density is 2.0 g/cm^3 according to the empirical relationship of Eq. (4).

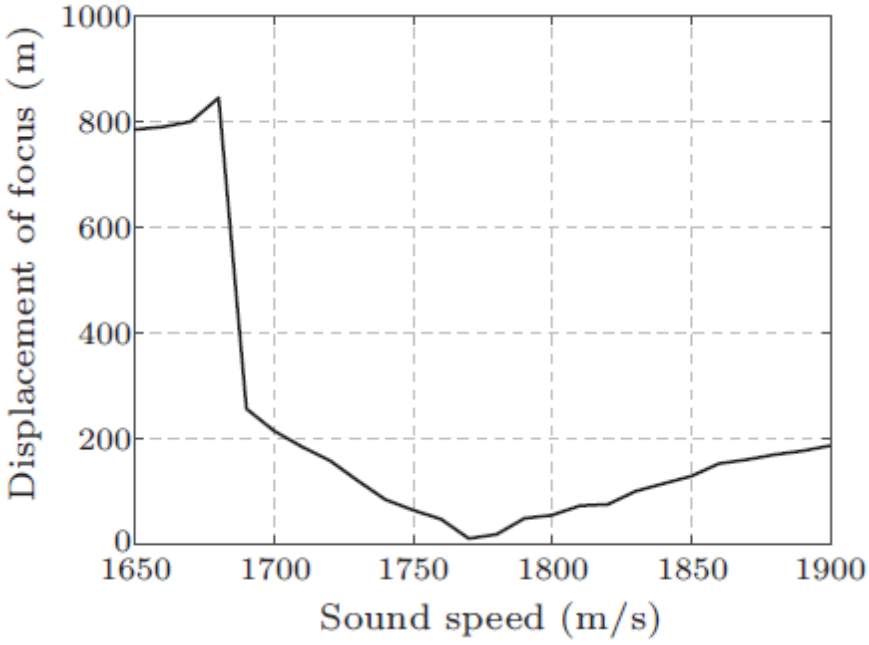

Fig. 1.10. Displacement of main focus from the virtual sound source versus bottom sound speed.

The normalized peak intensity *J(r; z)* of the back propagated field for the optimal bottom parameters is shown in Fig. 1.11(a). Remarkably, back propagation of the measured NCCF from the location of SHRU 2 gives a field with a pronounced focus in the vicinity of SHRU 1. The focusing quality of time-reversed NCCF in the experiment is comparable to that achieved in back-propagation of the simulated GF (Fig. 1.8(a)). The normalized peak intensity of the back-propagated

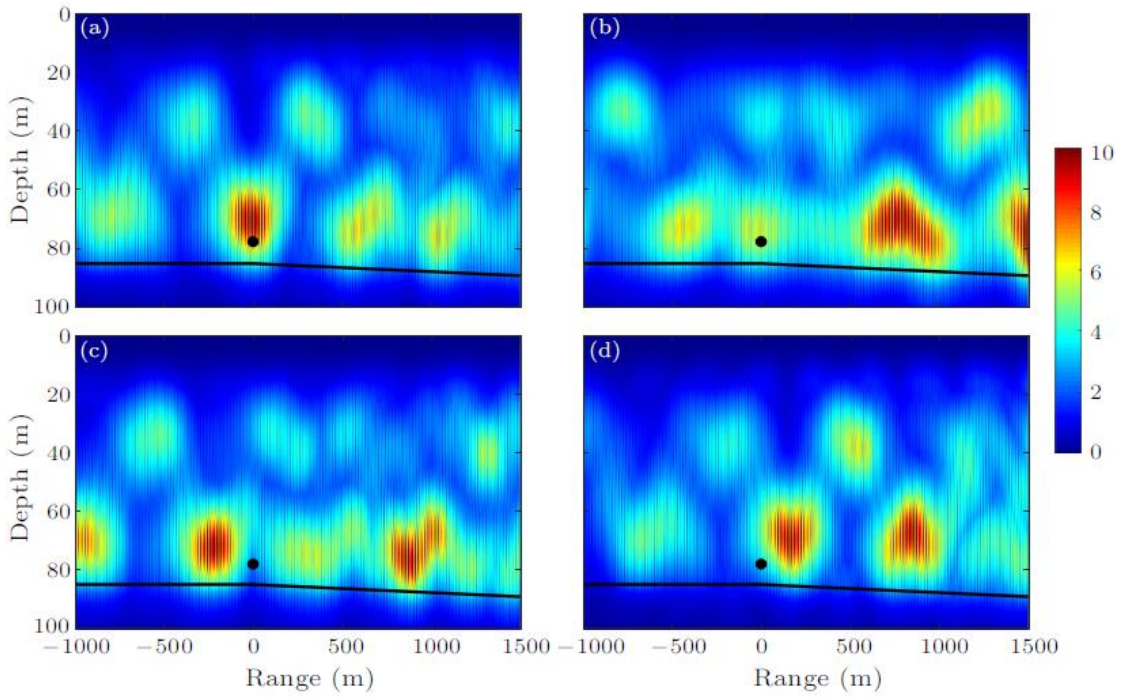

Fig. 1.11. Time reversal of GF retrieved from NCCF in the SW06 experiment. The GF is back-propagated in the environments with different bottom parameters. Normalized peak intensity of the back-propagated acoustic field in the vertical cross-section of the waveguide is shown by color. Sound speed and density in the bottom are (a) 1770 m/s and 2.0 g/cm^3, (b) 1650 m/s and 1.8 g/cm^3, (c) 1700 m/s and 1.9 g/cm^3, and (d) 1900 m/s and 2.2 g/cm^3. In each panel, the black dot denotes the position of the virtual sound source SHRU 1, and the bathymetry is indicated by a thick black line.

field for other bottom parameters are also given in Figs.1.11(b)–1.11(d). As in numerical simulations, the position of the main focus of the back-propagated NCCF proves to be sensitive to the bottom parameters. A mismatch between the actual bottom parameters and the parameters assumed in back-propagating the retrieved GF shifts and blurs the main focus, while making the spurious additional foci more pronounced.

The corresponding bottom densities in Fig.1.11 obtained from Eq. (4) are 2.0, 1.8, 1.9 and 2.2 g/cm^3, respectively. A uniform fluid halfspace bottom model is used in the inversion method, which includes three parameters: sound speed, density and attenuation. As discussed in Ref. [22], the equivalent single-layer bottom model has the same effect on the underwater acoustic field as the multiple-layer models within some range-frequency domain of interest. Furthermore, the Hamilton sediment empirical relationship between

sound speed and density is utilized to reduce the dimension of unknown parameters. As a result, this inversion method could avoid the multiple-solution problem, which often appears in some other geoacoustic inversion methods. It should be emphasized that the inversion method combining NI and TRM techniques can also be applied to more complex bottom models. The additional parameters will lead to a considerable increase of computation time for searching optimal solutions, and the multiple-solution problem may appear.

In summary, a passive geoacoustic inversion method combining NI and TRM techniques has been presented, in which ambient noise recorded on only two hydrophones is used. In numerical simulations, strong focusing occurs in the vicinity of one hydrophone when the GF is back-propagated from the other hydrophone, with the position and strength of the focus being sensitive to sound speed and density in the bottom. We extract the GF from the NCCF measured by two single hydrophones in the SW06 experiment.

After performing the TRM process, values of sound speed and density in the bottom are estimated by optimizing focusing of the back-propagated GF. Compared with active techniques, the passive inversion method does not contribute to noise pollution in the ocean, and consequently is inherently environmentally friendly. Moreover, this is a low-cost method because only two hydrophones are necessary.

II. MODAL DECOMPOSITION USING WARPING TRANSFORM

2.1 Warping transform

Modal filtration is a standard procedure in shallow water acoustics. There are two traditional approaches: modal filtration using orthogonal eigen functions (waveguide modes) which requires a vertical array of hydrophones and modal separation by the using arrival times. But both methods have their inconveniences. In VLA we can use orthogonality only in water column, but in reality, sound field continues in the bottom and this part of the field is impossible to measure. Arrival time method works for long enough distances only, because time interval between arrivals of different modes should be big enough for the dispersion to be noticeable. In the case of SW06 experiment for construction of CCFs we use data from single hydrophones, distance between them is about 5-7 km and the last method works not good enough.

However, for wide-band acoustical signal analysis the so called Warping Transform Technique, can be used, which was invented for image processing and effectively recreated for problems of acoustics. For the sound field from controlled sources, it can be used directly and for random diffused sources it requires construction of cross-correlation function between two receivers, which is equivalent to Green`s function (1.1), as if one or another of them was an active acoustic source.

One of the key methods currently being actively developed for the processing and analyzing incoherent signals, including mode filtering at relatively small distances, both in experiment and in theory, and which is supposed to be used, is isovelosity Warping Transform, (hereinafter WT) which is defined for the input signal $P(t)$ in the following way. If we introduce warped time t_w then signal will be transformed as a function of t_w :

$$h(t_w) = \sqrt{t_w^2 + r^2/c^2}. \qquad (2.1)$$

$$P_w(t_w) = WT(P)(t_w) = \sqrt{|h'(t_w)|}P(h(t_w)).$$

WT was proposed for signal analysis in (Baraniuk R, 1995) [16], it deals with the time-frequency characteristic of the received signal, based on the transformation (deformation) of the time variable using the nonlinear function $h(t)$, in other words, on the introduction of a new variable - warped time and/or warped frequency. WT is a unitary operator that does not belong to the

Cohen class (Cohen, 1995); its properties and the theorem defining WT for a phase-modulated signal are given in (Twaroch et al, 1998). The effectiveness of WT has been shown in a number of works, including the acoustics of the shallow water (Bonnel et al, 2011, 2012, 2013)). In addition, processing based on WT was used to analyze acoustic signals of marine mammals for passive tomography and whale specifications based on analysis and processing of the time-frequency response (Ioana, 2006). Warping transform can be used in frequency domain, if the law of dispersion is different or for each single mode, if the model with constant sound speed is not accurate enough to separate modes.

The aim of WT in marine acoustics is to linearize phase of received signal. To approach this goal, let us start with simplest waveguide model: isovelosity water column ($c = Const$) and rigid bottom.

In this case, phase of each mode in time domain will be equal to

$$\phi_m(t) = 2\pi f\sqrt{t^2 - t_r^2} \tag{2.2}$$

Where $t_r = \frac{r}{c}$ is time of receiving the signal, time of emission is $t = 0$ and $t > t_r$. Thus, the corresponding warping function *h(t)* (2.1) does not depend on the mode number and processing can be done in a single transformation.

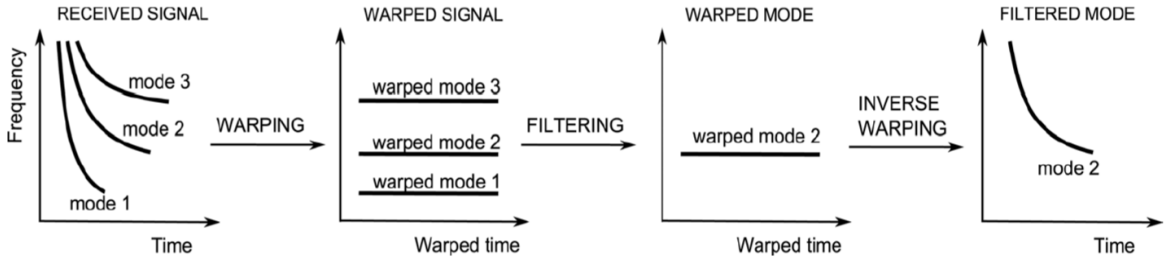

a b c d

Figure 2.1 Scheme of application of Warping Transform.

In the Figure 2.1 algorithm for application of WT is shown. (a) – spectrogram of input signal *P*(*t*), (b) is spectrogram of warped signal, (c) selection of mode 2 from warped spectrogram, (d) – mode 2 after usage of inverse WT.

Example of performance of warping transform on a simulated signal is shown on Figure 2.2. On the top, spectrogram of the modal signal for Pekeris waveguide, containing 11 modes is shown. White lines map theoretical dispersion curves for first 6 modes. Bottom plot shows the spectrogram of the signal after warping. Note that time and frequency axis are different after warping. In this exact case, additional coefficient was used to map the spectrogram on the same frequency axis.

Key feature for the usage of WT is wide frequency band of input signal, so WT seems to be adequate method to physical essence of the problem of noise interferometry. Using warping transform as one of the key methods for working with non-diffusive fields, both for the analyzing CCF built even at relatively small distances between hydrophones (for example, on a horizontal antenna), and for received signals, which again can be done at relatively small distances from the source (for example, a moving ship). As noted above, WT can provide mode filtering, that is critical for the solving inverse problem in the shallow sea.

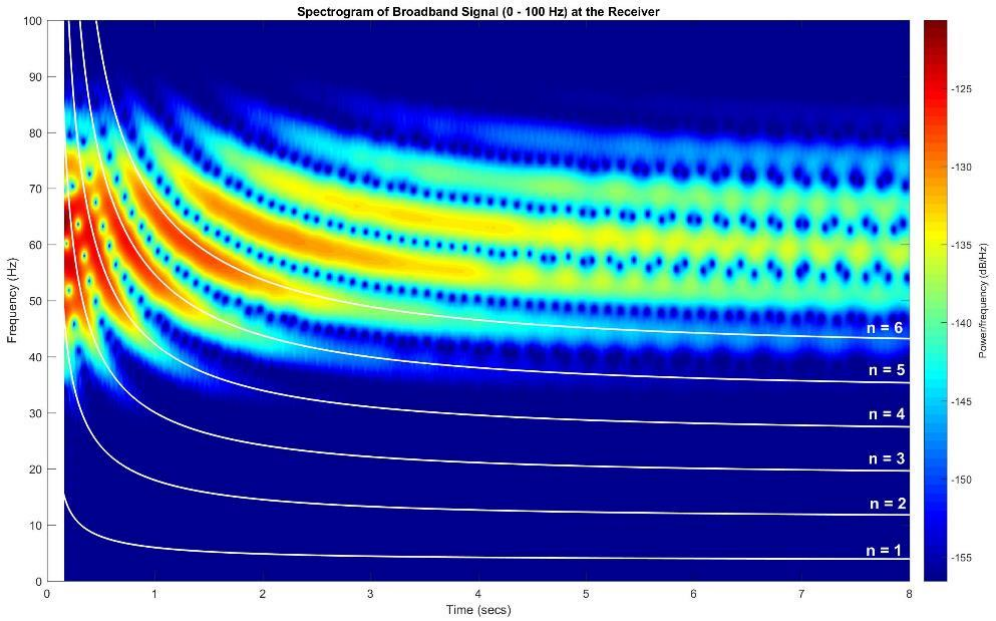

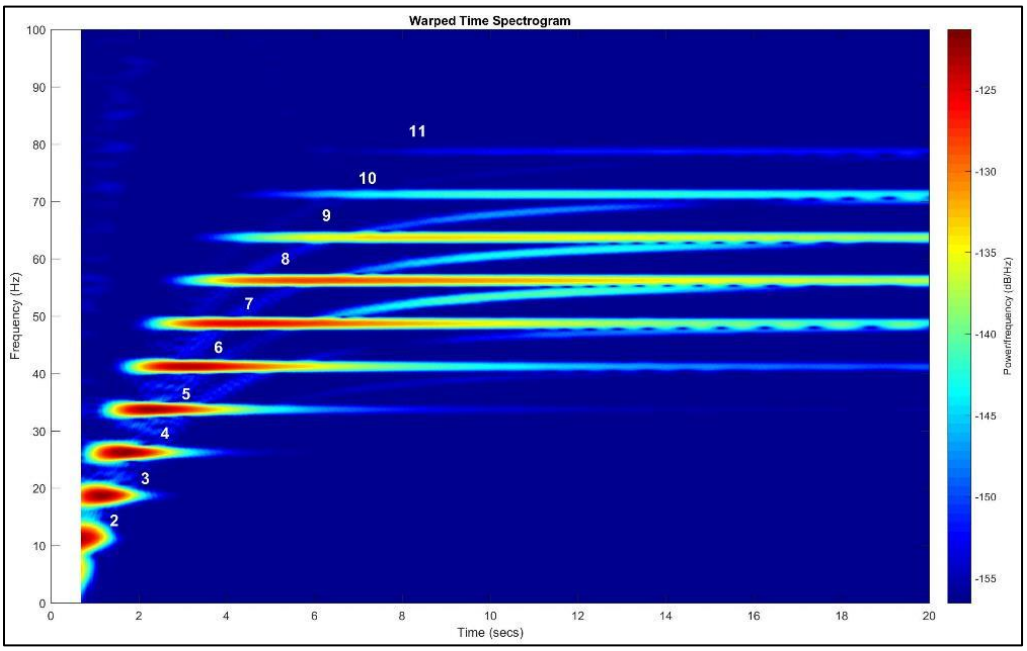

Figure 2.2 Warping transform for a signal calculated for Pekeris model with parameters r=5000 m, H=100 m, z_s=50 m, z_r=50 m, $c = 1500$ m/s, $\rho = 1050$ kg/m3, frequency band is 0-100 Hz.

Another branch of our research was processing of controlled airgun signals data acquired in experiment SWARM`95 that includes acoustic data influenced by horizontal refraction.

The goal of this work was to show possibility of identification of horizontal refraction caused by internal waves using single hydrophone data time-frequency analysis.

2.2 Example of application of the warping transform to wideband signal.

Here we will talk about some examples of using WT methodology using real data from SWARM`95 experiment. Let`s take signals from file01.mat, recorded in the Morning of August 4th 1995, where depth of airgun placement was 30 meters and influence of horizontal refraction was not noticed. For this example, we take shot #5 recorded on receiver #16.

Distance between source and receiver was about 15 km, sound speed in Pekeris model used for the transform is 1500 m/s, frequency band is 30-300 Hz, color scale of the spectrograms is logarithmic.

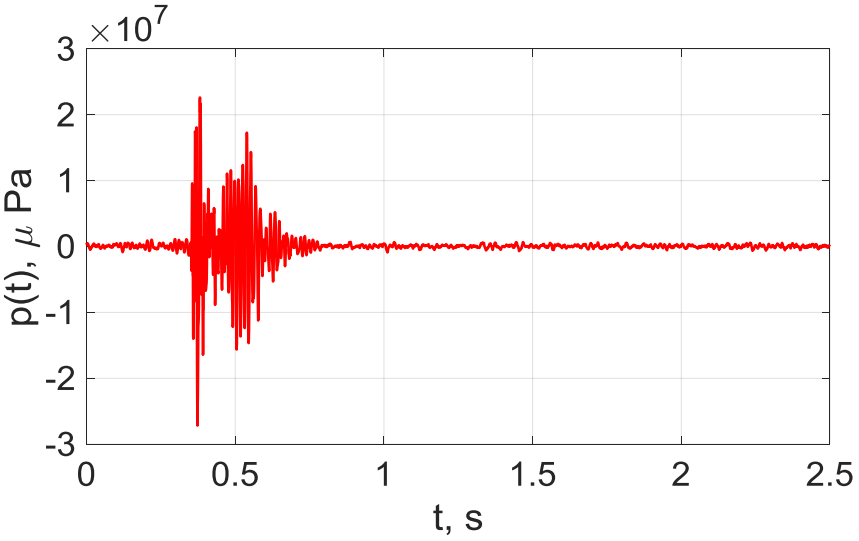

Figure 2.3. Airgun signal received by hydrophone #16 of WHOI array before editing.

One of the most important parameters for WT is the time of signal beginning (τ). From Figure 2.3 we can see that $\tau \approx 0.33$ s. Before using WT we cut out the part of the signal, where $0 \leq t \leq \tau$.

On Fig.2.4 we see how resampled signal looks. It is shorter than original and differs in amplitude, because of conservative coefficient $h'(t)$ (2.1). Difference caused by filtering is not noticeable, because we work in the same frequency band the signal was radiated.

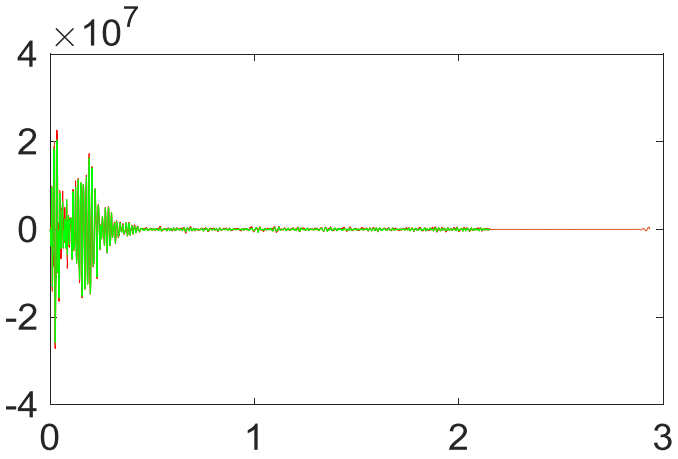

Figure 2.4. Filtered signal after WT (green) vs Cut original signal (red). X axis is time in seconds, y is pressure in μPa.

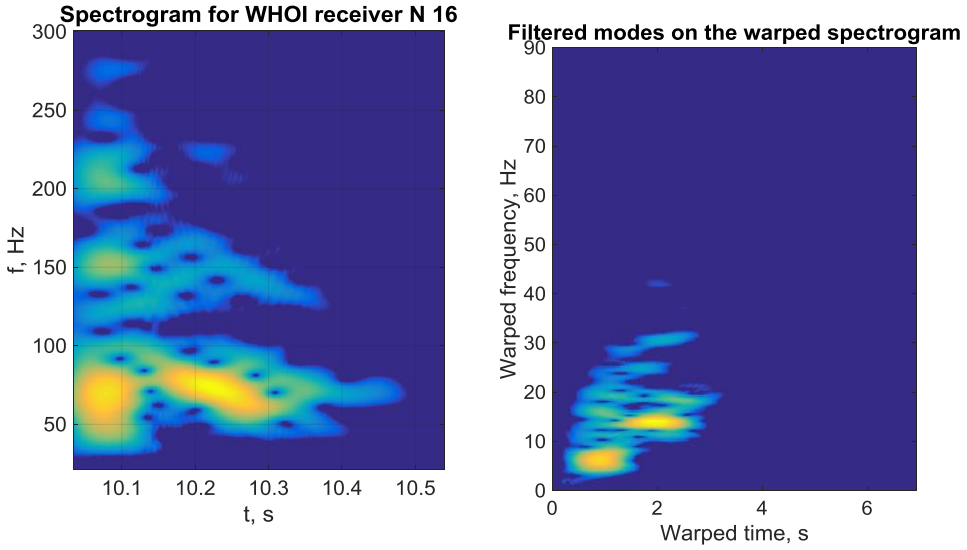

Figure 2.5. Left: Spectrogram of original signal, where the beginning $0 \leq t \leq \tau$ is deleted and time is added to r/c. Right: Spectrogram of warped signal.

On the left spectrogram of Fig.2.5 we can clearly see dispersion maxima of two first modes that are the strongest. Modes 3 and 4 are selectable, but we don`t know by which hyperbolic lines we can place and integrate them to compare their energy. In case of WT spectrogram, we see five modes. The next step to clarify it even more is to integrate WT spectrogram over time. Integral of warped spectrogram is shown on Fig. 2.6.

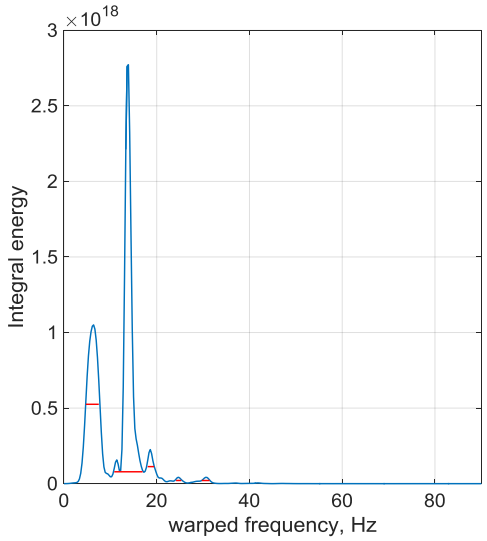

Figure 2.6. Integral of WT spectrogram with local maxima found automatically (red bars).

Parameters of choosing maxima of integral energy can differ depending on sound to noise ratio of the signal and/or a priori knowledge of modal distribution. It is also possible to pick maxima manually. Here, threshold of peak picking is 0.3 of the peak and height of the red bar is on 0.5 energy of each peak.

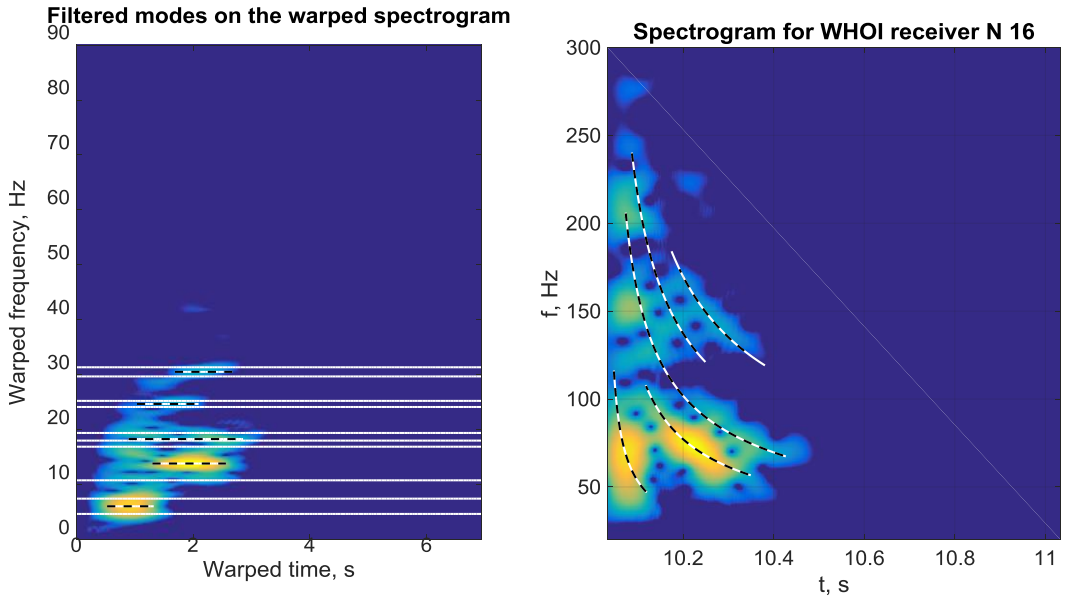

Figure 2.7. Warped spectrogram with mapped maxima of intensity (left) and original spectrogram with mapped dispersion curves, calculated from warped frequency maxima.

Next, integrals of peaks can be used to calculate energy of modes and exact warped frequencies of peaks can be used to calculate dispersion curves of each mode using Pekeris model, as shown in Fig.2.5.

$$f(t_w, f_w) = \frac{f_w}{\sqrt{1-\frac{r^2}{c^2 h(t_w)^2}}}. \tag{2.3}$$

The equation (2.1) is not the same thing as inverse WT, it just gives us an approximation for model fitting.

Now, when we have an idea of how the warping algorithm works, we should talk about parameters included.

The most sensitive is τ – the moment where signal starts. In the case of SWARM`95 experiment, we did not have the full record of the signal, from 0, when it is emitted by source. In case of SW06, where CCFs had this zero point, $\tau = r/c$, but because parameter c is taken for Pekeris model, therefore, very rough, it still needed some corrections. In SWARM data we did not know exact r/c nor τ, so the only way to choose those parameters was by choosing visually the results of spectrograms after WT. For example, if the signal start is denoted too early, the most dramatic change will appear in noise before the signal and not in the first modes. As a result, on a spectrogram of warped signal, the modes will not be as separable as we wanted. On Fig.2.10 are shown the spectrograms of the same signal, but with $\tau = 0.1$ s. Even the first modes did not separate in warped frequency domain and the algorithm did not find and map them right.

If τ is too big, it is possible to lose a part of first mode`s energy or the whole mode. It is crucial to check that the whole signal is presented on the spectrogram of original signal, in case if we don`t have exact knowledge of distance. Additionally, in SWARM data time of start of the signal slightly changed from record to record.

Nevertheless, there is a positive effect of denoting the start of the signal later than it should be. In several cases, it helps to separate modes better using WT. In case of theoretically constructed signal that we used for testing, bigger τ had a great effect on quantity of visible modes. On the figure 2.7 we see simulated signal for a distance of 10 km and sound speed in water 1500 m/s. We see that this signal has a long predecessor part with low intensity, that makes warping of this signal as it is less effective. On the Figure 2.8 spectrogram of this signal is shown. It is obvious that high energy part of the signal starts around $\tau = 7.2\ s$. Figures 2.11 a and b represent spectrograms of this signal warped using $\tau = 6.67\ s$ and $\tau = 7.2\ s$, respectively.

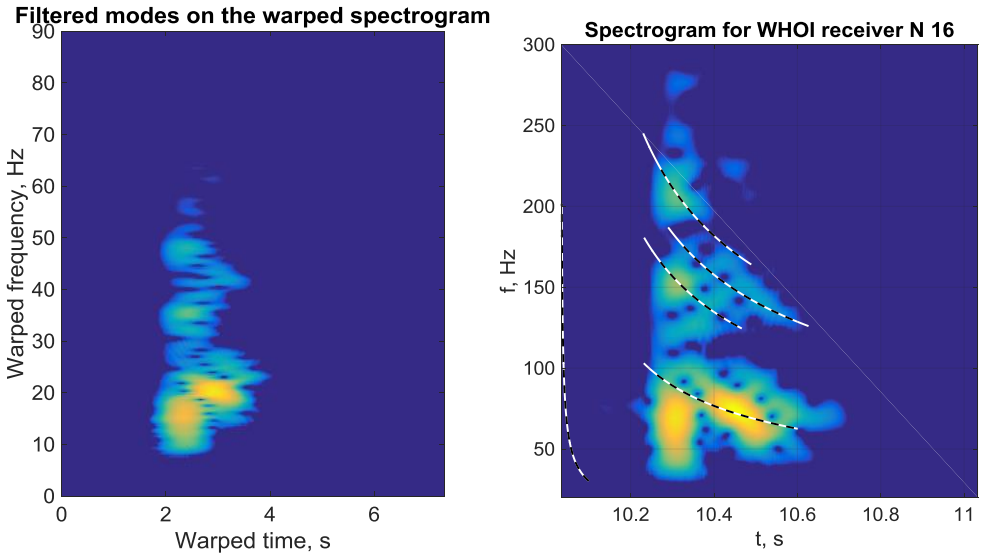

Figure 2.8. Spectrograms of warped signal (left) and original signal with mapped dispersion curves, based on warped spectrogram (right) where $\tau = 0{,}1$ s.

This example illustrates benefits of using later time of start of signal, if the beginning of the signal carries comparatively low energy.

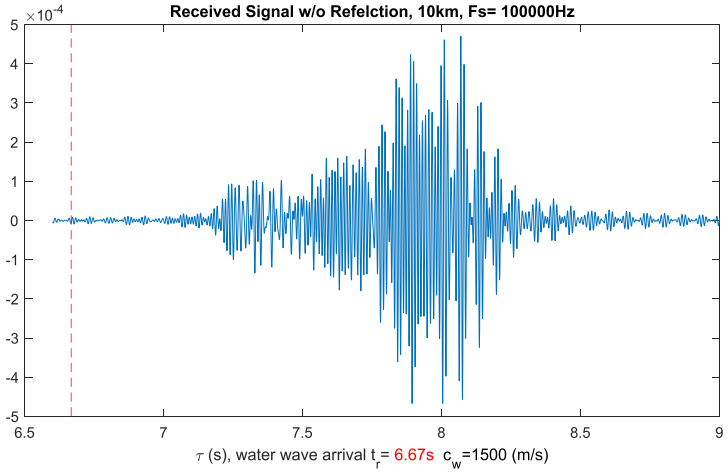

Figure 2.9. Theoretical signal calculated for tests for a distance of 10 km and sound speed in water 1500 m/s.

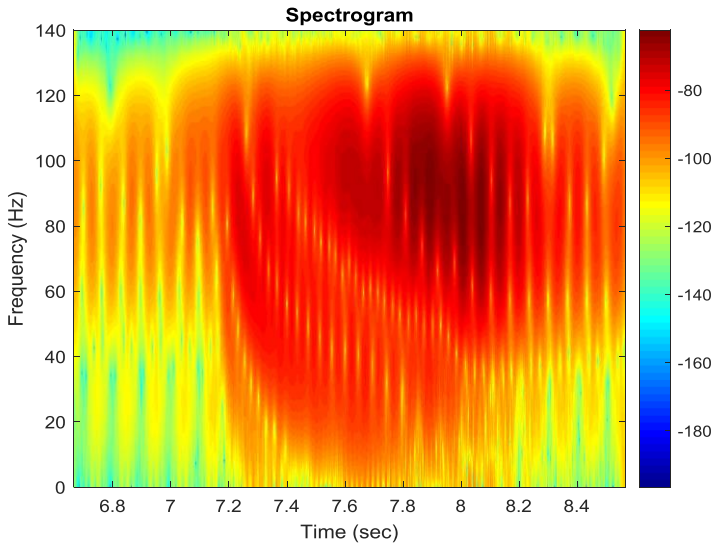

Figure 2.10. Spectrogram of original theoretical signal from Fig.2.7.

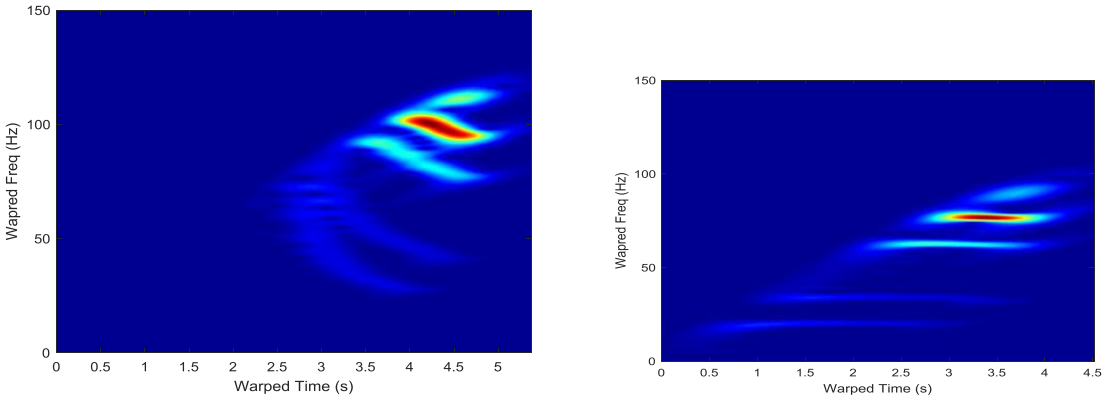

a b

Figure 2.11 a) Spectrogram of signal warped with tau=6.67 s, which is correct calculated time of arrival. Only 5 modes are visible (original signal contained 7 modes. b) Spectrogram of a warped signal, where tau=7.2 s. Two modes in the middle have low energies, but it is visible, that there is an empty space between first two and last three modes.

III. MANIFESTATION OF HORIZONTAL REFRACTION ON A SINGLE HYDROPHONE IN THE EXPERIMENT SWARM'95.

3.1 SWARM'95 Experiment

Experiment Shallow Water Acoustics in Random Media (SWARM'95) (Badiey et al, 2002) on the sound signals propagation in the shallow water waveguide was carried out in Atlantic shelf of USA by Woods Hole Oceanographic Institute (WHOI) and Naval Research Lab (NRL) and University of Delaware (UD). Two acoustic tracks of the length ~ 15 km with the angle ~ 35 between them were arranged, where two wideband sources were used (air-gun and J15) with the band ~ 30-300 Hz and two vertical arrays (WHOI VLA) at the acoustic track which is approximately parallel to the beach) and NRL VLA (acoustic track UDE source – WHOI VLA is shown in the Fig.3.1a).

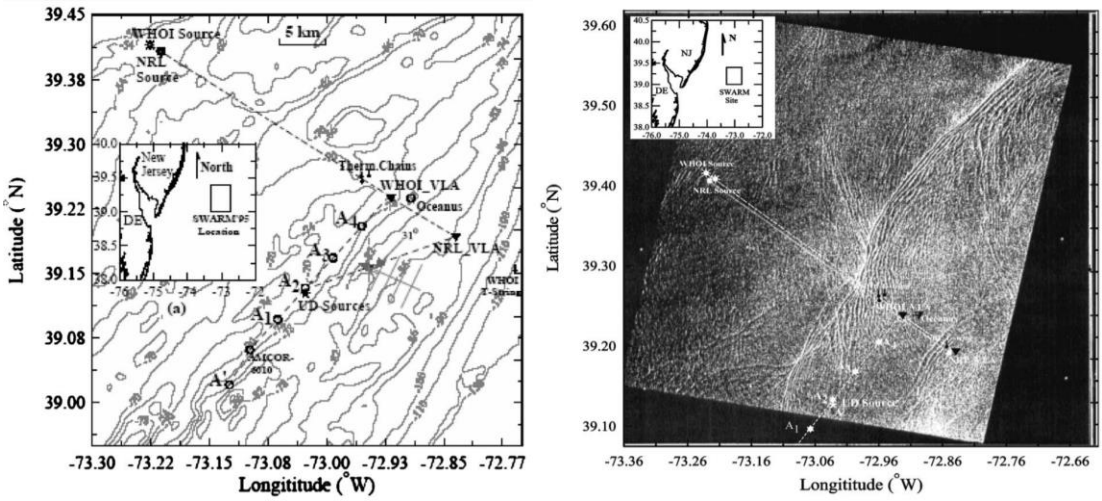

a) b)

Figure 3.1. a) Location and bathymetry of SWARM'95 experiment's oceanographic equipment. b) Satellite picture for 31 August 1995, showing internal wave activity at the experimental site.

UD source is air-gun, located 12 m below the sea surface, radiating wideband signals with band ~ 30-270 Hz every 60 sec. WHOI VLA contains 16 hydrophones, spanned the water column from 14.9 to 67.4 m, with hydrophone spacing 3.5 m. During time of experiment a few trains of

nonlinear internal waves (NIW) were passing through acoustic track (Fig.3.1b), producing sound intensity fluctuations registered by VLA. The most interesting observations were carried out in the presence of the nonlinear internal waves (NIW) passing through acoustic track with the angle about 5 degrees between wave front of NIW and direction of acoustic track, where fluctuations were registered due to the so called focusing/defocusing in horizontal plane takes place.

Intensity fluctuations were registered in the time interval 19:00 – 20:00 GMT 4th of August 1995. One of the main specific features of this phenomena is synchronicity of fluctuations for different waveguide modes, and the corresponding synchronicity of intensity fluctuations over depth. Theoretical explanation of this experiment was done in the paper (on the base of theoretical analysis and data processing using vertical line array, which allows us to filter waveguide modes on the base of standard methodology.

Figure 3.2 represents relative placement of airgun source and two arrays and map view of estimated direction of train of internal waves relatively to WHOI vertical array.

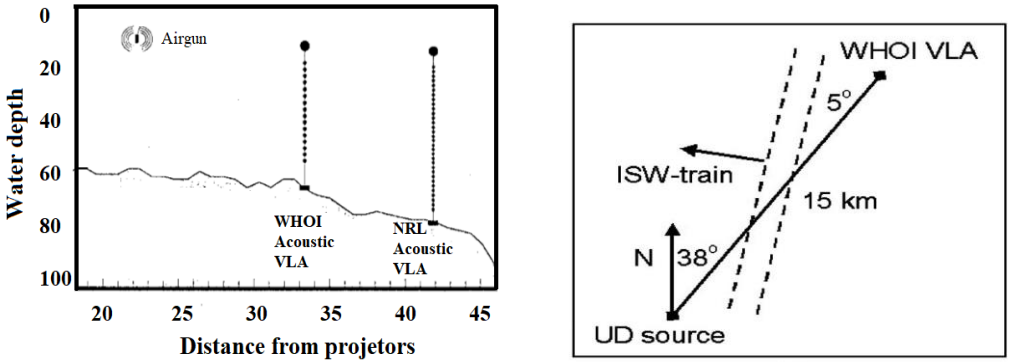

Figure 3.2. Vertical arrays and airgun placement used in our research (left). Schematic map view of internal wave front passing through the vertical arrays (right).

3.2 Airgun data from SWARM`95

3.2.1 NRL Array data

NRL is an array of 32 receivers passed by IW at 5-degree angle. Figures 3.3-3.5 represent the acoustic data we possess for this array in a form of intensity diagram per shot for each receiver of the array. This method of plotting is very useful for visualization of data, where internal waves can be presented.

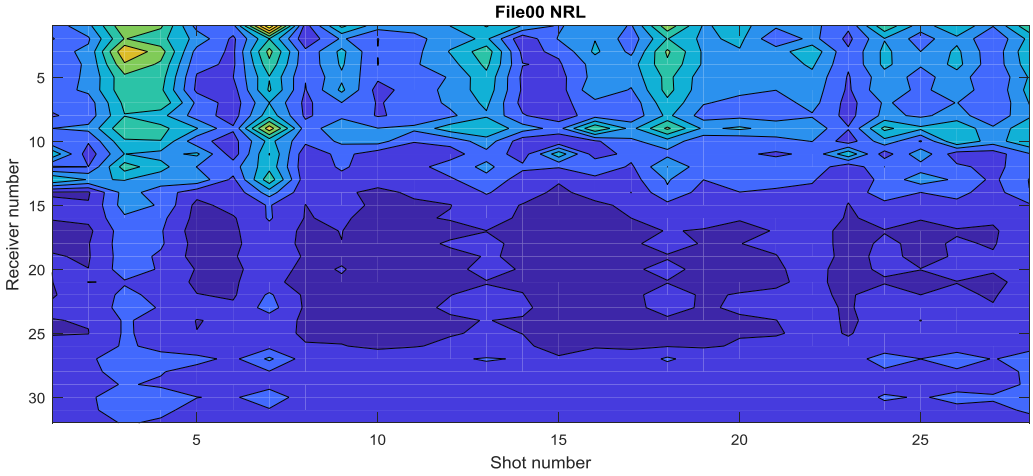

Figure 3.3 File00.mat visualized as signal energy for each airgun shot. 06:27:16-06:37:00, source depth was 15 m.

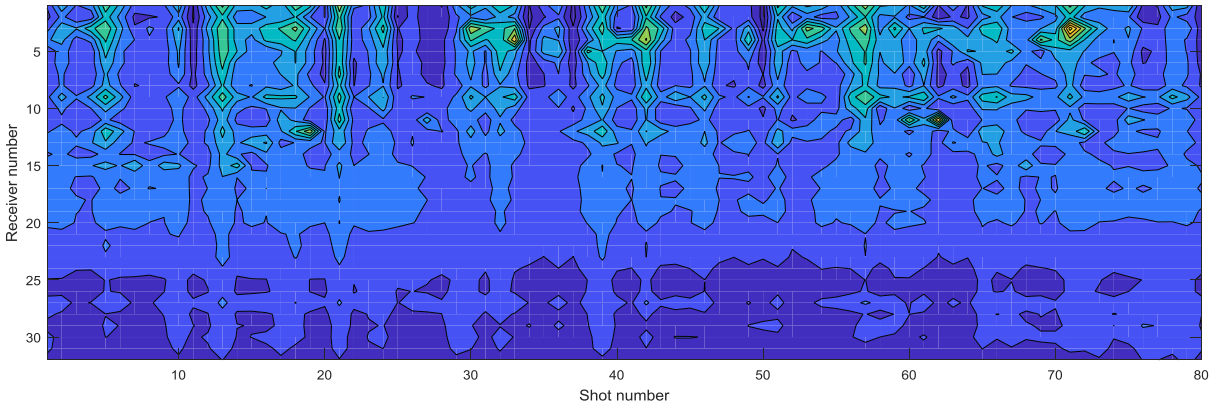

Figure 3.4 File01.mat visualized as signal energy for each airgun shot. Airgun location depth was 35 m. GMT time 06:38: 00-07:06:00.

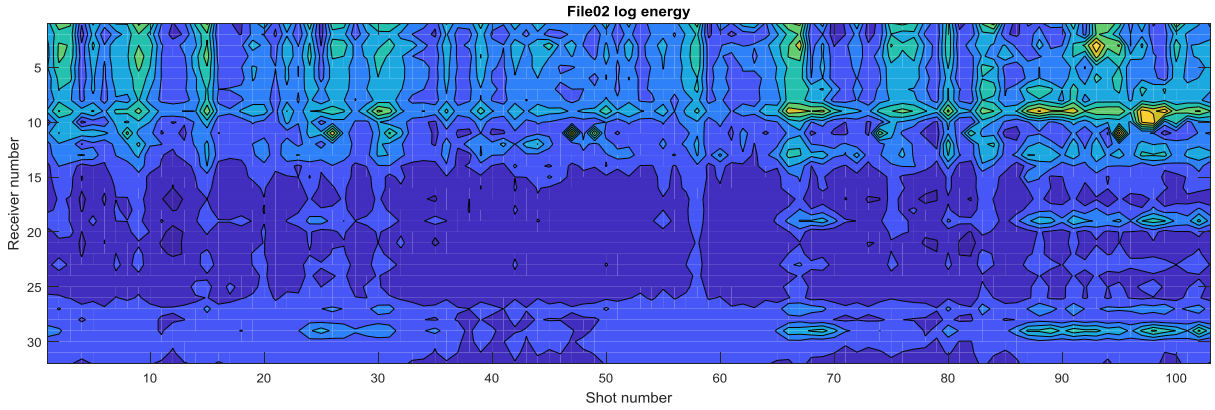

Figure 3.5 File02.mat visualized as signal energy for each airgun shot. Air gun location depth was 15 m. GMT time: 07:10:00-07:46:00.

3.2.2 WHOI Array Data

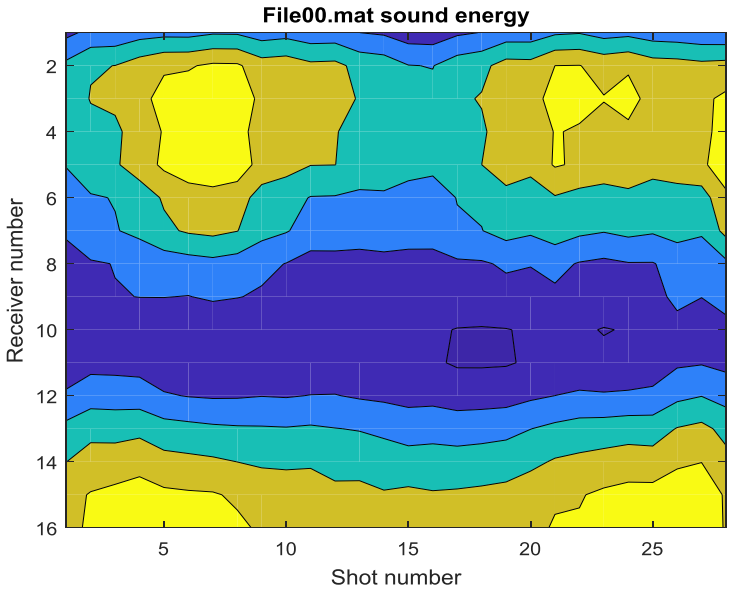

Figure 3.6. File 00.mat visualized as signal energy for each airgun shot. Airgun location depth was 15 m. 06:27:16-06:37:00.

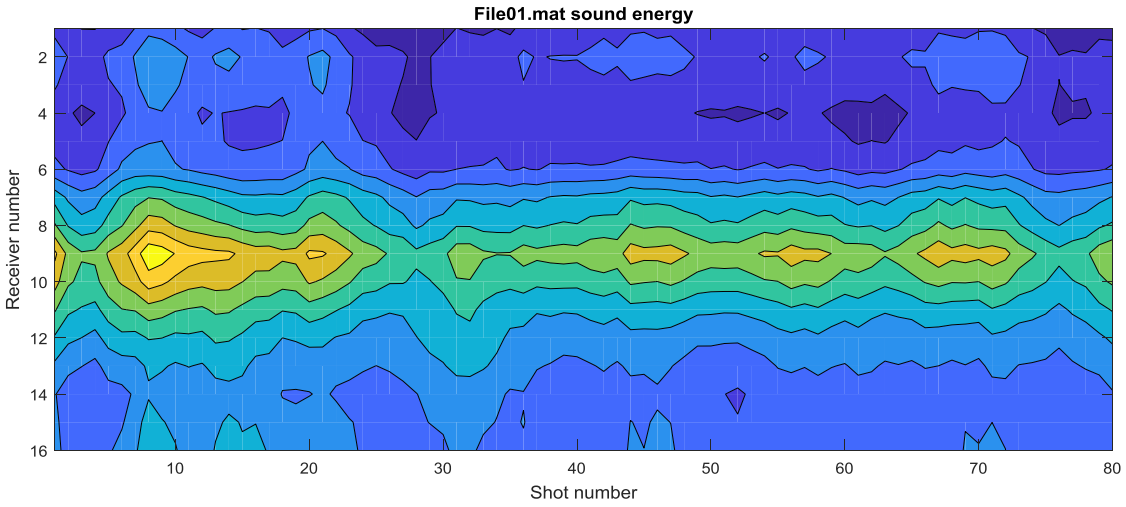

Figure 3.7. File01.mat visualized as signal energy for each airgun shot. Airgun location depth was 35 m. GMT time 06:38: 00-07:06:00

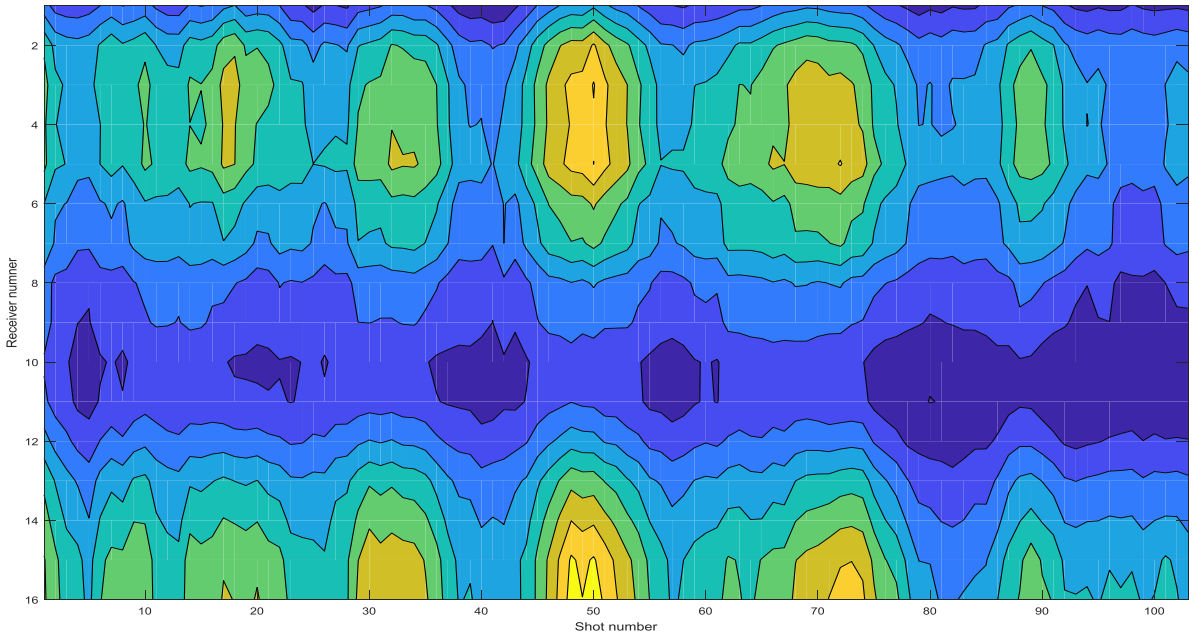

Figure 3.8. File 02 visualized as signal energy for each airgun shot. Air gun location depth was 15 m. GMT time: 07:10:00-07:46:00

Figures 3.6-3.8 represent acoustic data received using WHOI array without noticeable influence of horizontal refraction. The interval of the airgun signals is about 20 seconds for this dataset. During JD216 06:27:16-06:37:00, the ship was moving toward the two receivers in a straight line. During JD216 06:38:00-07:06:00, and JD216 07:10:00-07:46:00, the ship was drifting around.

Other datasets are signals recorded on WHOI VLA 4th of august 1995 19:00-20:00 presented on Fig.3.11 for WHOI array and 20:00-21:00 that we had not found.

3.3 Horizontal refraction

Let's consider sound field from the wideband source placed in the horizontal plane with coordinates (0,0). If there is the train of NIW passing through acoustic track then sound field changes in time *(T)*, on receiving array. Sound field on the VLA, placed at the point in horizontal plane with coordinate (*x,y*) has the form:

$$P(x,y,z;t) = \sum A_l(T)\Psi_l(z)\exp\left(iS(x,y)\right) \quad , \tag{3.1}$$

where *A(T)* is amplitude of "vertical" mode *l*, *S(x,y)* is phase function (eikonal) in horizontal plane, describing horizontal rays, z is the depth of receiver. Modal functions evaluated for conditions of the SWARM experiment and their dispersion curves on a distance of 15 km are shown on figure 3.9.

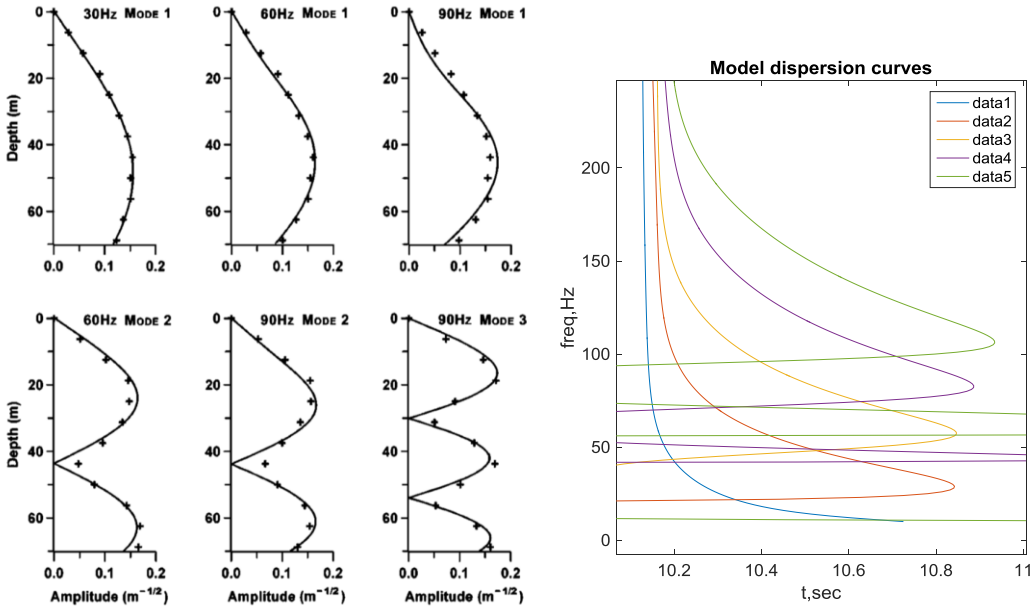

Figure 3.9 Model of $\psi_l(z)$ functions for SWARM experiment conditions (left) and modeled dispersion curves for modes 1-5 (right)

We can suppose that waveguide modal functions at the VLA practically do not change in time and all the variations of the sound field are provided by modal amplitudes $A_l(T)$. Intensity of separate mode on the single hydrophone (or at the fixed depth z) is:

$$I_l = |A_l(T)\Psi_l(z)|^2 \tag{3.2}$$

Figure 3.10 explains unevenness of intensity in time of the signals received on WHOI array. In presence of internal waves ray model (Fig.3.10) shows the manifestation of focusing and defocusing of sound energy on horizontal plane in the area of source-receiver track.

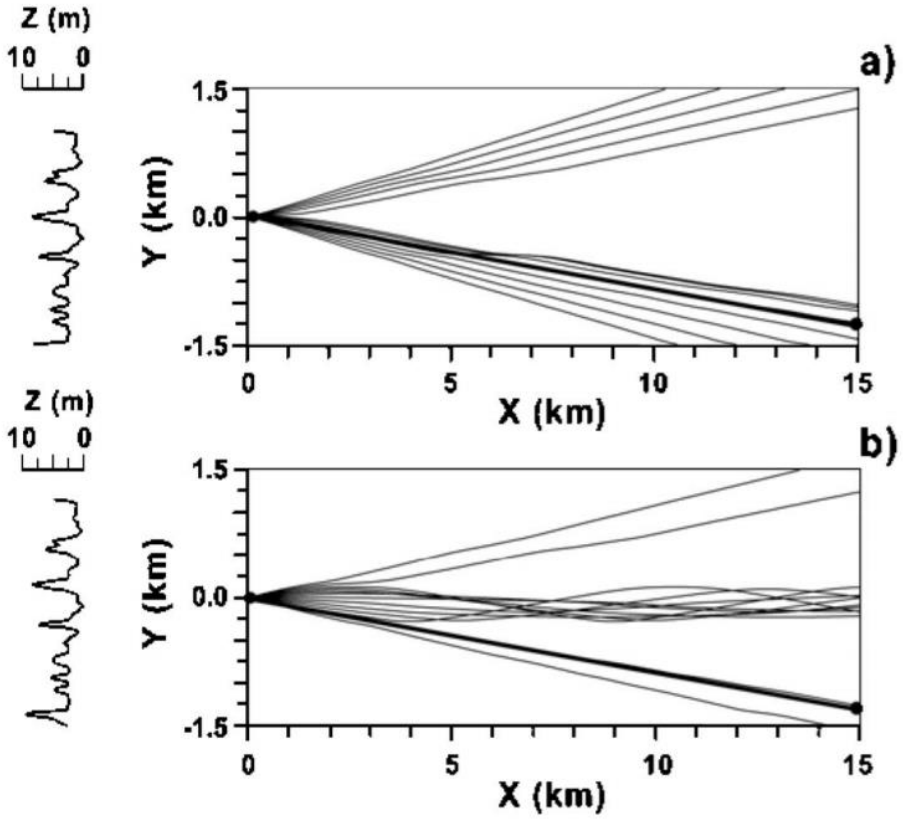

Figure 3.10 a) Ray theory calculation of the acoustic field in the horizontal plane corresponding to geotime 19:16 GMT, showing defocusing by horizontal refraction and an energy maximum; b) same as a), but corresponding to geotime 19:22 GMT, showing focusing and an energy minimum. Corresponding ISW positions are shown to the left of each plot, and bold straight lines denote the source–receiver track.

Experimental evidence of horizontal refraction was presented in the papers (Badiey et al, 2005, 2007), where we can list specific features, characterizing fluctuations of the sound field just due to horizontal refraction, initiated by nonlinear internal waves:

(i) significant fluctuations of intensity with period ~ 12-15 min, corresponding to the Vaisala period for given temperature (density) profile, and in turn, to the period of NIW;

(ii) Synchronicity of fluctuations over depth (focusing/defocusing) for all the waveguide modes

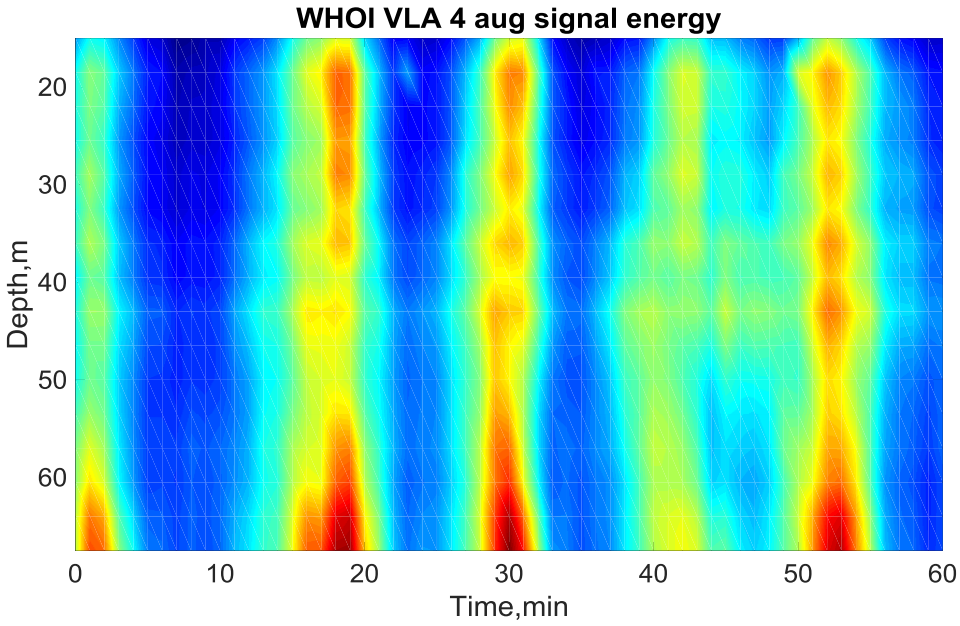

Figure 3.11 Temporal dependence of depth distribution of the sound intensity.

In the Fig.3.11 total intensity (summarized over all the modes) is shown. Let's consider modal decomposition of the sound field using sound field recorded by the single hydrophone only. In the Fig.3.12 spectrogram of pulse is shown, where we can see dispersion curves, corresponding to four modes, giving contribution to the sound field.

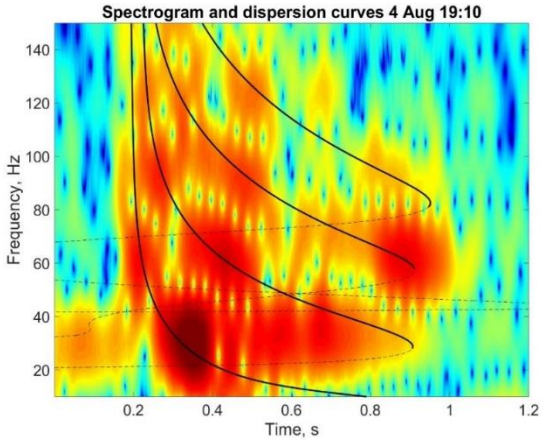

Figure 3.12 Spectrogram of one pulse of air-gun. Solid lines show the corresponding frequency dependence of modal group velocities calculated using KRAKEN program.

In order to get amplitude of separate mode let's use Warping Transform (Baranyuk et al. 1995) which is defined as some transform for interpolation of the input signal *P(t)* on the deformed time-axis.

Main properties of the Warping Transform are:

1) Existence of inverse WT;

2) Conservation of L2 norm;

3) Variation of the spectrogram: dispersion curves become straight lines for the ideal waveguide (Pekeris model).

The corresponding WT spectrogram is shown in the Fig.3.13 Time of beginning is separate parameter in WT. It was underlined in the paper [37] that mode filtering becomes better for increasing of parameter r/c. In given paper positions of rectified curves was considered in the process of choice. Norm conservation is approximate in the process of WT usage due to part of the first mode can be cut out. At the same time for qualitative estimation this approximation seems to be enough.

After application of the inverse Warping Transform it is possible to get amplitudes of each mode an and the corresponding modal intensity In. In the Fig.3.14 temporal dependence of modal intensities (3.2) are shown. We can see different maximal values of intensities due to different values of eigen functions for given depth and synchronous variation in time for all four modes. Remark that on the figure 3.14 modal intensities were presented in relative units, which means, that the magnitudes of modal intensities on the plots should not be compared to each other.

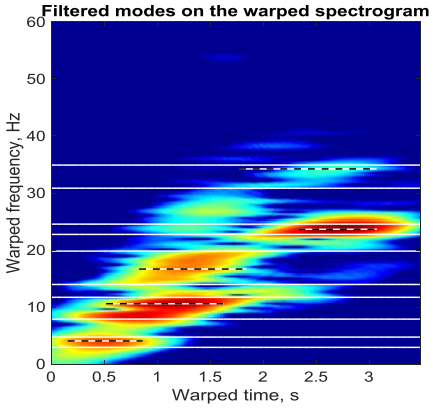

Figure 3.13. WT spectrogram for pulse in the Fig.3.12

Using warping transform, we calculated integrals of intensity of each mode stripe over warped signal spectrogram.

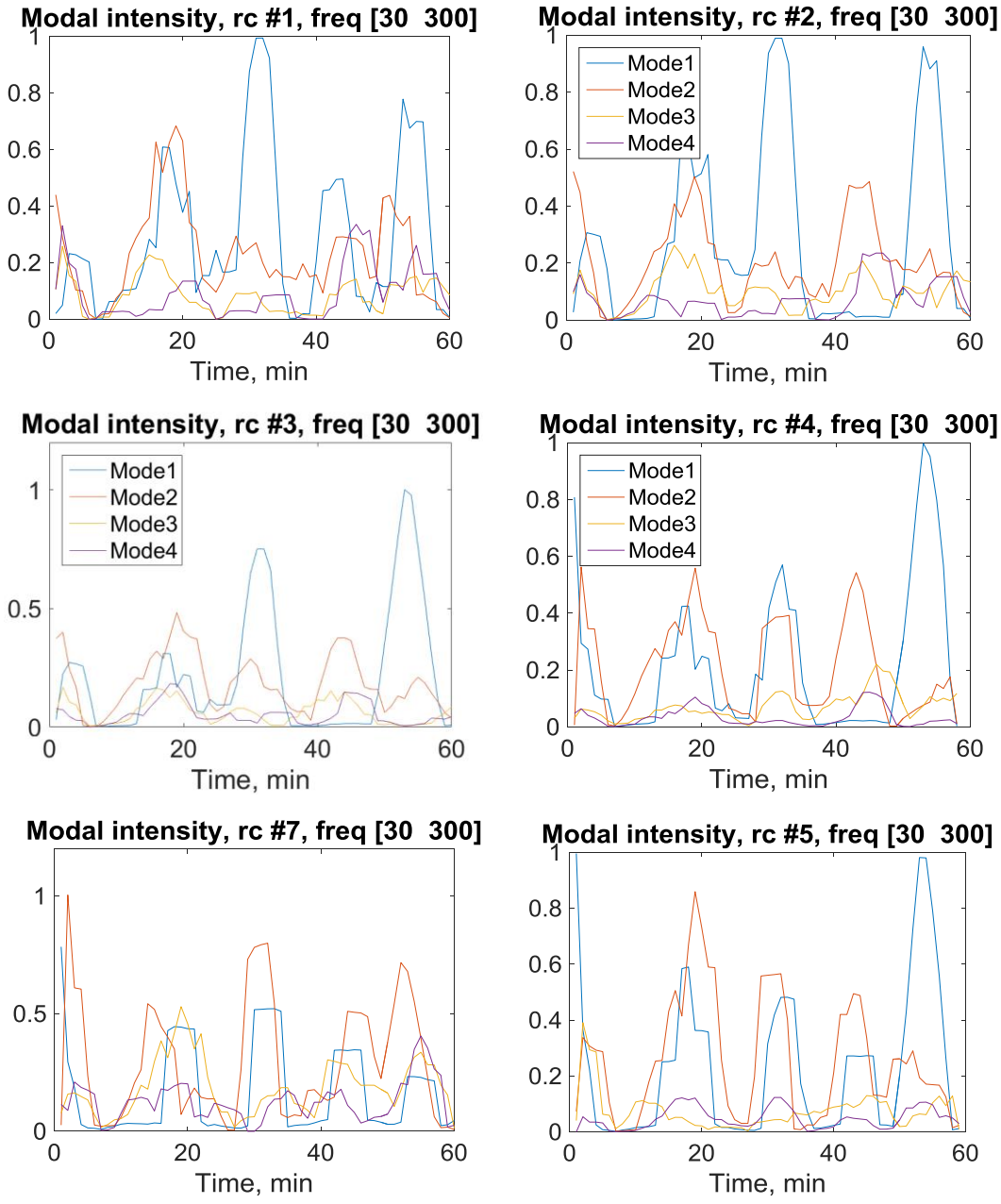

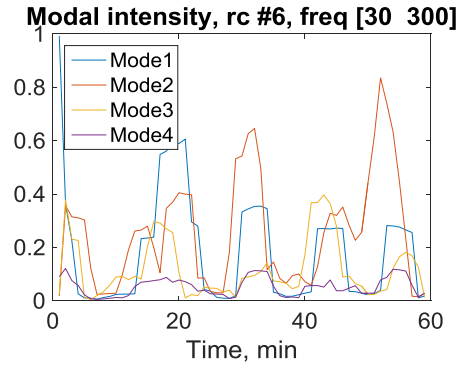
Modal intensity, rc #6, freq [30 300]
Mode1
Mode2
Mode3
Mode4
Time, min

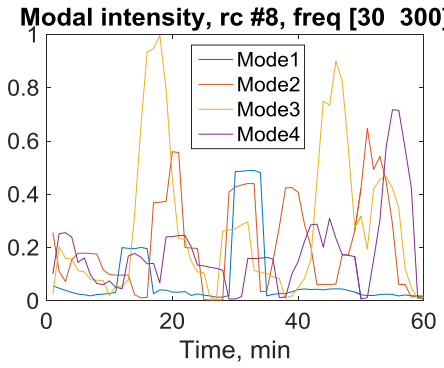
Modal intensity, rc #8, freq [30 300]
Mode1
Mode2
Mode3
Mode4
Time, min

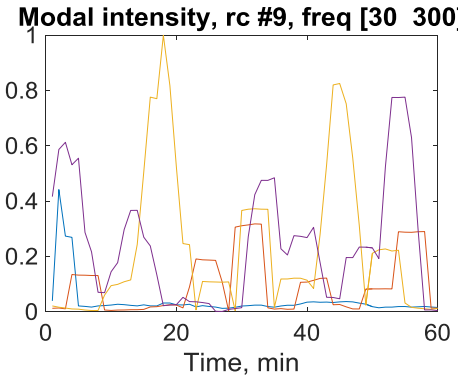
Modal intensity, rc #9, freq [30 300]
Time, min

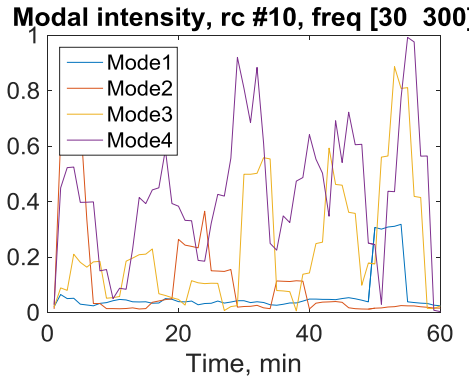
Modal intensity, rc #10, freq [30 300]
Mode1
Mode2
Mode3
Mode4
Time, min

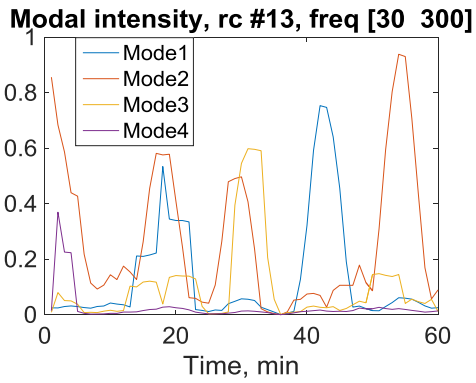
Modal intensity, rc #13, freq [30 300]
Mode1
Mode2
Mode3
Mode4
Time, min

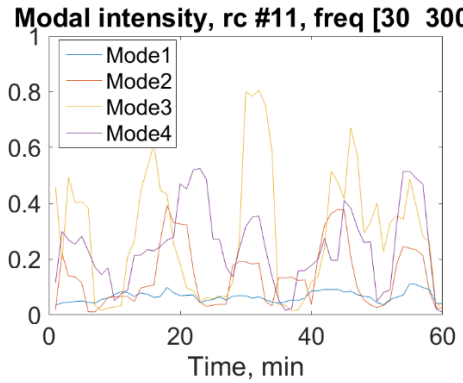
Modal intensity, rc #11, freq [30 300]
Mode1
Mode2
Mode3
Mode4
Time, min

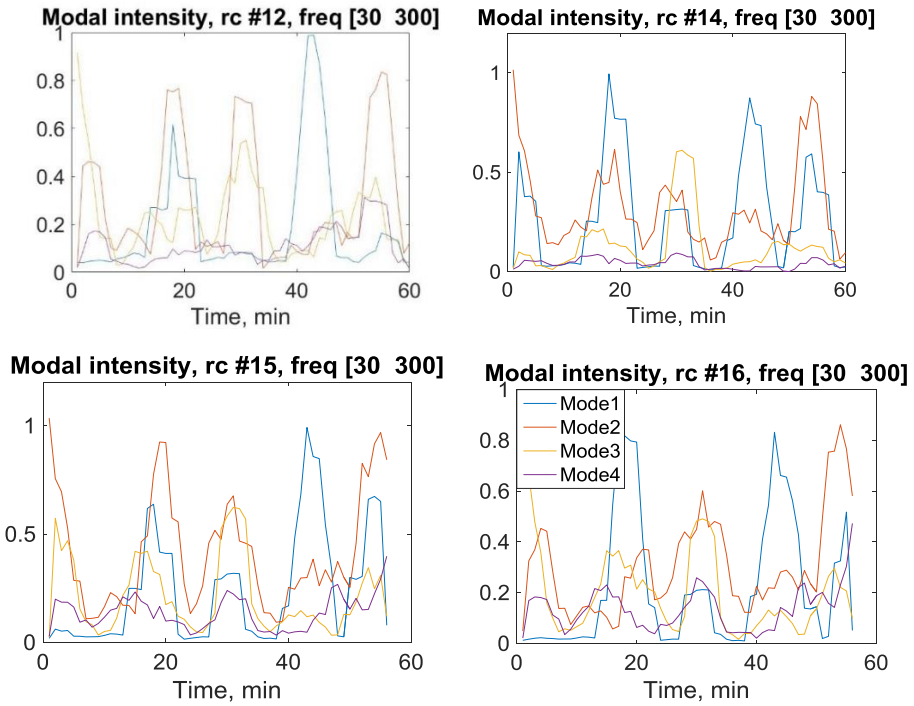

Figure 3.14 Mode intensities in relative units evaluated for hydrophones of WHOI array in frequency band 30-300 Hz.

Results of data processing using WT are presented for August 4, 1995, 19-20 GMT. For each from 60 signals received by 16 hydrophones WT was used, and the corresponding spectrogram was constructed and integrated over time. It allows us to separated maximums $f_w^n(t)$ - frequencies of warped modes. 4 modes were selected.

As usually [19,38,39,40] warped dispersion curves are approximated by one frequency $f_w^n(t) = const$. In given paper for estimation of intensity of modal components we take into account width of maximums on warped dispersion curve. Modal amplitude is integral over area containing peak at the frequency $f_w^n(t)$.

In the Fig. 3.15 temporal dependence for depth distribution of total intensity along with the corresponding functions for three lowest modes are shown.

Scintillation index

We can clearly see synchronicity of variation of different modes and synchronicity of variations over depth what acknowledge 3D nature of given phenomena. Using these data we can find scintillation index for intensities of modes,

$$S_n^2(T) = (\langle I_n^2(T)\rangle - \langle I_n(T)\rangle^2)/\langle I_n(T)\rangle^2 \quad (3.3)$$

which is proportional to the refraction index for the corresponding modes in horizontal plane, here we define $I_n(T) = A_n^2(T)\psi_n(z,T)$, where T is Geotime (equivalent to the time of the airgun shot) and modal function can be canceled and scintillation index SI does not depend on the depth of hydrophone. Results of calculations is shown in the Fig.3.16, which gives frequency dependencies close to obtained in [27].

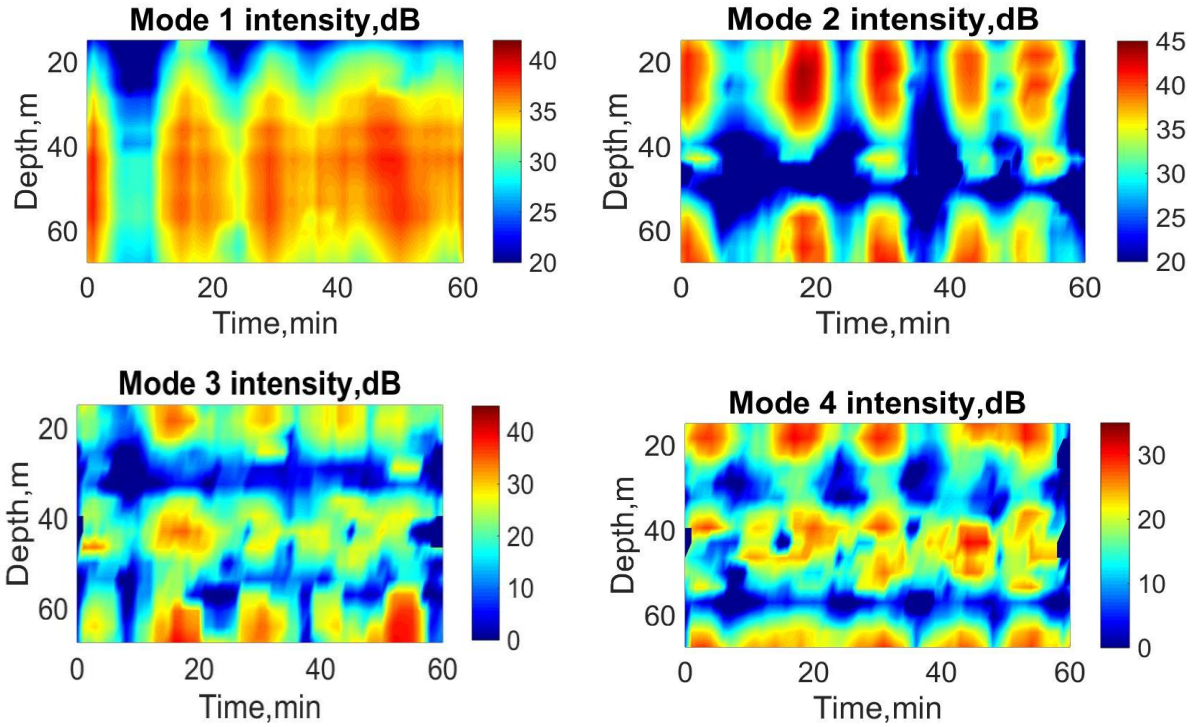

Fig.3.15. Temporal dependence of total intensity and intensities of the lowest four modes.

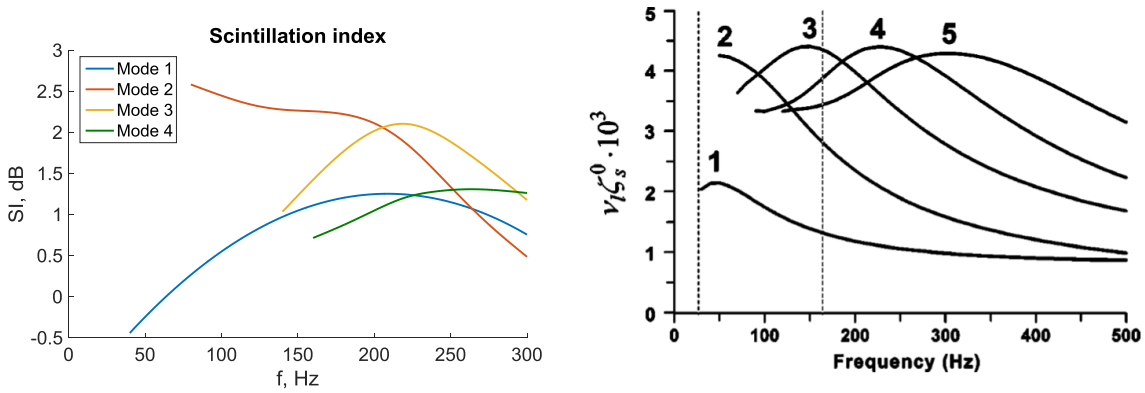

Figure 3.16 On the upper picture: Scintillation indices calculated using single hydrophone data. On the lower picture: Theoretically evaluated Refraction indices from Badiey et al. [27]. Here ν_l is some oefficient, $\varsigma_s^0$is amplitude of internal wave and $\nu_l \varsigma_s^0 = n_l(x, y)$.For calculation of SI signals from hydrophone 16 were taken, next they were filtered with the width 20 Hz, with the following shift by 5 Hz, for each step. Calculated modal amplitudes were smoothed in frequency domain. Figure 3.17 illustrates the process of warping of a filtered signal and automatic mode selection in it.

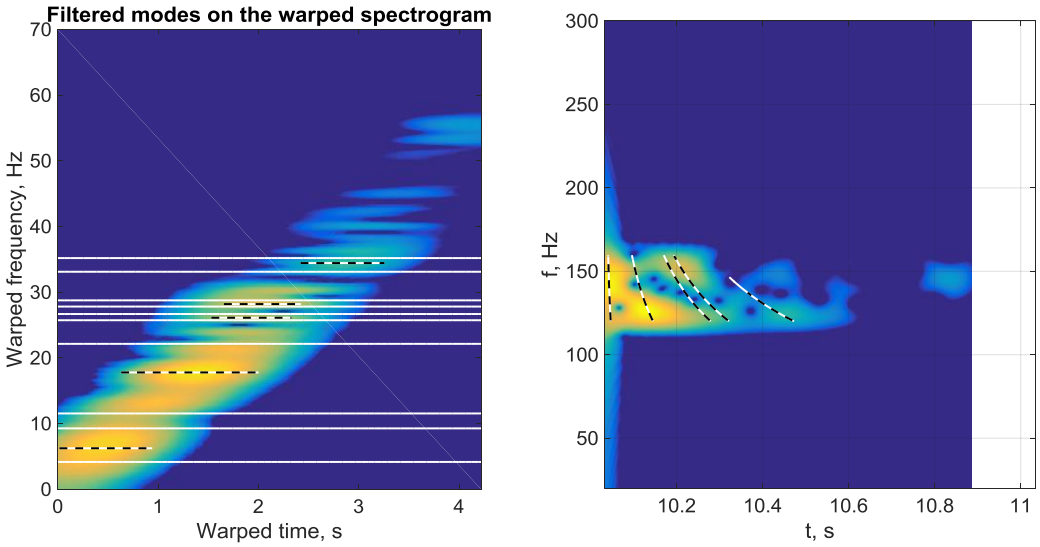

Figure 3.17 Example of modal separation for frequency band of 120-160 Hz.

On the Figure 3.18 calculated SI`s were presented before and after smoothing. SI calculated for receiver 10 located on 50-m deep, where 1st and 4th modes are the strongest, according to model of modal functions presented on Fig.3.9.

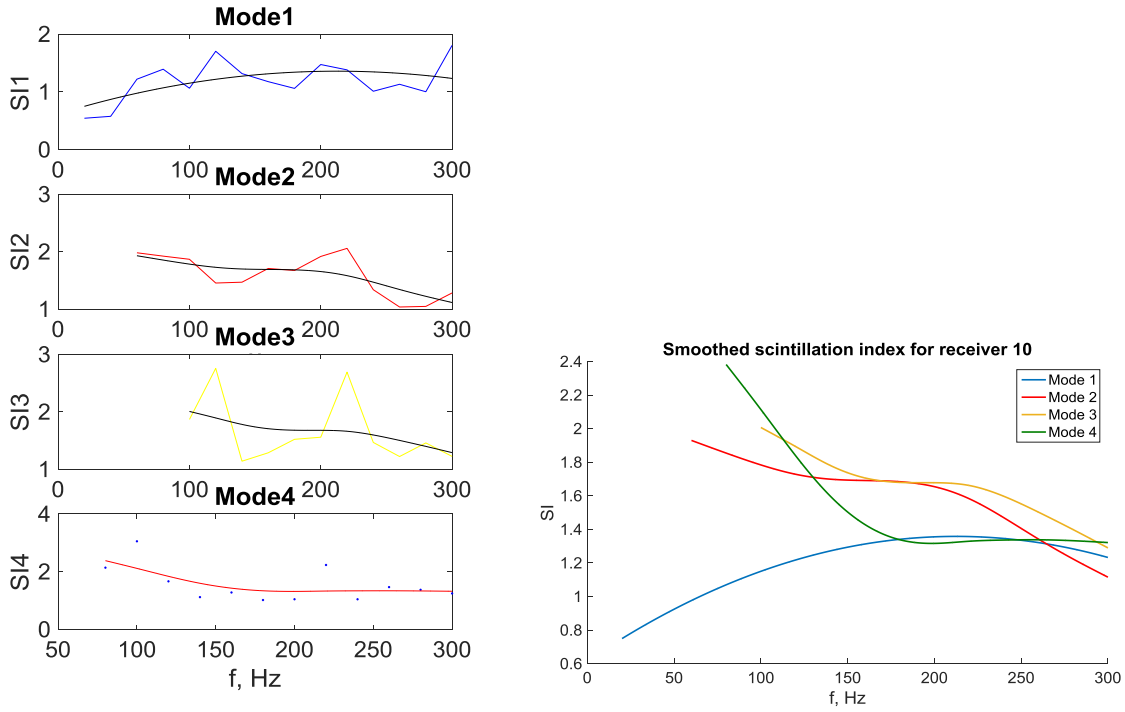

Figure 3.18. SI calculated for receiver 10 located on 50-m deep, before and after smoothing.

Parameters of warping transform can change a lot in calculation of SI. If time of start of the signal is set not right, in some cases, first mode might be not found, and second will be counted as first etc. Or, if time of start is too early, modes can be separated poorly because of not strong enough influence of warping. On Fig.3.19 we see scintillation indexes calculated for different warping parameters τ. We discussed more of influence of this parameter in Chapter 2.

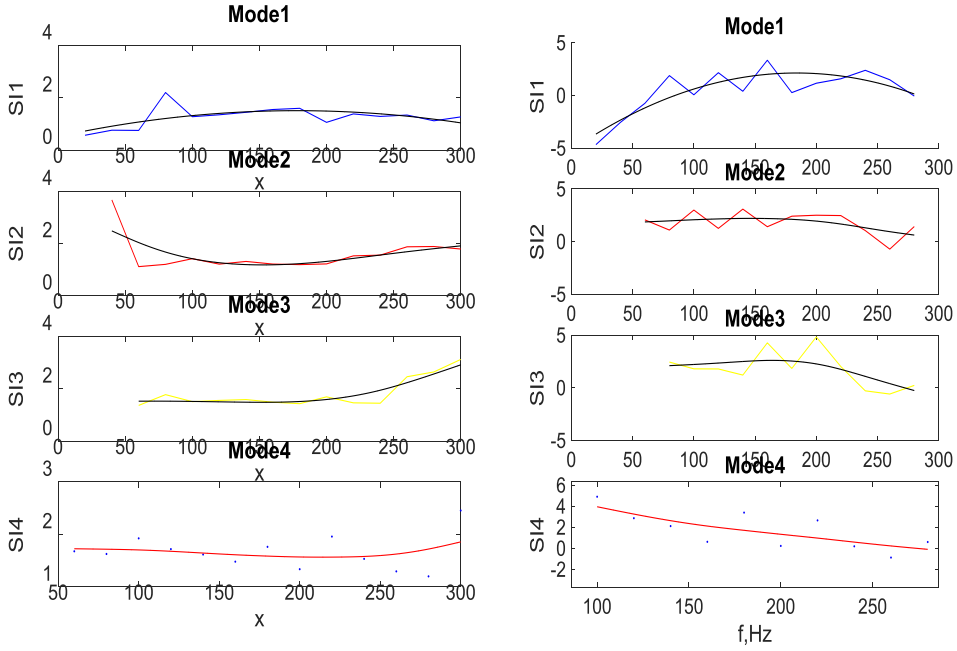

Fig 3.19. SI for receiver 16 calculated for earlier (left) and later (right) start of signal time τ used for warping transform.

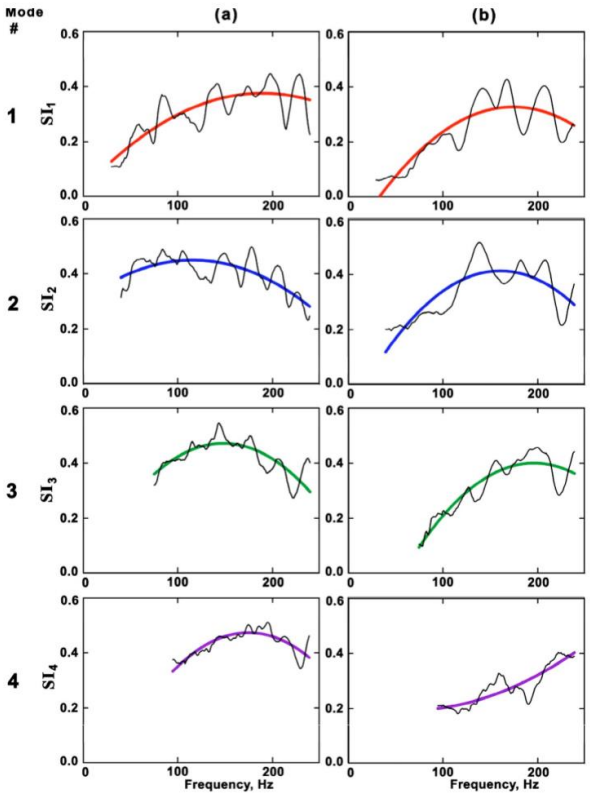

Figure.3.20 Frequency dependent SI from [32]

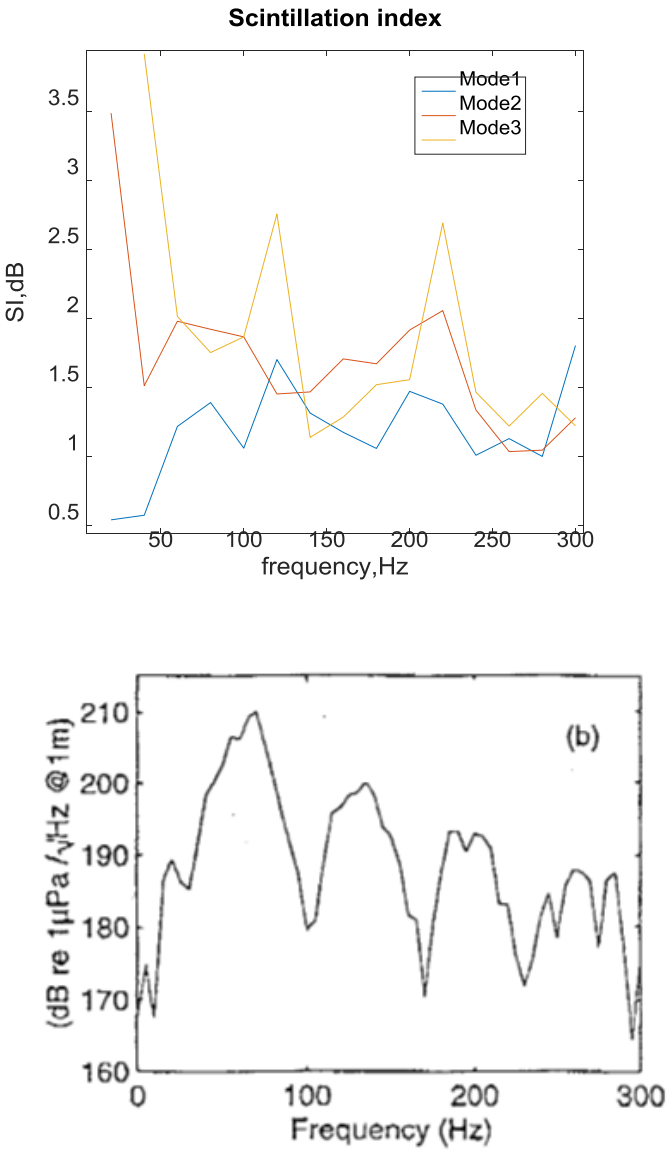

Fig.3.21 SI calculated without smoothing for receiver 10 vs Source power spectrum.

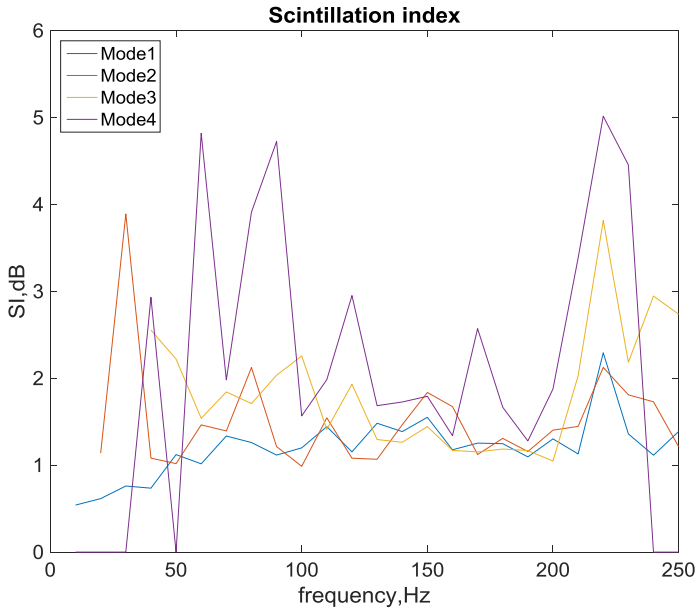

Figure 3.22 SI calculated for receiver 15 with 10 Hz step with no smoothing.

We should notice, that smoothing of scintillation index is necessary not only for SI calculated using single hydrophone approach. In paper (Badiey et al, 2007) oscillations of SI were also present in case of modal separation using orthogonal functions and vertical array data, as presenter on Fig.3.20.

Another reason why oscillations of SI appear in calculations is that spectrum of airgun signal was not flat. On Fig. 3.21 not smoothed SI calculated for receiver #10 is matched to spectrum of airgun signalFrequency band that we choose for calculating SI also plays an important role. In one hand, we want it to be as narrow as possible to make frequency dependence accurate. In the other, when a frequency band to retrieve modes is too narrow (Fig. 3.22), we have too many oscillations, especially in higher modes because in some signals where they are present, they are not found by the program.

IV. WARPING TRANSFORM AND GEOACOUSTIC INVERSION.

4.1 Normal mode dispersion and time warping in the coastal ocean

Simple, analytically solvable models of normal mode propagation in the coastal ocean are developed and applied to study the effect of the seafloor bathymetry on modal travel times. Within the adiabatic approximation, horizontal inhomogeneity of the waveguide is found to change the modal dispersion curves in a way that helps separation of the modal components of the acoustic field using the time-warping transform. It is shown that moderate seafloor slopes can lead to surprisingly large errors in retrieved geoacoustic parameters and cause a positive bias in bottom sound speed estimates if horizontal refraction is ignored.

Time-warping transform[1] has been very successful and is increasingly employed in shallow water acoustics to isolate normal mode components of the field due to a compact, broadband sound source (Bonnel et al, 2011, 2013), (Ballard et al, 2014) or two-point cross-correlation function of diffuse noise, (Sergeev et al, 2017), (Tan et al, 2018) and to measure mode travel times as a function of frequency. The time-warping transform was developed for range-independent waveguides with pressure release or rigid boundaries (Le Touze et al, 2009). Dispersion curves in range-independent shallow-water waveguides are qualitatively different from the ideal waveguide by having an anomalous dispersion, or ground wave, part (Brekhovskikh, 1960). Physical parameters of the ocean are never quite constant in the horizontal plane, and bathymetry variations are typically responsible for a major part of the waveguide's horizontal inhomogeneity in the coastal ocean. In this Letter, using simple models of the coastal ocean we show that seafloor slopes contribute to the success of the warping technique by making mode dispersion curves more similar to the dispersion curves in an ideal waveguide. We also show that seafloor slopes may provide an explanation for the observation[2, 3, 8] that warping-based geoacoustic inversions of mode travel times tend to return higher estimates of sound speed in the seabed than other inversion techniques.

Introduce a Cartesian coordinate system with horizontal coordinates x and y and a vertical coordinate z. Let a homogeneous fluid layer with sound speed c and density ρ be located between plane boundaries $z = 0$ and $z = H$ with normal impedances Z_0 and Z_H, respectively. By imposing the boundary conditions of impedance continuity at $z = 0$ and $z = H$ on the solution of 1-D wave equation in the homogeneous fluid layer, we obtain the dispersion relation

$$\tan\left(\omega H\sqrt{c^{-2}-c_n^{-2}}\right)=i\rho\sqrt{c^{-2}-c_n^{-2}}\,\frac{Z_0+Z_H}{\rho^2+\left(c^{-2}-c_n^{-2}\right)Z_0Z_H} \qquad (4.1)$$

of the acoustic normal modes supported by the waveguide. Here ω and c_n are the wave frequency and phase speed of n-th normal mode, $n = 1, 2, \ldots$. If the impedances depend only on the angle of incidence of a plane wave (or, equivalently, on c_n) and are independent of ω, wave frequency enters the dispersion equation (1) only in the combination ωH. We will refer to such media as simple waveguides, for brevity. Examples of simple waveguides include a fluid layer with ideal (pressure-release and/or rigid) boundaries, a layer with a pressure-release boundary $z = 0$ and a homogeneous fluid (Pekeris waveguide) or solid half-space at $z > H$, etc. Using well-known input impedances of fluid and solid half-spaces, (Brekhovskikh, 1960) it is straightforward to check that Eq. (4.1) reduces to previously established normal mode dispersion relations in these special cases.

We use simple waveguides to model sound propagation in the coastal ocean. If water depth H depends on x and y, the waveguide becomes horizontally inhomogeneous. (Horizontal gradients of the sound speed also make the waveguide horizontally inhomogeneous but are not considered in this Letter.) Then, within the adiabatic approximation, also known as the vertical modes and horizontal rays theory (Weinberg et al, 1974) Eq.
Error! Reference source not found. determines phase speed and the group speed $u_n=\left[\partial\left(\omega c_n^{-1}\right)/\partial\omega\right]^{-1}$ of adiabatic normal modes at each horizontal position (x, y). Consider downslope propagation in a coastal wedge, where water depth $H(x)=H_0+x\cot\alpha$. In the adiabatic approximation, travel time of n-th normal mode

$$T_n=\int\frac{dx}{u_n}=\cot\alpha\int_{H_1}^{H_2}\frac{dH}{u_n(\omega,H)}. \qquad (4.2)$$

Here H_1 and H_2 are the water depths at the source and receiver locations, $H_1 < H_2$; α is the angle that the seafloor makes with the horizontal plane. At upslope propagation, mode travel time is again given by Eq. (4.2), where H_1 and H_2 are now the receiver and source depths, respectively. Since the phase speed c_n depends on ω and H only via the combination ωH,

$$\frac{1}{u_n}=\frac{1}{c_n}+\omega\left(\frac{\partial}{\partial\omega}\frac{1}{c_n}\right)_H=\frac{1}{c_n}+\omega H\,\frac{d}{d(\omega H)}\frac{1}{c_n}=\frac{1}{c_n}+H\left(\frac{\partial}{\partial H}\frac{1}{c_n}\right)_\omega=\left(\frac{\partial}{\partial H}\frac{H}{c_n}\right)_\omega . \qquad (4.3)$$

Substitution of the right-most side of Eq. (4.3) into Eq. (4.2) gives a closed-form expression for mode travel time:

$$T_n = \left[\frac{H_2}{c_n(\omega, H_2)} - \frac{H_1}{c_n(\omega, H_1)} \right] \cot\alpha. \qquad (4.4)$$

It is straightforward to extend this result to a more complicated bathymetry, where water depth is piece-wise linear function of x. Then, the mode travel time is given by the sum of contributions Eq. (4.4) in each segment with a constant bottom slope, the slope α being different in each segment.

In the particular case of a wedge with pressure release (impedance $Z = 0$) and/or rigid ($Z = \infty$) boundaries, the dispersion relation (4.1) gives the well-known expressions

$$c_n = c\left(1 - F_n^2 f^{-2}\right)^{-1/2}, \quad u_n = c^2/c_n, \quad F_n = (n-\beta)c/2H \qquad (4.5)$$

for the phase and group speeds. Here $f = \omega/2\pi$, F_n is the cutoff frequency of n-th normal mode, $\beta = 0.5$ if one boundary is pressure-release and the other is rigid, $\beta = 0$ or 1 when both boundaries are pressure release or rigid, respectively. Using Eq. (4.5), it is easy to integrate over H in Eq. (4.2) and verify validity of Eq. (4.4) in this particular case.

At upslope propagation in a waveguide with ideal boundaries, the group speed turns to zero at the mode cutoff. Nevertheless, the mode travel time to the mode's cutoff is finite in the wedge: $T_n = H_2 \cot\alpha / c_n(\omega, H_2)$ according to Eq. (4.4), since the phase speed c_n in Eq. (4.5) is infinite at the cutoff. If a source and a receiver are located at points (x_1, y, z_1) and (x_2, y, z_2) and the smaller of water depths $H_1 = H(x_1)$ and $H_2 = H(x_2)$ is larger than the depth at the cutoff of n-th normal mode, there will be two arrivals of the mode. One arrival corresponds to a direct, up- or downslope path. The travel time for this arrival is given by Eq. (4.4). On the other path, normal mode first propagates from the source upslope to the mode's cutoff, is totally reflected there (Brekhovskikh et al, 1999) and then propagates downslope to the receiver. The travel time on the reflected path differs from that on the direct path by replacing the minus sign with plus in the brackets in the right side of Eq. (4.4).

Up- and downslope propagation in a wedge with either fluid or solid penetrable bottom can be analyzed in a similar fashion. In particular, when the bottom is a fluid with sound speed $c_b > c$

and density $\rho_b = m\rho$, the impedance $Z_H = im\rho\left(c_n^{-2} - c_b^{-2}\right)^{-1/2}$, and it follows from the dispersion relation (4.1) that phase and group speeds at the mode cutoff equal c_b, and cutoff frequencies $F_n = (2n-1)\left(c^{-2} - c_b^{-2}\right)^{-1/2} \big/ 4H$ (Brekhovskikh et al, 1999). Using Eq. (4.4), we find mode travel time to its cutoff at upslope propagation from a source at (x_2, y, z_2):

$$T_n = \left[\frac{H_2}{c_n(\omega, H_2)} - \frac{(2n-1)\pi}{2\omega\sqrt{c_b^2 c^{-2} - 1}} \right] \cot\alpha. \qquad (4.6)$$

In the limit $c_b \to \infty$, Eq. (4.6) reduces to the rigid-bottom result given above, as expected.

In horizontally inhomogeneous waveguides, adiabatic normal modes propagate along horizontal (modal) rays, which generally have non-zero curvature, except when cross-range environmental gradients, including the cross-range slope of the seafloor, equal zero. Since waveguide parameters are independent of the cross-slope horizontal coordinate y in the coastal wedge, the y-component of the wave vector (k_x, k_y, 0) of the mode is constant along the modal ray; $k_x^2 + k_y^2 = \omega^2 / c_n^2$ (Weinberg et al, 1974). Let $H(x) = x\cot\alpha$, $0 < \alpha < \pi/2$. Then x-component of the wave vector increases with x on the modal ray. If $k_x > 0$ at the source, the mode propagates towards increasing x, i.e., deeper water. If $k_x < 0$ at the source, the mode propagates towards the coastline, reaches a turning point, where $k_x = 0$, and then propagates towards deeper water. The turning point occurs at such depth H_t that $k_y = \omega/c_n(\omega, H_t)$. When $|k_y| < \omega/c_b$ in the penetrable wedge, the mode reaches its cutoff, where the mode's energy is radiated into the bottom, before it reaches a turning point, and the horizontal ray terminates. Geometry of horizontal rays emanating from a sound source at (x_s, 0, z) in the ideal wedge is described by the equation (Harrison, 1979)

$$x^2 - x_s^2 = 2x_s y\cot\psi + \frac{y^2}{\cos^2\gamma_n}\left(\sin^2\gamma_n + \cot^2\psi\right), \quad \gamma_n = \arcsin\frac{f}{F_n(x_s)}. \qquad (4.7)$$

Here $F_n(x_s)$ and ψ are the cutoff frequency and the angle between the ray and x coordinate axis at the source location. For a detailed discussion of geometry of horizontal rays and their caustic, see (Harrison, 1979).

On a horizontal ray, increments of the mode travel time and cross-slope displacement are $dT_n = \omega\left(k_x c_n u_n\right)^{-1} dx,\ dy = k_y dx/k_x$. Using Eq. (4.3) for the group speed and integrating by parts, we find

$$T_n = H\sqrt{c_n^{-2} - \omega^{-2}k_y^2}\Big|_{x_s}^{x} \cot\alpha + k_y y/\omega \qquad (4.8)$$

on a horizontal ray without turning points.[10] If the ray turns before reaching the receiver, mode travel time is calculated by using Eq. **Error! Reference source not found.** to find travel times to and from the turning point. In the ideal wedge, $k_y = \omega c^{-1}\sin\psi\cos\gamma_n$ in Eq.

Error! Reference source not found. is found analytically for any source and receiver positions by solving the quadratic equation **Error! Reference source not found.** for cotψ. In the penetrable wedge, k_y needs to be found numerically for a given $y \neq 0$.

In application to shallow-water acoustic waveguides, time-warping transform allows one to separate contributions of individual normal modes into acoustic field and retrieve modal dispersion curves without using hydrophone arrays.[2–8] "Warped time," t_w, and signal frequency in the warped domain, f_w, are given by the equations[1–3]

$$t_w = \sqrt{t^2 - t_r^2}, \quad f_w = f\left(t\right)\sqrt{1 - t_r^2/t^2}\,. \qquad (1)$$

It is assumed that signal is emitted at $t = 0$. Here t_r and $f(t)$ are a reference travel time and the instantaneous frequency of the signal arriving at the receiver at time t. In a range-independent waveguide with a uniform water column, reference travel time $t_r = r/c$, where r is range, i.e., source-receiver horizontal separation. If the dispersion curve of a normal mode is found in the physical domain, Eq. (1) maps the dispersion curve into the warped domain, and vice versa. For instance, according to Eq. **Error! Reference source not found.**, application of the transform (1) to range-independent waveguides with ideal boundaries gives $f_w = F_n$ for all values of t_w, $0 < t_w < \infty$, where F_n is the cut-off frequency of the normal mode. Hence, the dispersion curves of all normal modes are straight lines $f_w = F_n$ in the warped domain.

In application of the warping transform to sound propagation in a coastal wedge, we will also use $t_r = r/c$. In the ideal wedge this value coincides with the minimal mode travel time, see Eqs. **Error! Reference source not found.** and **Error! Reference source not found.**. Figure 1 illustrates the dependence of mode travel time on the mode order and frequency at upslope and

downslope propagation in a wedge, as predicted by Eqs. **Error! Reference source not found.** and (1). In this case, the problem is essentially two-dimensional (2-D). Note that wave frequency and warped frequency scale with depth as c/H. When the ratio of source and receiver depths is fixed, mode travel times and warped travel times scale as $\cot\alpha$; other than that, the graphs shown in Fig. 1 are unaffected by the bottom slope. The example presented in Fig. 1 refers to strong range dependence, where water depths at the source and receiver points differ by the factor of 2.

In the ideal wedge, travel time of reflected mode increases with increasing frequency, which is qualitatively different from the range-independent waveguide. Dispersion curves of the direct mode arrivals also systematically deviate from those in a range-independent waveguide with the same average depth but in a more subtle way (Figs. 1a, b). The warped frequencies of individual normal modes are no

longer constant and steadily increase with the warped travel time. The warped frequencies are higher than in a range-independent waveguide with the same average depth.

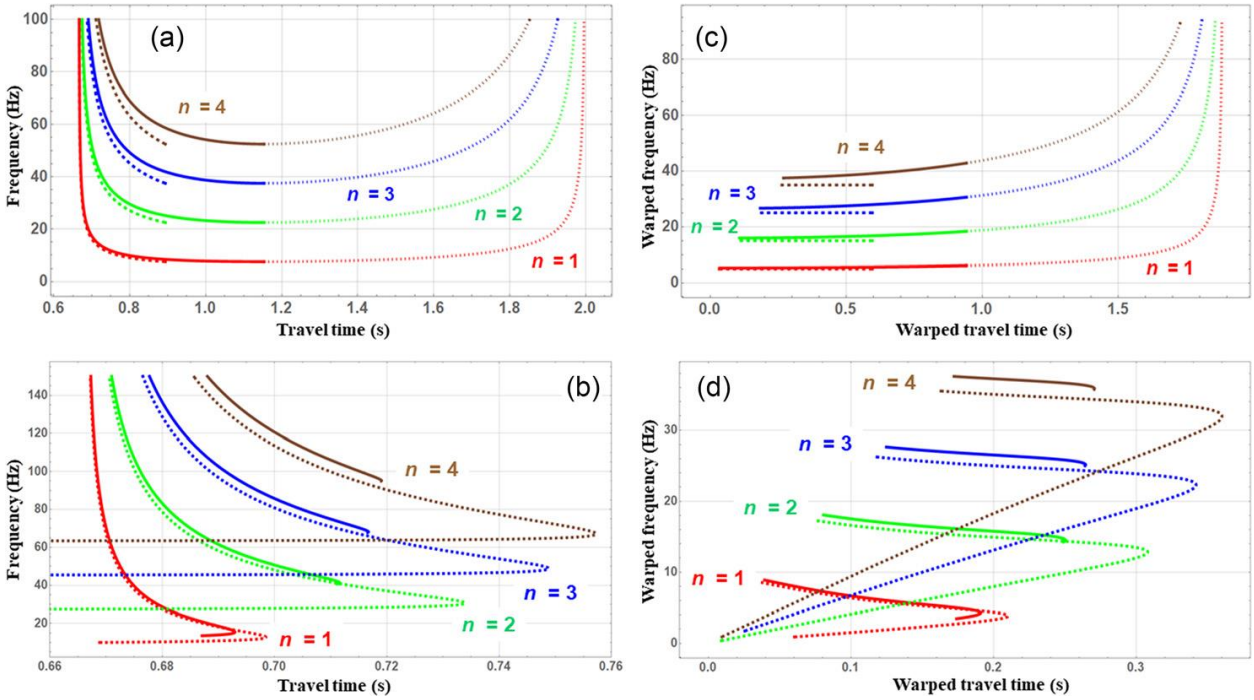

Fig. 4.1. Dispersion curves of the first four adiabatic normal modes in the physical (a, c) and warped (b, d) domains at upslope or downslope propagation in a coastal wedge. Source and receiver are located on a line perpendicular to the coast, with the water depths being 100 m and 50 m at the two locations. Sound speed in water is 1500 m/s, seafloor slope is 0.05 rad ≈ 2.86°. Sound is radiated in the 10–150 Hz frequency band. Mode order n is indicated in the figures. (a, c) Mode travel times in an ideal wedge with rigid bottom are shown for direct up- or downslope propagation between the source and receiver (solid lines) and for modes propagating downslope after reflection from their respective mode cut-offs at shallower depths (dotted lines). Mode travel times over the same range of 999.2 m in a range-independent waveguide with the same average depth of 75 m are shown by dashed lines. (b, d) Mode travel times in a penetrable wedge with a fluid bottom are shown by solid lines for up- or downslope propagation between the source and receiver. Dashed lines show mode travel times in a range-independent Pekeris waveguide with the same propagation range and average depth. Sound speed in the fluid bottom c_b =1800 m/s, the ratio of bottom and water densities m = 2.2.

In the adiabatic approximation, a normal mode propagating upslope radiates all its energy into the bottom in the vicinity of the mode's cutoff in the penetrable wedge. In contrast to the ideal wedge, there is no reflection from the cutoff. As a function of frequency, mode group speed u_n in the range-independent Pekeris waveguide has a minimum,[9] which separates the lower-frequency "ground wave," where u_n decreases with increasing frequency from $u_n = c_b$ at cutoff frequency to the minimum (anomalous dispersion), and the higher-frequency "water wave," where $\partial u_n/\partial\omega > 0$ (normal dispersion) (Fig. 4.1c). The most apparent difference between the dispersion curves in the penetrable wedge and in a range-independent waveguide with the same average depth is the disappearance (for modes n = 2, 3, 4) or contraction (for mode 1) of the anomalous dispersion part of the curves (Figs. 4.1c, d). In addition, at normal dispersion, instantaneous frequencies tend to be higher, at a given travel time, in the wedge than in the Pekeris waveguide. Another important difference from the range-independent case is the decrease in the maximum travel time (Figs. 1c, d). This can be attributed to the minimum group speed occurring at different frequencies at different depths, so that at all frequencies only a small portion of the entire up- or downslope propagation path is travelled at near-minimum group speeds. In the warped domain, contraction of the frequency range or complete disappearance of

the anomalous dispersion part gives the warping results in the penetrable wedge (Fig. 4.1d) a much closer resemblance of the results in the range-independent ideal waveguide than in the case of the Pekeris waveguide.

Seafloor slope has a significant effect on mode dispersion in a penetrable wedge even when the water depths at the source and receiver locations are the same. In this case of cross-slope propagation the effect is due to horizontal refraction. (Harrison, 1979). Figure 4.2 illustrates the effects of horizontal refraction at cross-slope propagation in a coastal wedge with a moderate seafloor slope of 2.86°. Adiabatic mode dispersion curves are given by Eqs. (4.8) and (4.9) in the physical and warped domains. In the ideal wedge, the instantaneous frequency of modal arrivals increases with mode order (Fig. 4.2a), as it does in range-independent waveguide. Dependence of the instantaneous frequency on travel time is opposite for the signals that traveled along horizontal rays with and without contact with the caustic. In contrast to the range-independent waveguide, the travel time increases with frequency on the modal eigenrays, which touch the caustic. This is similar to the situation with reflected arrivals at downslope propagation (Fig. 4.1a, b) and can be understood as the result of lengthening of the propagation path. The path length increases with increasing frequency since modes travel closer to shore at higher frequencies.

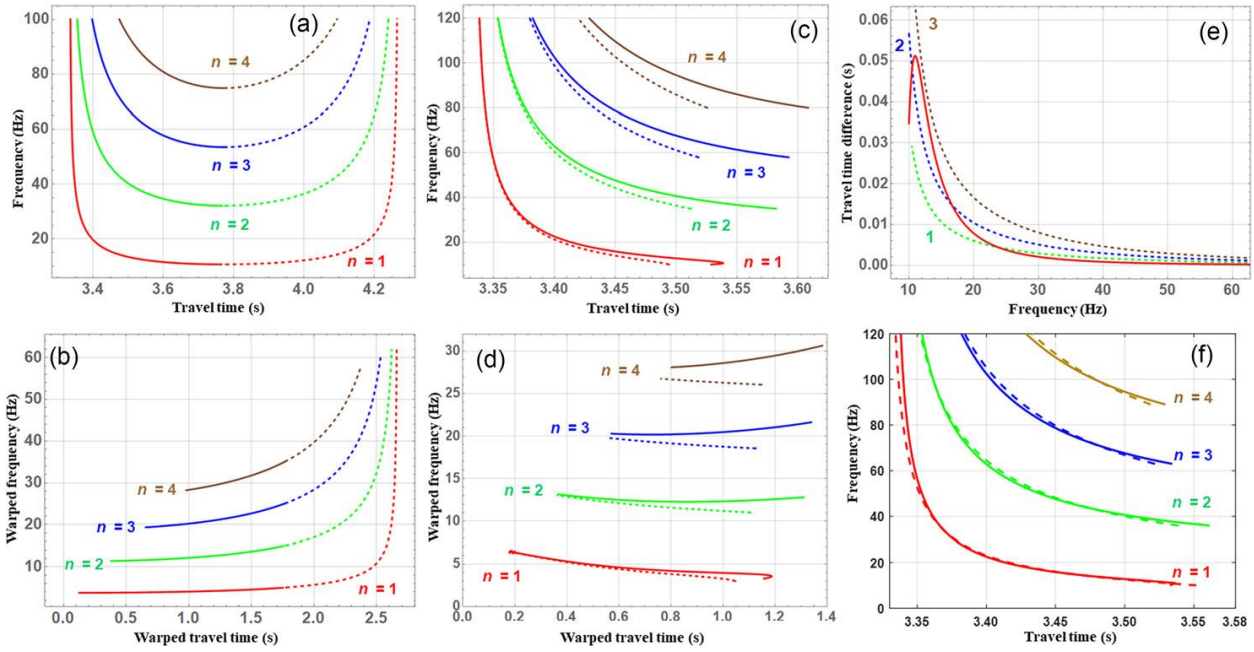

Fig. 4.2. Dispersion curves of adiabatic normal modes at cross-slope propagation in a coastal wedge. Water depth at the source and receiver locations is 100 m, source-receiver horizontal separation is 5000 m. Wedge geometry and waveguide parameters are the same as in Fig. 4.1. (a) Instantaneous frequency of modal arrivals is shown as a function of travel time and mode order n in a wedge with rigid bottom. Solid and dashed lines refer to the horizontal eigenrays before and after these reached a caustic. (b) Same as in (a) but for warped frequency as a function of warped time. (c) Instantaneous frequency of modal arrivals is shown as a function of travel time and mode order n in a penetrable wedge with a fluid bottom (solid lines) and in a range-independent Pekeris waveguide with the same propagation range and 100 m water depth (dashed lines). The dispersion curves are plotted in the frequency bands 10–120, 35–120, 58–120, and 80–120 Hz for modes 1, 2, 3, and 4, respectively. (d) Same as (c) but in the warped domain. (e) The travel time changes due to horizontal refraction and variations of the bottom sound speed are compared for mode 1. Solid line depicts the frequency dependence of the difference in travel times in the penetrable wedge and in the Pekeris waveguide with the same bottom parameters. Dashed curves show the difference in the mode travel time in the range-independent waveguide due to an increase in the bottom sound speed by 100 m/s (1), 200 m/s (2), and 400 m/s (3). (f) Mode travel times in the best-matching Pekeris waveguide (dashed lines) are superimposed on the dispersion curves of the four lowest-order adiabatic normal modes at cross-slope propagation in the penetrable wedge (solid lines). Bottom sound speed is 2270 m/s in the best-matching Pekeris waveguide; its other parameters are given in the text.

Dispersion curves of adiabatic normal modes prove to be self-similar in the ideal wedge. When the warped frequency is normalized by the mode cutoff frequency at the source, F_n, the plots of $f_w(t_w)/F_n$ collapse on the same curve for all n. This is also valid for $f(t)/F_n$ and in arbitrary (not just cross-slope) propagation geometry. The self-similarity follows from the fact that the travel time and horizontal ray geometry depend on ω and n via the single parameter, $\gamma_n = \arcsin\left(F_n / f\right)$, in Eqs. (4.7) and (4.8).

At cross-range propagation in a penetrable wedge normal modes experience stronger dispersion than at propagation over the same range in the range-independent waveguide with the same fluid bottom (Figs. 4.2c, d). This leads to an increase of the received signal duration. In particular, for a fixed frequency range in the normal dispersion band, the maximum travel time is

greatly increased compared to the Pekeris waveguide. Lower frequencies are responsible for later arrivals and are more sensitive to the seafloor slope (Fig. 4.2c). In contrast, travel times at higher frequencies, where the value of the group speed approaches the sound speed in water, are insensitive to the slope. Figure 2c indicates that the minimum effective group speed occurs (i.e., the adiabatic mode travel time reaches its maximum as a function of frequency) at a higher frequency at cross-slope propagation than in the Pekeris waveguide. At all frequencies considered, sound propagates slower in the wedge than in the Pekeris waveguide. This should be contrasted with the *decrease* in mode phase Φ_n due to horizontal refraction. Mode phase (eikonal) is given by the integral of the mode wavenumber ω/c_n along the horizontal ray (Godin, 2002) Of course, the signs of the phase and travel time changes being different would be impossible in the case of non-dispersive propagation. In the warped domain, horizontal refraction manifests itself in increasing modal travel time and values of the warped frequency (Fig. 4.2d). There is also a qualitative change in the dispersion curves of modes 2–4. Unlike the Pekeris waveguide and the case of upslope/downslope propagation (Fig. 4.1d), warped frequency increases with increasing warped time (Fig.4. 2d). As a result, the dispersion curves in the warped domain start to resemble the dispersion curves in the ideal waveguide rather than in the Pekeris waveguide.

The increase in the mode dispersion and maximum modal travel time due to horizontal refraction has significant implications for geoacoustic inversions, which are usually carried out either in the $N\times2D$ approximation or assuming range-independent environment. (Bonnel et al, 2011, 2013, Petrov, 2014, Godin, 2002). The travel times increase by up to 45–85 ms for modes 1–4 in Fig. 4.2c, and a large change in the bottom parameters is needed to reproduce the increase in the $N\times2D$ approximation. This is illustrated in Fig. 4.2e for mode 1, which is least affected by the horizontal refraction. In this example, c_b = 1800 m/s in the penetrable wedge but one needs bottom sound speeds between 1900 and 2200 m/s to approximate the long travel times at low frequencies.

A geoacoustic inversion has been carried out in the $N\times2D$ approximation using synthetic dispersion curves $T_n(f)$ of adiabatic modes (Fig. 4.2c) at cross-slope propagation in a penetrable wedge as the input data. No noise of any kind was added to the data. The inversion aimed to match the "measured," $T_n(f)$, and modeled, $t_n(f)$, dispersion curves of the first four modes at frequencies up to 120 Hz. The distance between the dispersion curves was quantified as $[T_n(f)]$–

$t_n(f)]^2$ and was averaged over frequency. At cross-slope propagation, the environment is a range-independent Pekeris waveguide in the $N\times2D$ approximation. There were four unknowns in the inverse problem: source-receiver horizontal separation r, water depth H, bottom sound speed c_b, and the ratio m of the bottom and water densities. An exhaustive search was performed on a regular grid with steps δr = 1 m, δH = 1 m, δc_b = 10 m/s, and δm = 0.1 in the following bounds: 4990 m $\leq r \leq$ 5010 m, 90 m $\leq H \leq$ 110 m, 1750 m/s $\leq c_b \leq$ 2300 m/s, and 1.2 $\leq m \leq$ 2.4. The best-matching model has r = 4996 m, H = 97 m, c_b = 2270 m/s, and m = 1.5 and is compared to the input dispersion curves in Fig. 2f, where dispersion curves are shown for each mode in the frequency band of the inversion scheme input. While the model succeeds in reducing the RMS travel time errors to acceptable values of 2.3 ms, 4.0 ms, 5.6 ms and 5.1 ms for modes 1, 2, 3, and 4, respectively, it comes at the cost of significant distortions in the water depth and bottom density and a severe, 470 m/s, overestimation of the bottom sound speed. Results of the inversion prove to be very sensitive to the amount of input information but the same trend remains. For instance, matching the dispersion curves of mode 1 alone or modes 1–3 gives H = 94 m, c_b = 2240 m/s, and m = 2.0 or H = 110 m, c_b = 2060 m/s, and m = 1.7, respectively.

Obviously, the same biases will occur in modal travel times-based geoacoustic inversions, whether time warping or another technique is used to isolate the normal-mode components of the acoustic field and measure the travel times. The bias depends on the acoustic observable(s) providing the input information, i.e., data, for an inversion. (Korakas and Sturm , 2011) used 3-D parabolic equation simulations to study the effect of horizontal refraction on geoacoustic inversions in a coastal wedge. Monochromatic acoustic pressure on a vertical line array spanning the water column served as synthetic input data. Unlike the data simulations, the inversions were done within the $N\times2D$ approximation. In a cross-slope propagation scenario rather similar to the one we considered above, results (Korakas and Sturm , 2011) were biased toward lower bottom sound speeds. This is in contrast to the strong bias towards higher bottom sound speeds that we found when mode travel times serve as the input data.

We have derived simple, closed-form equations for travel times of adiabatic normal modes in range-dependent waveguides, where the seabed impedance is independent of frequency. Horizontal inhomogeneity of the shallow-water waveguides is found to make the mode dispersion curves more similar to those of an ideal waveguide than in the absence of range-dependence, and to contribute to the success of separating the normal modes using time-warping.

Bathymetry variations suppress or eliminate the ground wave part of the mode dispersion curve. This may explain, in part, the known difficulty of retrieving the ground wave when the warping transform is used to isolate the normal modes in the coastal ocean. In agreement with Fermat's principle, the $N\times 2D$ approximation, which disregards horizontal refraction, systematically overestimates the phase of normal modes (Godin, 2002). However, the travel time bias introduced by the $N\times 2D$ approximation has the opposite sign in the coastal wedge.

In geoacoustic inversions of mode travel times, moderate bottom slopes are shown to lead to significant errors in retrieved seabed parameters and cause a positive bias up to hundreds of m/s in the inferred bottom sound speed, if horizontal refraction is ignored.

4.2. Passive geocoustic inversion in a dynamic environment on a continental shelf

Empirical Green's functions are obtained for 31 paths in a highly dynamic coastal ocean by cross-correlation of ambient and shipping noise recorded in the Shallow Water 2006 experiment on a horizontal line array and a single hydrophone about 3600 m from the array. Using time warping, group speeds of three low-order normal modes are passively measured in the 10–110 Hz frequency band and inverted for geoacoustic parameters of the seabed. It is demonstrated that, despite very strong sound speed variations caused by nonlinear internal waves, noise interferometry can be successfully used to acoustically characterize the seafloor on a continental shelf.

Acoustic noise interferometry (Roux et al, 2004, Sabra et al, 2005, Godin, 2006) exploits ambient and shipping noise as a signal to probe the ocean and offers a way to measure its physical parameters without using any controlled sound sources (Godin et al, 2010, 2014, Woolfe, 2015). The technique relies on time averaging to retrieve an approximation to the deterministic Green's function (GF), or empirical GF, from noise cross-correlations. In shallow water, the basic assumption that the environment does not change during noise averaging time is hardly compatible with temporal variability of the ocean. Theory (Skarsoulis et al, 2019) and experiments in coastal oceans with mild temporal variability indicate that the assumption can be significantly relaxed. The goal of this paper is to investigate the feasibility of using noise interferometry for passive acoustic characterization of the seabed in a coastal ocean with strong and rapid variations of the water column properties. We obtain empirical GFs from noise cross-

correlations on multiple paths in a highly dynamic environment (Sabra et al, 2005, Godin, 2018) on the US continental shelf, apply time-warping transform to retrieve dispersion curves of normal modes from the GFs, invert the passively measured dispersion curves to estimate parameters of the seabed, and compare results of the passive and active geoacoustic inversions.

The data employed in this study are the records of shipping and ambient noise obtained in the course of the Shallow Water 2006 (SW06) experiment (Sabra, 2005) on the US continental shelf off New Jersey. We use time series of noise continuously recorded during 15 days from August 18 to September 1, 2006 on a Single Hydrophone Recording Unit (SHRU) and 32-hydrophone horizontal line array (HLA).

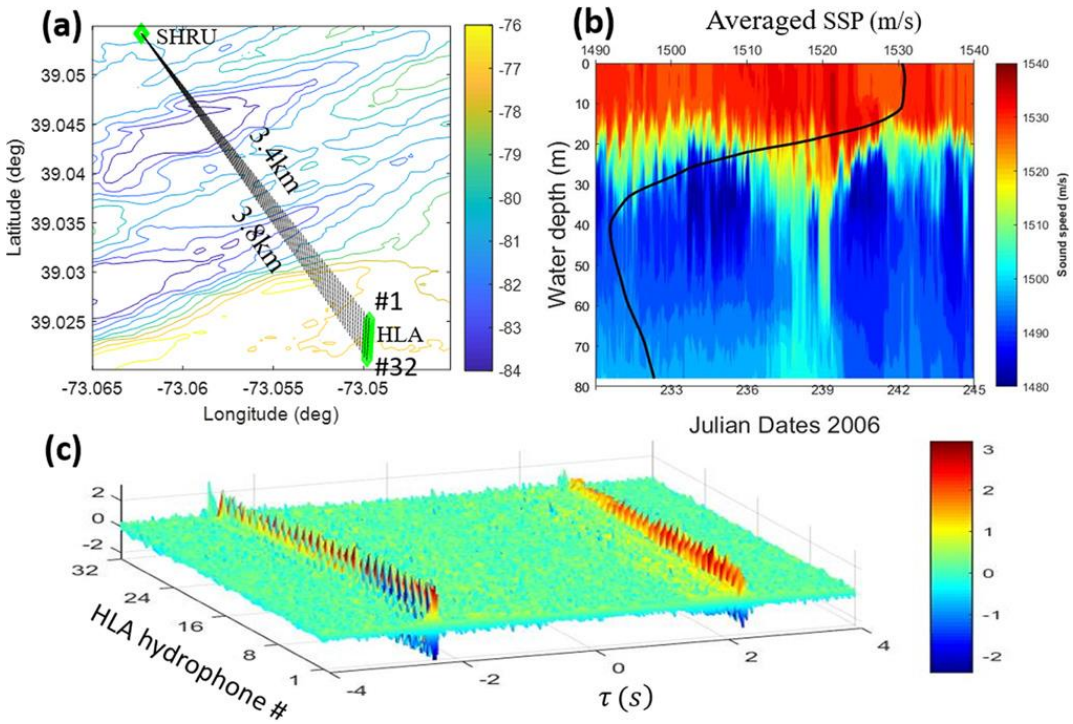

Fig. 4.3. (Color online) Bathymetry, sound speed, and two-point cross-correlation functions of noise measured during the SW06 experiment. (a) Locations of the SHRU and horizontal line array (HLA) employed in this study. Water depth (in meters) is shown by color of the isobaths. (b) Time-dependence of the sound speed in water (shown by color) measured at a location near the northern end of the HLA, with the fifteen-day average of the sound speed profile (black line) superimposed. (c) Noise cross-correlation functions (NCCFs) between SHRU and individual hydrophones of HLA are shown as functions of the time delay τ and the number, 1 to 32, of the

HLA hydrophone. Color indicates NCCF value (in arbitrary units). NCCFs are calculated using 15 days of noise records.

The spacing of HLA hydrophones is 15 m, and the distance between SHRU and the HLA hydrophones ranges between 3.4 and 3.8 km [Fig. 4.3(a)]. SHRU and HLA hydrophones are located close to the seafloor. The two systems share the same sampling frequency and data format, (Sabra, 2005) which facilitates data processing.

The SW06 site is known for strong and rapid variations of the sound speed in the water column due to energetic internal gravity waves, including internal tides (Godin, 2018) Figure 4.3(b) shows sound speed measured with a vertical thermistor chain (Sabra et al, 2005) that was deployed in the vicinity of the southern end of HLA. Internal tides depress the thermocline by tens of meters in a quasi-periodic manner causing sound speed variations up to 10 m/s from the mean [Fig. 4.3(b)] and making the environment rather challenging for application of acoustic noise interferometry.

We have calculated cross-correlation functions between the acoustic pressure recorded at SHRU and each of the HLA hydrophones [Fig. 4.3(c)]. Following Refs. (Godin et al, 2014) and (Bonnel et al, 2011), NCCF between SHRU and *i*-th hydrophone of HLA is first evaluated in the frequency domain as an average over *N* non-overlapping time windows:

$$\hat{C}_i(f) = \frac{1}{N}\sum_{n=1}^{N} \frac{P_S^{(n)}(f) P_{H,i}^{(n)}(f)^*}{\left| P_S^{(n)}(f) P_{H,i}^{(n)}(f)^* \right|}, \quad i = 1, 2, \ldots, 32. \tag{4.10}$$

Here the asterisk * denotes complex conjugation; $P_S^{(n)}(f)$ and $P_{H,i}^{(n)}(f)$ are the spectra of pressure recorded during the *n*-th time window by SHRU and *i*-th HLA hydrophone, respectively. Normalizing the spectra by their absolute values in the summand in Eq. (4.10) implements the spectral pre-whitening that, in the noise interferometry context, is known to suppress contributions of strong, transient non-diffuse noise sources such as nearby shipping (Godin et al, 2005) The time domain NCCFs $C_i(\tau)$ are obtained via inverse Fourier transform of Eq. (4.10) . For brevity, the negative ($\tau < 0$) and positive ($\tau > 0$) time-delay parts of $C_i(\tau)$ will be

referred to as N-NCCF and P-NCCF. These approximate, respectively, the acoustic GFs that describe sound propagation from the *i*-th HLA hydrophone to SHRU and from SHRU to the hydrophone.

Time-window length of 64 s was chosen in implementing Eq. (4.10). HLA hydrophone #31 malfunctioned during the experiment and did not produce useful data. Thus, NCCFs were obtained only for 31 receiver pairs. In motionless media with perfectly diffuse noise, NCCFs are even function of τ, (Godin, 2006) and asymmetry of measured NCCFs is due to a shift between the internal clocks used at the two receivers. Cross-correlation of P-NCCF with N-NCCF for the same receiver pair, which was done for all 31 pairs, revealed a shift of 0.896 s between the SHRU and HLA clocks. Being much smaller than the time-window length, the clock shift has a negligible effect on the quality of NCCF estimates and has been corrected for by shifting all $C_i(\tau)$ by 0.896 s along the time-delay axis.

With random noise sources, the sum in the right side of Eq. (4.10) is also a random function. In a time-independent environment, it is expected to converge to a deterministic NCCF when noise averaging time is sufficiently long, i.e., the number N of time windows is sufficiently large. The frequency band 10 Hz < f < 110 Hz is used to obtain the time-domain NCCFs. The deterministic features of the NCCFs gradually emerge and become increasingly clear as more daily averages are stacked. About 10 days of noise averaging is sufficient to reach a stable estimate of all NCCFs. Since noise sources are intermittent, the signal strengths of both P-NCCFs and N-NCCFs do not increase monotonically. [In noise interferometry, the deterministic component of NCCF estimates serves as the signal, and signal-to-noise ratio (SNR) is understood as the ratio of amplitudes of the deterministic and random components of an NCCF estimate.] It is interesting to observe that P-NCCFs accumulate faster than N-NCCFs in the first five days, and after that both approach stability in a qualitatively similar way. We found that certain days, such as days 6 and 12, produce N-NCCF estimates with a particularly high SNR. Averaging noise recorded during 2–3 of such "good days" results in N-NCCF estimates with SNR close to that of the much longer, fifteen-day averages shown in Fig. 4.3(c).

Note that SNR decreases as the horizontal distance from SHRU to the HLA hydrophone increases. The decrease appears to be faster than that of the GF amplitude. This can be due, in part, to the noise directivity in the horizontal plane. Variations of the sound speed profile and sea

surface geometry in time also contribute to the more rapid decrease of the NCCF's SNR with range than in the time-independent environment. Moreover, the suppression of the coherent (deterministic) component of NCCF estimates due to time dependence of the propagation conditions tends to increase with acoustic frequency. For individual normal mode components of NCCF in shallow-water waveguide, the suppression is also predicted to increase with the mode order. We found that SNR of the Eq. (4.10) -based NCCF estimate becomes rather low and the signal is lost in noise at frequencies above about 110 Hz. No useful NCCFs were derived from the available data at these frequencies. We attribute this to the coherence loss of time averages in the rapidly evolving environment. The subsequent analysis will be limited to 10–110 Hz frequency band.

Remark, that there are additional NCCF peaks that appear at positive time delays τ shortly before the main peaks of P-NCCFs. The additional peaks form a line in Fig. 4.3(c). We interpret the additional peak as a spurious arrival from a non-diffuse noise source. Position of the additional peaks is found to be consistent with the non-diffuse noise source being a shipping lanes leading to and from the New York Harbor, which is located about 120 nm from HLA. Same interpretation was proposed earlier for the spurious arrival observed in NCCF for a different pair of SW06 receivers. The spurious arrivals partially overlap with the main peaks and distort the P-NCCFs, especially on the northern side of HLA [Fig. 4.3(a)]. Because of this, only N-NCCFs are used in this study as the input data to retrieve normal mode dispersion curves and perform geoacoustic inversions.

Time warping transform maps a signal $S(\tau)$ into the "warped" signal

$$S\left(w(\tau)\right) = \left|dw(\tau)/d\tau\right|^{-1/2} S(\tau), \tag{4.11}$$

where $w(\tau)$ has the meaning of time in the warped domain. Transform (4.11) with the warping function $w(\tau) = \left(\tau^2 - \tau_r^{\,2}\right)^{1/2}$ has been used successfully to isolate normal mode components of acoustic field in shallow-water waveguides. Here $\tau = 0$ at the moment when the signal is emitted by a sound source. Reference time τ_r in the warping function can be defined as $\tau_r = r/c_w$, where r is the sound propagation range and c_w is a representative value of sound speed in water. In the noise interferometry context, r is the distance between two receivers. The inverse time-warping

transform, which restores the original signal from the warped one, is again given by Eq. (4.11) but with $w(\tau) = \left(\tau^2 + \tau_r^{\,2}\right)^{1/2}$.

We use measured N-NCCFs as the signals to probe the environment. Then $S_i(\tau) = C_i(-\tau)$, $\tau > 0$, $i = 1, 2, \ldots, 32$. Spectrogram of $S_1(\tau)$ is shown in Fig 4.4(a). The spectrogram shows strong mode interference that manifests itself most clearly in a sequence of deep interference nulls. It does not appear possible to identify individual mode contributions, let alone retrieve mode dispersion curves from the spectrogram. However, normal mode components occupy distinct frequency bands and are clearly separated in the spectrogram of the warped signal $S_1(w)$ in Fig.4.4 (b). In the warping function $w(\tau)$, τ_r has the meaning of the earliest arrival time of the received signal being warped. For each receiver pair, it has been determined from the condition that modes are best separated and fully resolved in the warped domain. For instance, the optimum reference time for $S_1(w)$ is $\tau_r \approx 2.28$ s. Equivalent values of c_w in the equation $\tau_r = r/c_w$ for the optimum reference times prove to be close to the minimum of the sound speed profile in Fig. 4.3(b).

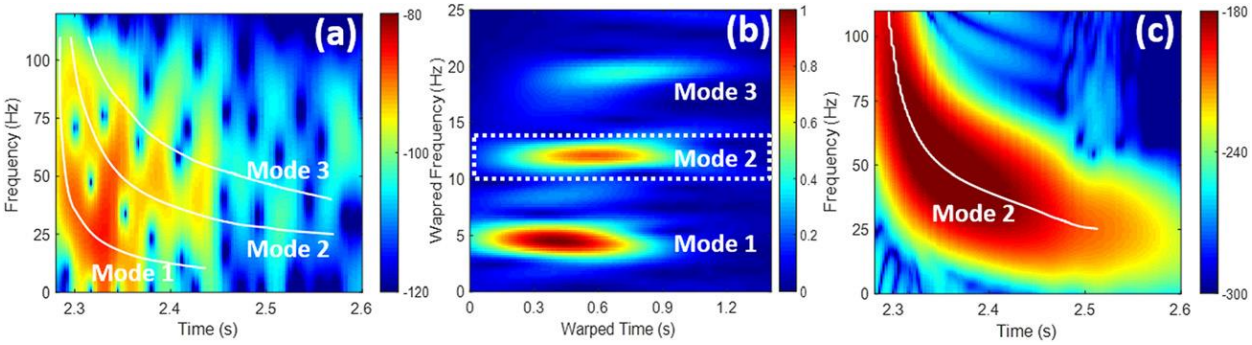

Fig.4.4. Application of the time-warping transform to a measured NCCF to separate its normal-modal components and passively measure dispersion curves of the normal modes. (a) Spectrogram of the negative-time-delay part, N-NCCF, of the cross-correlation $C_1(\tau)$ between SHRU and the first HLA hydrophone. Spectral density is shown by color in dB relative an arbitrary reference. Overlaid white lines display estimated dispersion curves of the first three normal modes. (b) Spectrogram of the same N-NCCF after time warping. Contributions of individual normal modes are indicated. The area within white dashed lines is the time-frequency

mask applied to isolate mode 2 as an unwarping stage of signal processing. (c) Spectrogram of the mode 2 waveform after unwarping. White line shows the mode 2 dispersion curve retrieved from the spectrogram.

The spectrogram of the warped signal allows one to define time-frequency (TF) masks as areas in the warped time-warped frequency plane, where energy of a single mode is concentrated and no other modes are present. TF mask of a particular mode is illustrated in Fig. 4.4(b). To isolate the contribution of mode m to the signal $S_i(\tau)$, respective TF mask is applied to the short-time Fourier transform of $S_i(w)$. Inverse short-time Fourier transform of the result gives the mode's waveform in the warped domain, which is unwarped back to the physical domain by application of the inverse time-warping transform. Spectrogram of the mode 2 component of $S_1(\tau)$ is illustrated in Fig. 4.4(c). As expected, it shows no signs of mode interference.

In a spectrogram of a single-mode, broadband waveform the peak values with respect to time at any given frequency lie close to the travel time, which corresponds to the mode's group speed at that frequency. Dependence of the travel time on frequency is most accurately extracted from the spectrogram using the reassignment process, (Tan et al, 2019) which improves the resolution of TF distribution by reallocating the energy concentration. The result of application of the reassignment process is illustrated in Fig. 4.4(c) for mode 2 component of signal $S_1(\tau)$. The procedure was repeated and frequency dependence of the travel time was determined for the first 3 modes using optimum, mode- and HLA hydrophone-specific TF masks for all 31 measured N-NCCFs.

Geoacoustic inversion

The input acoustic data for a geoacoustic inversion (Fig. 4.5) are the travel times of modes m = 1–3 measured on 31 paths. Assuming range-independent propagation, for each mode the data can be combined in terms of the group speed $g_{i,m}(f) = r_i / t_{i,m}(f)$ of the mode. Here r_i is the horizontal distance between SHRU and i-th HLA hydrophone. Averaging $g_{i,m}$ over i has the advantage of significantly suppressing random measurement errors. The frequency dependence of the path-averaged group speeds $\bar{g}_m(f)$ and uncertainty of their measurements are illustrated

in Fig. 4.5(b). The uncertainty is evaluated at each frequency as the square root of the sample variance of 31 measurements.

The actual propagation environment is horizontally inhomogeneous. The water depths at SHRU and HLA are 82 m and 78 m, respectively. Within the triangle with vertices at SHRU and hydrophones 1 and 32 of HLA [Fig. 4.3(a)], water depths are 76–85 m with the average of 80.6 m. We modeled the effect of bathymetry on the mode travel times in the Nx2D approximation assuming adiabatic propagation.[17] Water column and seabed parameters in the simulations were taken from the optimal environmental model [see Fig. 4.5(a) and Table 1] discussed later in this Section. We found that the differences between travel times over actual, range-dependent bathymetry on a path and in the range-independent waveguide with the path-average water depth to be small compared to the measurement errors on a single path. For instance, for $m = 2$ and on a typical path $i = 16$ at frequency of 50 Hz, range dependence of the bathymetry changes the mode travel time by about 30% of the measurement uncertainty shown in Fig. 4.5(b). The largest effects of the range-dependence were found for mode 3, for which measurement uncertainties are also larger. In the simulations, effects of changes in the path-averaged depth were found to be significantly stronger than those of variations from the average. We conclude that, with the data available, the advantages of measurement error suppression by path averaging far outweigh any possible benefits of including a range-dependent bathymetry in geoacoustic inversions.

We conduct a geoacoustic inversion assuming a range-independent environmental model with a fluid seabed formed by a homogeneous sediment layer overlying a homogeneous half-space, and a known sound speed profile in water [Fig. 3(a)]. Sound speed in water is given by the time-averaged profile shown in Fig. 1(b). The unknown parameters of the model are the water depth D, sediment layer thickness H, sound speeds c_s, c_b in the sediment and basement, and the ratios ρ_s, ρ_b of densities in the sediment and half-space to that in seawater.

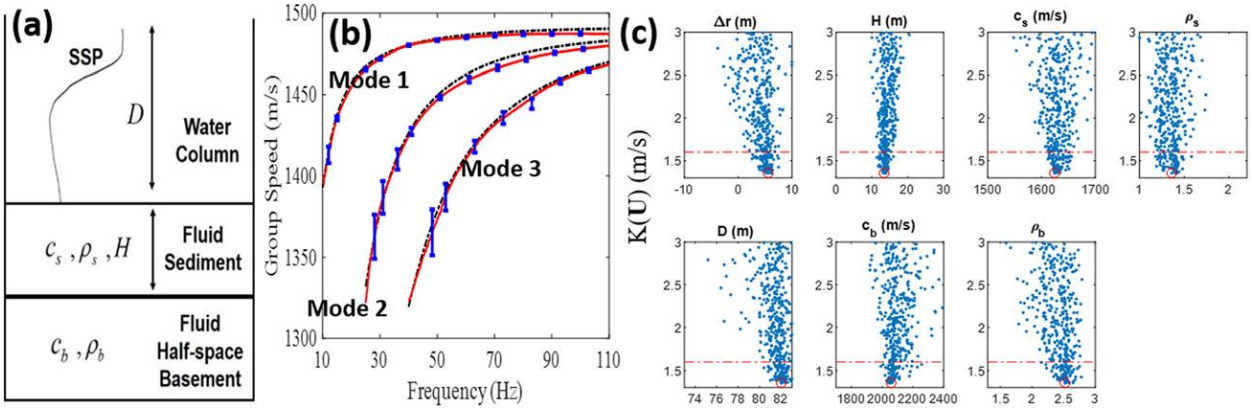

Fig. 4.5. Geoacoustic inversion. (a) Range-independent environmental model implied in the inversion process. The unknown parameters to be determined are the water depth D, sediment layer thickness H, sound speeds c_s, c_b in the sediment and basement, and the ratios ρ_s, ρ_b of densities in the sediment and basement to that in seawater. Sound speed profile in water is assumed to be known. (b) Normal mode dispersion curves. Red solid lines are the passively measured frequency dependencies of the mode group speeds, with error bars shown in blue for selected frequency bins. Black dashed lines are the dispersion curves in the best-fitting environment found by solving the inverse problem. (c) Sensitivity of the data-model mismatch to individual parameters of the environmental model. In each panel, the cost function $K(\mathbf{U})$, Eq. (4.3), is plotted as a function of a single search parameter for all possible values of the other five parameters. Red circle indicates the position of the cost function minimum $K(\hat{\mathbf{U}}) \approx 2.32$ m/s and the inferred value of each parameter. Only values of $K(\mathbf{U})$ up to 4 m/s are shown.

The unknown parameters are found by minimizing the mismatch

$$K(\mathbf{U}) = \sqrt{\frac{1}{N}\sum_{m,n=1}^{M,N}\left[\bar{g}_m(f_n) - \hat{g}_m(f_n,\mathbf{U})\right]^2} \qquad (4.12)$$

between the measured, $\bar{g}_m(f)$, and modeled group speeds of normal modes. Here $M = 3$ is the number of normal modes identified, and N is the number of frequency bins to be compared between the measured and modeled mode dispersion curves. The modeled group speeds $\hat{g}_m(f_n,\mathbf{U})$ are calculated by the normal mode code KRAKEN[18] for various values of the vector $\mathbf{U} = \{H, c_s, \rho_s, c_b, \rho_b, D\}$ of unknown environmental parameters.

The minimum $K\left(\hat{\mathbf{U}}\right) \approx 2.32$ m/s of the cost function $K\left(\mathbf{U}\right)$ in Eq. (4.12) is found by exhaustive search on a regular grid in the six-dimensional parameters space. Table 1 summarizes parameters of the grid and the optimal environmental model, which minimizes the data-model mismatch. The choice of search bounds for the geoacoustic parameters (Table 1) was informed by results of the previous geoacoustic studies[12, 19–21] at the SW06 site. Sensitivity of the cost function to variations of individual search parameters is illustrated in Fig. 4.5(c). As a function of water depth, the mismatch is minimal at D = 81 m, which is close to the average depth of 80.6 m. Sediment layer parameters, especially H and c_s, are well constrained with the mode dispersion data, while sensitivity to c_b and especially ρ_b is lower [Fig. 4.5(c)]. Figure 4.5(b) compares normal mode dispersion curves in the optimal environmental model with the measured group speeds. Note that the mismatch is small compared to measurement uncertainties, except at higher frequencies, where modal group speeds are most sensitive to variations of the sound speed in water. The inversion results are further discussed in the next section and compared to geoacoustic models derived in other studies.

Table 1. Geoacoustic inversion parameters and results

Parameter	Unit	Search bounds	Step	Inversion results
H	m	[5, 30]	2.5	15
c_s	m/s	[1500, 1700]	20	1620
ρ_s	–	[1.1, 1.9]	0.1	1.4
c_b	m/s	[1700, 2100]	25	2050
ρ_b	–	[1.3, 2.5]	0.15	2.35
D	m	[77, 83]	1	81

As demonstrated earlier, empirical GFs have been retrieved from NCCFs in the 10–110 Hz frequency band with accuracy sufficient to characterize geoacoustic properties of the seabed, despite very strong variations of the sound speed in water [Fig. 4.3(b)] during the noise averaging time. Application of noise interferometry to SW06 data was first reported at much

shorter ranges from tens to a few hundred meters[22, 23] and with shorter averaging times. No environmental information was retrieved from the short-range empirical GFs, which were obtained in the 20–100 Hz band. [22, 23] With 5.7-day noise averaging time, Qin et al.[15] calculated NCCF in the 10–70 Hz band for two SHRUs about 8 km apart and used the passive time-reversal mirror technique to carry out a single-parameter geoacoustic inversion assuming a homogeneous fluid seabed. From a subset of the data employed in the present study, Tan et al.[24] found empirical GFs in the 10–90 Hz frequency band from 7-day noise averages and performed a time-warping-based geoacoustic inversion using a single hydrophone pair. Compared to the previous work,[24] a longer averaging time and especially combining the results for 31 hydrophone pairs have allowed us here to expand the bandwidth and significantly increase the accuracy of retrieval of mode dispersion curves from the noise cross-correlations.

Within the chosen parameterization of the seabed properties [Fig. 4.5(a)], robustness of the geoacoustic inversion was investigated by employing a different cost function and varying the bandwidth of input data. If the cost function is chosen as the mismatch in the path-average of the group slowness, $1/g_{i,m}(f_n)$, rather than the mode group speed $g_{i,m}(f_n)$, solution of the inverse problem changes insignificantly: the inverted sediment properties H, c_s and ρ_s remain unchanged, and the basement properties shift by only one grid step.

Using mode group speed measurements at the lowest available frequencies was found critical to ensure sensitivity to the sediment layer and especially the half-space parameters. In contrast, decreasing the upper frequency from 110 Hz to 90 Hz appreciably changed only the optimum value of the water depth; ρ_b value changed by one grid step, and the other geoacoustic parameters were unaffected. This is consistent with results of the forward modeling, which shows that the group speeds at these frequencies are most sensitive to sound speed in water, and suggests the possibility of using the upper part of the available frequency band to characterize the water column properties.

Previous geoacoustic inversions at the SW06 site, which were performed using data obtained with various active techniques, gave a wide range of values of compressional wave speeds of 1560–1680 m/s in the upper sediment (up to few tens of meters below the seafloor) and 1650–2199 m/s in deeper layers (basement), see reviews in Refs. (Frisk et al, 2014, Wan et al 2016). Sediment and basement densities, either estimated or assumed in inversions, are 1.55–

2.30 g/cm^3 and 2.13–2.96 g/cm^3, respectively (Jiang et al, 2010, Wan et al, 2016). The range of geoacoustic parameters' estimates is very large because the geologic structure of the seabed changes rapidly with horizontal coordinates (Goff et al, 2004) and also because of differences in the acoustic frequencies, from 20 to 1000 Hz, and inversion approaches used. In terms of geographic proximity, geologic similarity (Goff et al, 2004, Wan et al 2016), and acoustic frequencies used, Refs. (Bonnel et al, 2011, Ballard et al, 2010) and Region 42 in Ref. (Rajan et al, 2010) are most closely related to the present study. Using a signal from an imploding lightbulb, Bonnel and Chapman, 2011 measured normal mode dispersion curves in a roughly 30–170 Hz band and found the following values of the geoacoustic parameters: c_s = 1603 m/s, c_b = 2199 m/s, H = 26.9 m, ρ_s = 1.89, ρ_b = 2.28. Our results (Table 1) for the basement parameters agree well with estimates in Ref. (Bonnel et al, 2011), certainly within the uncertainty of the estimates. Comparison of Fig. 4.5(c) with Fig. 4 in Ref. 12 indicates that the passive inversion is considerably more sensitive to c_b as well as H that was not reliably retrieved in Ref. (Bonnel et al, 2011), which can be attributed to our data containing lower acoustic frequencies. Results for c_s in Table 1 and Ref. (Bonnel et al, 2011) are reasonably close, although the higher sediment sound speed obtained in the present study agrees better with other results in the area, as discussed below. However, our estimate of ρ_s is significantly lower than in Ref. (Bonnel et al, 2011) . The sediment density in Table 1 is lower than expected and previously reported. A possible reason for ρ_s underestimation is that the inversion returns an effective density value, which incorporates, within the fluid bottom model, the low-frequency effects of shear rigidity of the sediments.

Comparison with results of Refs. (Rajan et al, 2010) and Ballard et al, 2010), which use data obtained with towed sources in 30–120 Hz and 50–175 Hz bands, respectively, refer to much wider areas, and report range-dependent inversions, is further complicated by the differences in the geoacoustic model parameterization. These results provide much higher vertical resolution of sound speed in the seabed but presuppose a fixed density stratification and, in Ref. (Ballard et al,2010), the depth of a strongly reflective interface (R-reflector) within the seabed. There is a similarity between gross features of sediment sound speed stratification in the geoacoustic models in Refs. 25, 27, and present study, see Fig. 16b in Ref. (Rajan et al, 2010). When averaged from the seafloor down, the average sound speed reaches c_s = 1620 m/s at about 11.0 m and 18.5 m in Refs. (Rajan et al, 2010) and , respectively. The value H = 15 m in Table 1 is close

to the average of these depths. However, the c_b values, 1725 m/s (Ballard et al, 2010) and 1765 m/s, (Rajan et al, 2010) are much smaller than in Table 1. The larger c_b values suggested by Bonnel and Chapman and the present study were apparently not explored in the perturbative inversions (Rajan et al, 2010, ballard et al, 2010) . Other possible reasons for the discrepancy include the effects of shear rigidity and horizontal refraction, which manifest differently on distinct paths and in different frequency bands and were not considered in any of the inversions. Very large c_b biases, up to hundreds of m/s, due to neglect of horizontal refraction were recently reported (Godin et al, 2019) for moderate slopes of a few degrees of the seafloor; the bias has opposite signs for tonal (Ballard et al, 2010) and broadband modal data.

We have demonstrated that robust estimates of empirical Green's functions can be obtained from noise cross-correlations in a dynamic coastal ocean despite internal wave-induced strong, rapid variations of the sound speed in water. Passively measured dispersion curves of low-order acoustic normal modes have been inverted for geoacoustic parameters of the seabed. The results are largely consistent with earlier geoacoustic inversions employing controlled sound sources in the same general area.

Future work includes using a higher-frequency portion of passively measured modal dispersion curves to characterize the water column variability and extending geoacoustic inversions to horizontally inhomogeneous environmental models.

V. OBSERVATIONS OF ACOUSTIC NOISE BURSTS ACCOMPANYING NONLINEAR INTERNAL GRAVITY WAVES ON A CONTINENTAL SHELF OFF NEW JERSEY

Anomalously large, transient fluctuations of acoustical noise intensity (up to four-five orders of magnitude above the background in a wide frequency band) were observed with single-hydrophone receiver units (SHRUs) and on the L-shaped horizontal and vertical line array of hydrophones (HVLA) "Shark" (belonging to Woods Hole Oceanographic Institution) in the Shallow Water 2006 experiment. The present study investigated temporal and spatial properties of these noise bursts. The site of the experiment (the New Jersey Atlantic shelf) is characterized by strong internal gravity wave activity, including tidally generated nonlinear internal waves (NIWs). As NIWs move from the shelf break towards the coast, they form trains consisting of up to twelve separate, localized, soliton-like waves with up to 25–35 m displacement of isopycnal surfaces. The NIW trains consecutively cross the positions of five SHRUs and the HVLA Shark that are located about 5–8 km from each other along a line perpendicular to the coast. We found that the bursts of acoustic noise were observed when an NIW train passed through locations of the corresponding acoustic receivers. Turbulence of the water flow, saltation and bedload of marine sediments were the dominant causes of the acoustic noise bursts caused by NIWs at different frequency bands. On near-bottom hydrophones, the most energetic part of the observed noise bursts was generated by collisions of suspended sediment particles with each other, the sensor, and the seafloor.

Internal gravity waves in the ocean create time-dependent and spatially inhomogeneous variations in temperature and sound speed profiles and are known to have a significant effect on underwater sound propagation (Simmen et al., 1997; Colosi et al., 1999; Tang et al., 2007). Especially strong variations in the sound propagation conditions and attendant fluctuations of the acoustic fields occur due to nonlinear internal waves (NIW) on continental shelves (Zhou et al., 1991; Godin et al., 2006; Apel et al., 2007). The magnitude of the acoustic effects depends on the NIW amplitude and spatial structure as well as on the azimuthal direction of the acoustical track relative to the direction of NIW propagation, which determines the dominant physical mechanism of the NIW-sound interaction. For example, on a 14 km propagation track largely along NIW wavefronts in the SWARM95 experiment in the Mid-Atlantic Bight, NIW-induced focusing and defocusing of acoustic normal modes in the horizontal plane was found to result in sound intensity fluctuations of low-frequency (20–300 Hz), with magnitudes of 7–8 dB and

periods of about 10 minutes (Badiey et al., 2002, 2007). In the same experiment, for mid-frequency signals (a few kHz) on a different sound propagation track crossing the NIW wavefronts, sound intensity fluctuations of a few dB took place due to NIW-induced coupling of the acoustic normal modes (Badiey et al., 2002; Katsnelson et al., 2009). Perhaps the strongest reported NIW-induced fluctuations of the transmission loss, or frequency-dependent sound intensity, of 20–25 dB were observed in the Yellow Sea off China; these were explained in terms of the resonant Bragg scattering of sound by an NIW wave train (Zhou et al., 1991; Apel et al., 2007).

In addition to the propagation effects, NIWs were observed to change sound intensity by generating underwater acoustic noise. Currents of various nature, including NIW-induced currents, shed vortices and generate turbulent pressure fluctuations when flowing past acoustic sensors and elements of their moorings. These pressure fluctuations are observed as very low-frequency noise (typically, below a few tens of Hertz) and are known as flow noise (Strasberg, 1979; Webb, 1988). Measurements of NIW-induced flow noise have been described in the literature (Serebryany et al., 2008b; Yang et al., 2013). At higher frequencies, Serebryany et al. (2005, 2008a, 2008b) observed strong fluctuations of the ocean surface-generated broadband acoustic noise that accompanied passage of a strong NIW. These fluctuations were attributed to the modulation of the surface gravity and capillary-gravity wave activity on the ocean surface by NIW-induced currents. NIW-induced fluctuations of the intensity of the surface-generated noise reached 10–15 dB in deep water in the Indian ocean (Serebryany et al., 2005) and up to about 6 dB on the continental shelf in the in the Mid-Atlantic Bight (Serebryany et al., 2008b). Similar observations were made by Yang et al. in the Pacific northeast of Taiwan (Yang et al., 2013) and in the South China Sea (Yang et al., 2015), with about 10 dB variations of the acoustic noise intensity due to NIW-induced changes in the surface wave activity.

In the present paper, we describe our analysis of observations of very large (up to 50 dB) broadband, transient increases in the noise intensity, to be referred to as noise bursts, on the continental shelf off New Jersey.

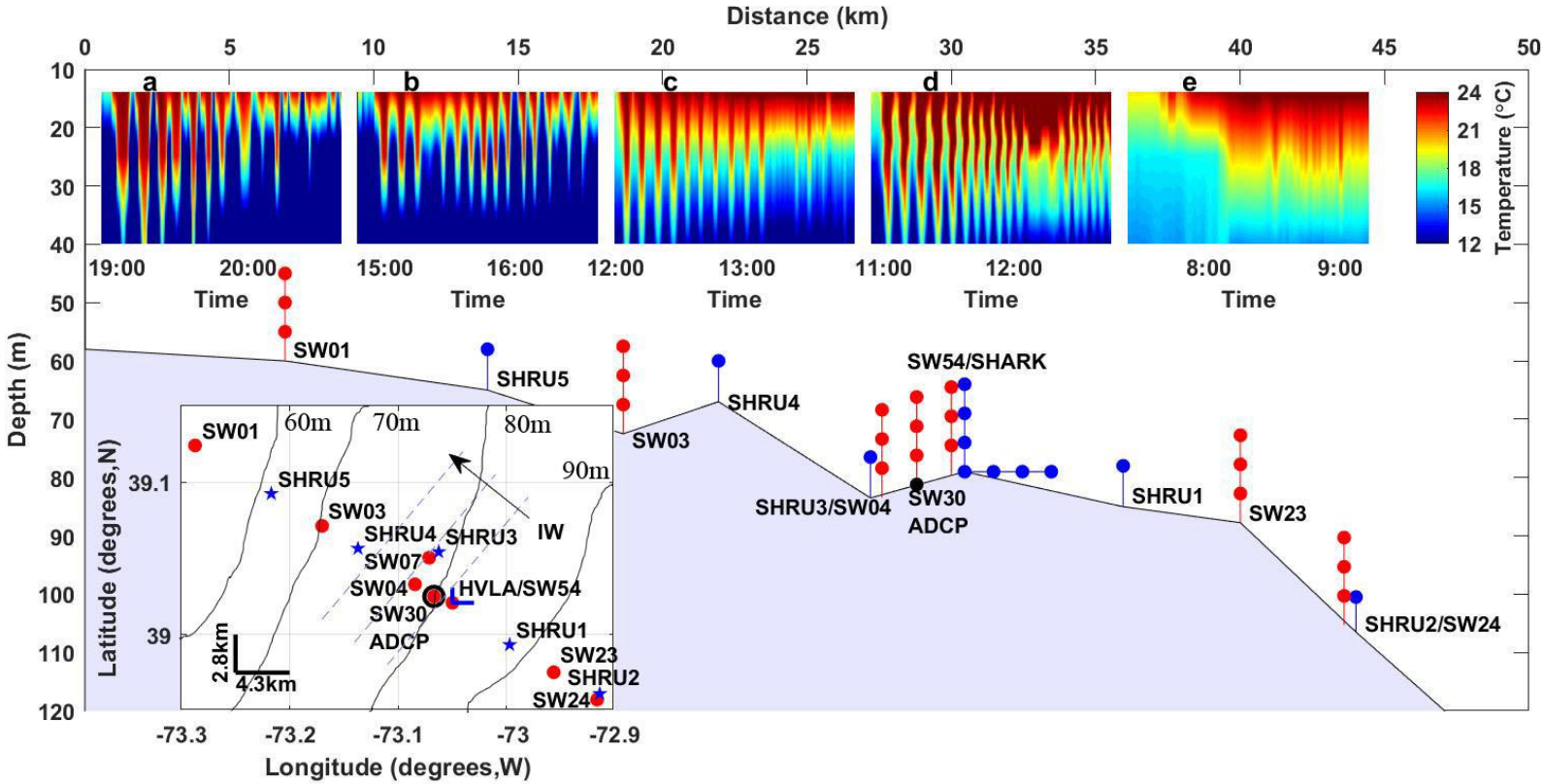

Figure 5.1. Evolution of a train of nonlinear internal waves over the site of the Shallow Water 2006 (SW'06) experiment. Positions of thermistor chains SW01, SW03, SW04, SW07, SW23, SW 24, SW30, SW54, single-hydrophone acoustic receivers SHRU1, SHRU 2, SHRU3, SHRU4, SHRU5 and hydrophone array HVLA Shark as well as wave fronts (dashed lines) and the direction of propagation (arrow) of an internal wave train are indicated in the map in the lower left corner. Bathymetry is shown along the straight line through SW01 and SW24. ADCP is located at the SW30. Depth dependence of water temperature as measured by SW01 (**a**), SW03 (**b**), SW04 (**c**), SW54 (**d**), and SW23 (**e**) is shown from 07:00 to 21:00 GMT on 19 August 2006 when a train of nonlinear internal waves propagated shoreward from SW23 past SW01. Time (GMT) on 19 August 2006 is shown in hours and minutes.

By combining acoustic observations on various hydrophones with measurements of the water temperature and current velocity, we established a relationship between individual noise bursts and tidally generated, localized, soliton-like NIWs, and identified the physical mechanisms responsible for the observed acoustic manifestations of the NIWs.

The paper is organized as follows: Section 2 outlines acquisition of the data used in this study. Properties of the noise bursts are discussed in Section 3. In Section 4 we show that the observed temporal and spectral characteristics of the noise bursts can be explained in terms of three physical mechanisms of noise generation, which include turbulence of the water flow and NIW-induced sediment saltation. Section 5 puts our findings into the broader context of previous research on sediment-generated underwater noise and sediment resuspension by NIWs. The results of the work are summarized in Section 6 along with their possible contributions to the study of sediment transport and of soliton-like NIWs on the continental shelf

The data used in this study were obtained in the multi-disciplinary, multi-institutional Shallow Water 2006 experiment (SW'06). The experiment was carried out in July–September, 2006, in the Mid-Atlantic Bight on the continental shelf off New Jersey (Newhall et al., 2007; Tang et al., 2007; Lynch & Tang, 2008; Xue et al., 2014). A bathymetric map of the experiment site is shown in the lower left corner of Figure 1. Water depth in this area decreases gradually from about 120 m near the shelf break to 55–60 m 40 km from the shelf break. The summer water temperature profile was characterized by a monotone temperature decrease from the surface to the seafloor and a rather strong thermocline with about 12^{o}C temperature drop between 10 and 25 m depths. The corresponding sound speed profile was at its minimum on the seafloor and provided for a bottom-interacting guided sound propagation.

The site of the experiment is characterized by a strong internal gravity wave activity, which is well documented (Tang et al., 2007; Xue et al., 2014). Approximately twice a day, a strong NIW is generated around the shelf break as a result of interaction of tides with the bathymetry. NIWs move from the shelf break shoreward in the northwest direction, largely along the bathymetry gradient. Over the two-month duration of the experiment, tens of events were registered of NIW train passages through the instrumented site. Direction of propagation and surface structure (shape of wavefronts, the number of waves in the train, and distance between them) were obtained using satellite images (Xue et al., 2014), which show a rather narrow spread

of NIW propagation directions in the horizontal plane. NIW propagation directions were nearly parallel to the across-shelf line, along which a suite of acoustic sensors, thermistor chains, and acoustic Doppler current profilers (ADCPs) was deployed (Figure 1).

Detailed information about the three-dimensional structure and temporal evolution of the NIW trains was obtained using a few tens of thermistor chains (Newhall et al., 2007; Tang et al., 2007; Lynch & Tang, 2008). These data show that the NIWs were depression waves. As it moved from the shelf break towards the shore, each NIW evolved into a wave train consisting of up to 10–12 localized, soliton-like waves (Figure 1). The isopycnal depression amplitude of the individual localized waves was largest near the leading front of the train and gradually decreased toward its back end. The observed wave trains were qualitatively similar to the D-noidal model of NIWs (Apel, 2003).

Observations of strong NIW events on the 17, 18, 19 and 22 of August, 2006, have been selected for the present study. These events had quite similar patterns of NIW movement and, in turn, similar features of acoustic intensity fluctuations. Consider a 12-hour time period from 08:00–20:00 GMT on August 19, 2006. The period started with the appearance of an NIW in the shelf-break area. NIW evolution process can be analyzed using temperature records from a cluster of 16 thermistor chains in a 2x2 km square-shaped area (Newhall et al., 2007). Positions of selected thermistor chains, denoted by letters SW, and of the acoustic receiving systems, single-hydrophone receiving units (SHRUs) and the L-shaped horizontal and vertical line hydrophone array (HVLA) Shark, are shown on the bathymetric map in Figure 1. SHRUs were moored with heavy anchors, with the hydrophone located about 7 m above the seafloor. HVLA Shark consisted of a 16-hydrophone vertical linear array (VLA), which extended through most of the water column, and a 450m-long, 32-hydrophone, near-bottom horizontal linear array (HLA).

Five color panels in Figure 1 show the temperature records obtained by five thermistor chains located at various distances from the shelf break. Each temperature record was 90 minutes long, corresponding to the time it took an NIW train to pass each thermistor chain. It can be seen that the NIW train was generated in the area between SW23 (where we can see the forward front of an unstructured NIW) and SW54, where NIW had developed a well-defined across-the-front structure. The distance between SW23 and SW24 was about 14 km. At SW54, the NIW contained 12 distinct, soliton-like waves (peaks of the depression of the isothermal surfaces) with

amplitudes of the thermocline's displacement from equilibrium position of up to 25–30 m (Figure 1). As the NIW train moved shoreward, it passed consecutively a set of acoustic receivers, including the HVLA Shark and five SHRUs, which were located a distance of 5–8 km from one other along a straight line. The NIW train evolved as it propagated; the amplitudes and the number of the localized waves in the train changed (Figure 1). One can estimate the speed v of the NIW train using distance between thermistor chains and the temporal interval between arrivals of the NIW leading front. From such an estimate we obtained $v \sim 0.9$ m/s, length of the NIW trains $L \sim 5$ km, quasi-period of the spatial structure inside the NIW train $l \sim 250$–300 m. The corresponding scale of temporal variability was 5–7 minutes.

For the entire duration of the SW'06 experiment, acoustic pressure was continuously measured by the SHRU and HVLA Shark hydrophones. The acoustic data was recorded with the common sampling rate of 9750 Hz for all hydrophones. Measured time series $p(t)$ of acoustic pressure p are used below for calculation of various characteristics of the acoustic field, including its intensity, frequency spectrum, and spectrograms. In addition, current velocity was measured using acoustic Doppler current profiles (ADCPs). The data obtained with a moored ADCP (Figure 5.1) that was used in this study is described in Section 2.

5.2 Observations of Noise Bursts

The vertical line array of HVLA Shark was collocated with thermistor chain SW54 (Figure 5.1) but other acoustic receivers, including SHRU1, SHRU4, and SHRU5, had no collocated temperature sensors. Figure 5. 2 presents a diagram demonstrating the connection between NIW passage and observations of elevated noise intensity at different points across the shelf. In the top panel, the vertical axis denotes distance along the straight line through locations of the hydrophones and thermistor chains, with 0 of this axis corresponding to the position of the thermistor chain SW01. The horizontal axis represents time and covers 15 hours of observations. Temporal variation of temperature at different locations is illustrated by temperature measurements (denoted by the letter ***t***), by one thermistor at 40 m depth of each of 5 thermistor chains. Note that all positions of the forward front of NIW train in the range-time plane were located approximately along a straight line, which indicates a nearly constant speed of the NIW train of 0.9 m/s. Time series of measured sound intensity are shown for four SHRUs and one of the hydrophones (channel 40) of HVLA Shark. The parts of these records that show large, rapid

increases (bursts) of the noise intensity are indicated by boxes ***a-e***. Figure 5.2 shows that the noise bursts were observed when the NIW train traveled past the acoustic sensor.

More detailed information about the frequency content of acoustic signals and its time dependence can be obtained using spectrograms. Spectrograms *S* (*f, t*) have been calculated in the frequency range 10-4000 Hz as follows:

$$S(f,t) = |\int W(\tau - t)\, p(\tau)\, exp(-2\pi i f \tau)\, d\tau|^2. \quad (5.1)$$

Here $p(t)$ is a measured time series of acoustic pressure, f is sound frequency, and $W(\tau - t)$ is the time window. Here a Kaiser window (Kaiser & Schafer, 1980) incorporating 1024 pressure samples was used. Figure 5.2 shows spectrograms of noise recorded when a NIW train was moving consecutively through positions of SHRU1 (panel ***a***), HVLA Shark (channel 40, hydrophone in the center of HLA, panel ***b***), and SHRUs 3, 4, 5 (panels ***c, d, e*** , respectively). HVLA Shark is represented in Figure 5.2 by measurements on channel 40, which was a hydrophone at the center of the horizontal line array.

In the area of NIW generation, where water depth was about 100 m, fluctuations of acoustic intensity were relatively weak, especially at frequencies above 1 kHz (see panel ***a*** in Figure 5.2), although there was some correlation of the intensity fluctuations with NIWs. In particular, the temporal scale of the sound variability of about 7 minutes corresponded to the time interval between separate localized waves with the NIW train. A similar situation took place on the HVLA Shark hydrophones (panel ***b***). Noise intensity was significantly weaker on the vertical part of the L-shaped array than on its horizontal part as was previously reported by Serebryany et al. (2008b).

Acoustic intensity fluctuations increased as the NIW train moved to shallower water. Panel ***d*** in Figure 2 depicts the spectrogram of noise recorded by SHRU4, which was located between thermistor chains SW03 and SW04. Comparison of the shapes of the NIW train recorded by these thermistor chains (panels ***b*** and ***c*** in Figure 1) shows that the main parameters of the NIW train – the number of individual localized waves, their amplitudes (~ 30–40 m), and the time interval between the waves (~ 7 min) – did not change significantly between SW03 and SW04. Hence, SW03 and SW04 measurements should provide a suitable representation of the NIW train at SHRU4.

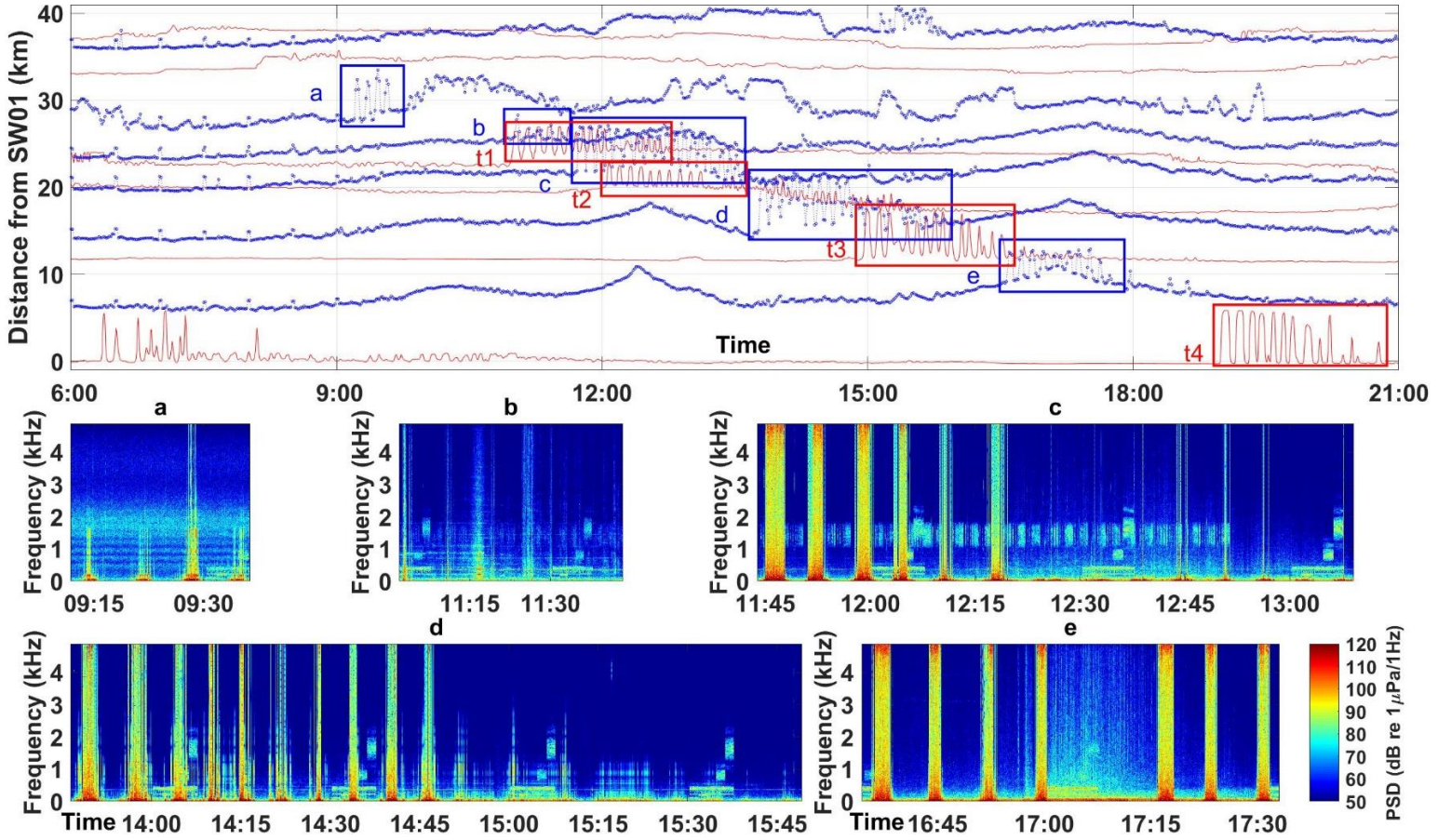

Figure 5.2. Time histories of water temperature and acoustic intensity at various points along the path of propagating internal wave train. Temperature records of thermistors at the depth of 40 m are denoted by letter T and depicted in red for thermistor chains SW23, SW54, SW04, SW03, and SW01. Time intervals of appearance of the NIW train are denoted t1, t2, t3, t4 for the last four chains (SW23 does not show NIWs) and boxed. Sound intensity records by SHRUs 1, 3, 4, and 5 and hydrophone 40 of HVLA Shark are depicted in blue. For visibility, the time dependencies recorded by individual sensors are shifted vertically in proportion to the distance from the sensor to SW01. Time intervals with strong fluctuations of acoustic pressure are boxed and marked ***a*** for SHRU1, ***b*** for HVLA Shark, ***c*** for SHRU3, ***d*** SHRU4, and *e* SHRU5. Time (GMT) on 19 August 2006 is shown in hours and minutes. Five color panels in the lower part of the figure show the spectrograms corresponding to the sound intensity

Comparison of the temperature record ***c*** in Figure 5.1 and spectrogram ***d*** in Figure 2 demonstrated a good agreement between the temporal scales (total duration of about 1 hour, the interval between peaks ~ 7 min) in the temperature and intensity measurements. The agreement between time dependencies of the temperature variations and acoustic spectra indicated a causal relation between NIWs and noise intensity fluctuations at SHRU4 and, by extension, at other locations on the continental shelf.

The SW3 and SW4 temperature records (panels ***b*** and ***c*** in Figure 5.1) have 12 large peaks, which corresponded to individual localized internal waves. Amplitude of the waves tended to decrease toward the tail of the NIW train. The data from acoustic sensors SHRU 3 and SHRU4, which were located between the thermistor chains SW3 and SW4 (Figure 1), showed fewer peaks in the spectrograms. There are 6 strong, broadband noise bursts in SHRU3 data in panel ***c*** in Figure 2. Water depth was about 68 m and 82 m at SHRU4 and SHRU3 locations respectively. For SHRU4, which was located in shallower water of 68 m depth, panel ***d*** in Figure 2 shows 10 strong, broadband noise bursts. We relate the observed difference in the number of noise bursts to the difference in the speed of the near-bottom currents induced by NIWs at the two sites. As discussed in Section 4, speed of the near-bottom currents increased with increasing NIW amplitude and decreasing water depth (see Eq. **Error! Reference source not found.**). The change in the number of noise bursts at frequencies above a few hundred Hertz suggests that acoustic noise generation has a threshold character. Number of noise bursts is equal to number of individual localized peaks in the NIW train, having speed of near-bottom current larger than threshold value.

The value of the threshold can be estimated by combining the noise intensity and water temperature measurements with current velocity data. Current velocity was not measured at acoustic sensor locations. We used the velocity data obtained with an acoustic Doppler current profiler, which was collocated with the thermistor chain SW30. Figure 5.3 compares the ADCP measurements with simultaneous measurements of the water temperature profile by thermistor chains SW07 and SW30 and acoustic observations at SHRU3. In the direction across the NIW wavefront, SW30 and ADCP preceded SHRU3 by about 700 m, and SW07 was behind SHRU3 by about 500 m (Figure 5.1). This geometry was responsible for the 10–15 minutes shifts of the respective temperature and current velocity manifestations of an NIW wave train (Figure 3b–d) from its acoustic manifestations (Figure 3a). The wave train evolved as it propagated. Isothermal

depressions had five and seven strong peaks following the leading front of the NIW train at SW07 and at SW30, respectively (Figure 5.3b, c). It is reasonable to assume that there were six strong peaks at SHRU3, which is located between SW07 and at SW30. Figure 5.3a shows six strong, broadband noise bursts following the leading front of the NIW train.

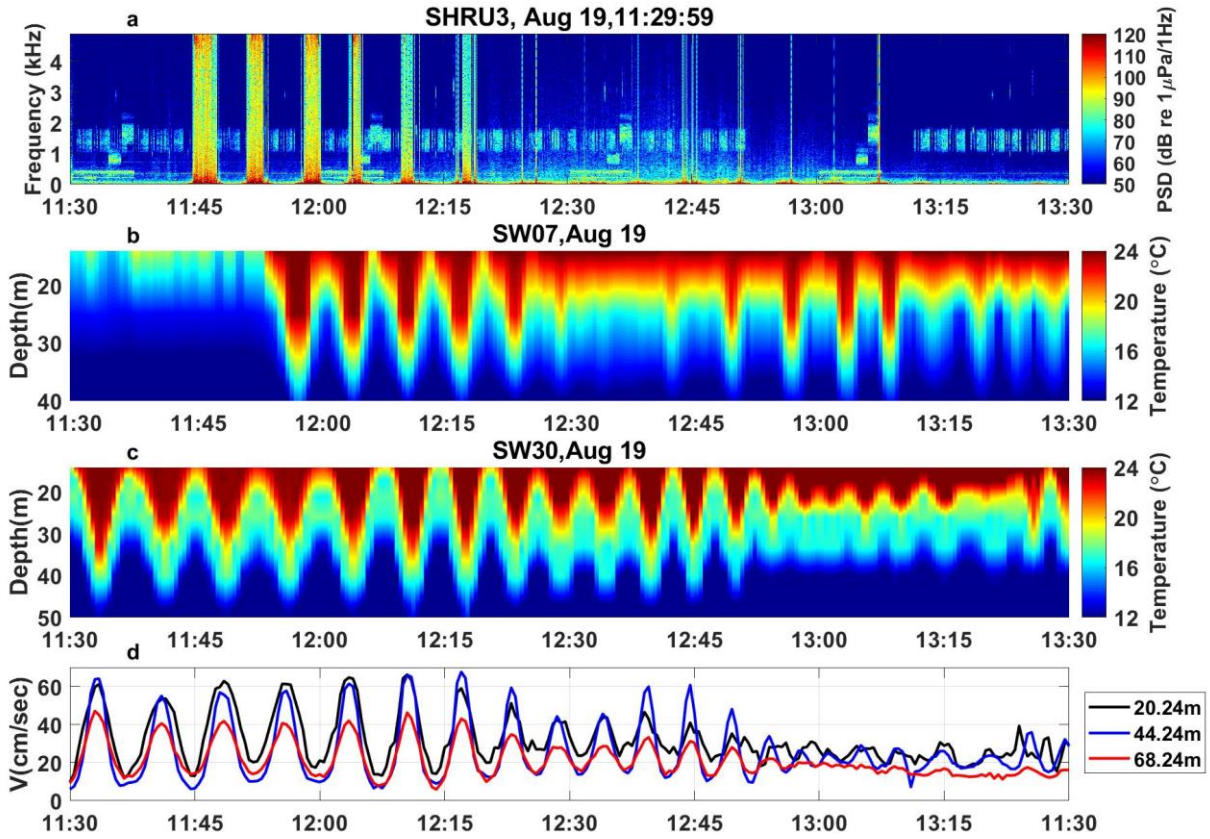

Figure 5.3. Temperature, current velocity, and acoustic manifestations of an NIW train in the vicinity of the acoustic receiver SHRU3. (**a**) Spectrogram of acoustic noise recorded by SHRU3. (**b**) Time history of the water temperature on the thermistor chain SW07. (**c**) Time history of the water temperature on the thermistor chain SW30. (**d**) Time-dependence of the horizontal current velocity at three depths. Time (GMT) on 19 August 2006 is shown in hours and minutes.

Horizontal velocity of the water flow caused by the NIW train reached its maximum when the isothermal depression was at maximum (Figure 5.3c, d). Observed velocities reached –

and for the strongest peaks exceeded – 60 cm/s below the thermocline. Velocity magnitude gradually declined with depth below the thermocline and decreased by a factor of about 1.5 near the bottom (Figure 3d). Comparison of the spectrogram of acoustic noise with the ADCP measurements indicated that strong, broadband noise bursts occurred when the NIW-induced near-bottom current exceeded a threshold value of about 40 cm/s.

These results suggest that the noise bursts occurred around the time when a peak of isothermal depression passed the observation point. A more precise relation between the phase of the isothermal displacement and acoustic noise can be obtained using the HVLA Shark data, since SW54 thermistors were attached to the vertical part of the hydrophone array. Figure 5.4 compares simultaneous, collocated measurements of the water temperature profile and sound intensity on the lowest hydrophone on the vertical part of the array. The figure demonstrates that maximum noise intensity was observed when the NIW-induced displacement of isothermal surface was at maximum. The time-dependent acoustic intensity *I* and intensity level *IL* were calculated as follows:

$$I(t) = \frac{1}{2\rho c \Delta t} \int_t^{t+\Delta t} p^2(\tau) d\tau, \tag{5.2}$$

$$IL(t) = 10\, log_{10} \left[\frac{I(t)}{I_0}\right]. \tag{5.3}$$

Here Δt = 1 s is the average time, ρ and c are the density and sound speed in water, and I_0 is the reference intensity, corresponding to the root mean square acoustic pressure of 1 μPa. The noise generated by NIWs on near-bottom hydrophones was as strong as, if not stronger, than any signal received or noise of a different origin. This is illustrated in Figure 5.5, which shows the time dependence of acoustic intensity recorded by SHRU5 during a full day. A number of sound generation mechanisms contributed to the observed acoustic field. For instance, from 04:00 to 17:00 there were prominent signals from the research sources (Newhall et al., 2007; Lynch & Tang, 2008), which were towed through the experiment site. Strong low-frequency noise, presumably due to shipping and/or a stormy condition, was present from about 10:00-14:00. This noise was superimposed on and overshadows signals from the research sources.

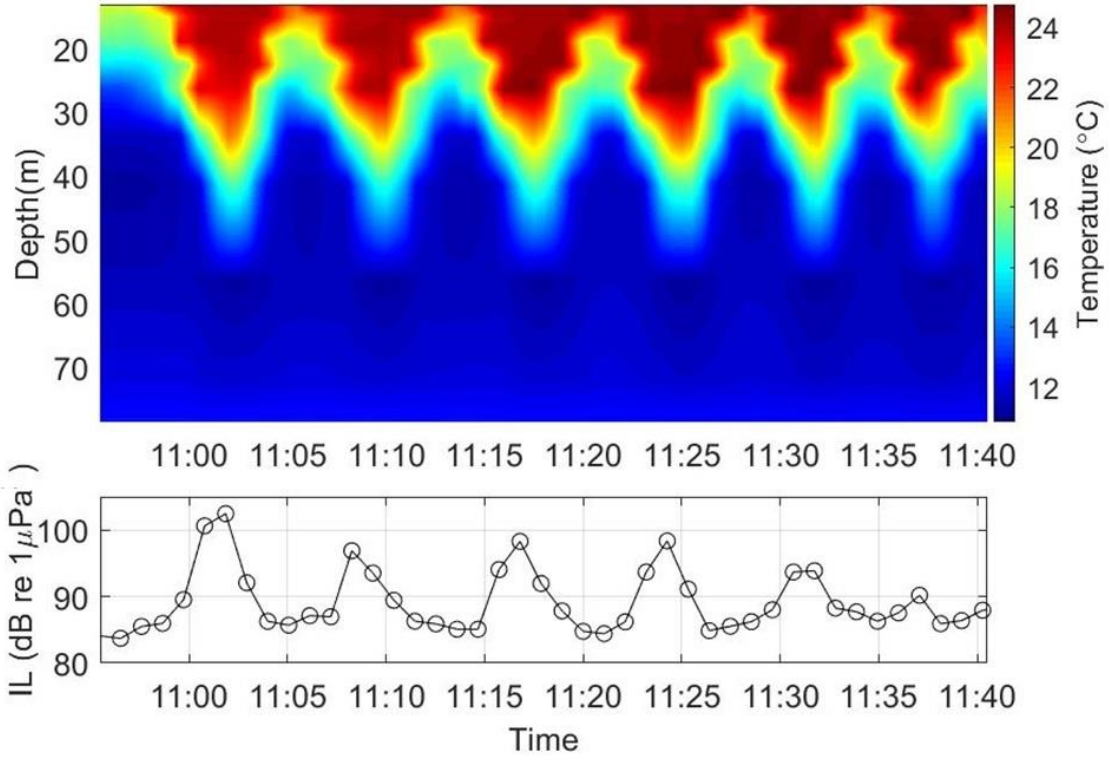

Figure 5.4. Temporal variations of the temperature depth dependence measured by thermistor chain SW54 (upper panel) and noise intensity on a collocated hydrophone (lower panel). Time (GMT) on 19 August 2006 is shown in hours and minutes.

NIW-induced noise intensity bursts appeared as a sequence of high and narrow, quasi-periodic intensity peaks in the 16:30-17:30 time interval. Intensity of the noise bursts reached 150-155 dB re 1 μPa. It exceeded the background noise intensity of 110-115 dB re 1 μPa by 40 dB, or four orders of magnitude.

5.3. Mechanisms of Noise Generation

Noise intensity, its time dependence, and the spectral content of the noise showed significant variability depending on hydrophone position and position of NIW train. Three distinct types of acoustic noise that accompanied the passage of NIWs can be identified, which combined to explain the bulk of observations (see Figure 5.6).

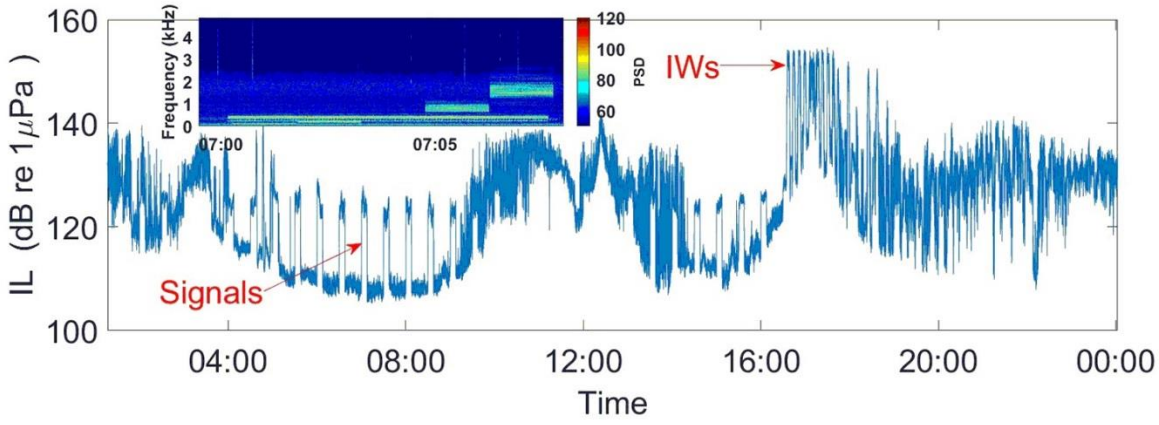

Figure 5.5. Temporal variation of the acoustic intensity measured by SHRU5. Time (GMT) on 19 August 2006 is shown in hours and minutes. The insert shows the spectrogram of a nine-minute section of the pressure record and illustrates contributions of research sound sources. Color shows power spectral density of total acoustic field in dB re 1 μPa/Hz.

These types are (i) low-frequency noise, which is illustrated in Figures 6a and 6b, (ii) noise spikes of ~1 s duration with spectral peaks located below approximately 1 kHz (Figure 5.5c), and (iii) more frequent, shorter-duration spikes with prominent high-frequency content above 3 kHz, which subsequently merged to become a continuous signal of a few minutes in duration (Figure 5.6d).

The low-frequency noise was most pronounced at infrasonic frequencies below 10 Hz (Figure 5.6b). It was observed almost always as each soliton-like wave in the NIW train passed the acoustic receiver. Acoustic intensity increased rapidly with the magnitude of pycnocline depression (see the time dependence of noise spectral density at frequencies below 10 Hz in Figure 6b). The low-frequency noise was clearly observed on all SHRUs and on VLA hydrophones, where noise intensity was only weakly dependent on the hydrophone depth.

We interpret the low-frequency noise that was observed as flow noise (Strasberg, 1979; Webb, 1988; Bassett et al., 2014). Flow noise, also known as pseudosound, results from advection of pressure fluctuations in a turbulent flow past the sensor. Pressure fluctuations include ambient fluctuations in a turbulent flow as well as pressure pulsations due to eddy

shedding when the flow interacts with the sensor and the entire mooring. Intensity of flow noise is known to increase with decreasing frequency (Strasberg, 1979; Webb, 1988; Bassett et al., 2014). Interpretation of the low-frequency noise as flow noise is supported by the apparent absence of such noise in signals on HLA hydrophones, which lie on the seafloor. For the pseudosound due to eddy shedding, by the flow past a cylinder of diameter d, the representative frequency is $f_e = St\ u/d$, where $St \sim 0.2$ is the Strouhal number and u is flow velocity (Strasberg, 1979; Webb, 1988). With NIW-induced currents of ~0.5 m/s (Serebryany et al., 2008b; see also Figure 3d), the observed upper frequency of 10 Hz is consistent with the eddy shedding by a mooring wire with $d \sim 1$ cm. The hydrophone and pressure housing have larger dimensions and contribute to lower-frequency pseudosound.

The observed strong correlation between intensity of low-frequency noise and pycnocline depression in NIWs (Figure 4) can be understood within the following simple model of NIW currents. Consider a progressive NIW with a linear wavefront, which moves with speed c along horizontal coordinate x in an ocean, where potential density jumps across a narrow pycnocline and remains constant below it. Let the water depth, unperturbed pycnocline depth, and pycnocline depression due to NIW be $H(x)$, $h(x)$, and $\eta(x - ct)$. The flow is stationary in the reference frame moving with NIW. In the long-wave approximation (Apel et al., 2007), it follows then from the continuity equation that flow velocity $u(x, t)$ below the pycnocline is

$$u = \frac{-c\eta\left(x-ct\right)}{H\left(x\right)-h\left(x\right)-\eta\left(x-ct\right)}. \tag{5.4}$$

The minus sign in the numerator in Eq. **Error! Reference source not found.** indicates that near the seafloor, water flows in the direction opposite to the direction of NIW propagation. Note that magnitude $|u|$ of the flow velocity rapidly increases with increasing pycnocline depression and, for fixed η, is inversely proportional to the distance from the perturbed pycnocline to the seafloor. For example, in the vicinity of SHRU3 the water depth was $H \approx 80$ m, thickness of thermocline $h \approx 20$ m and the pycnocline depression $\eta \approx 20$ m, and Eq. (5.4) gives $|u| = c/2 \sim 0.5$ m/s. This estimate agrees well with the ADCP measurements shown in Figure 5.3d.

The key to understanding the origin of the second noise type, illustrated in Figure 6c, is the fact that it was observed only on HLA hydrophones and was not present on either VLA

hydrophones or SHRUs. HLA hydrophones lay on the seafloor, while the VLA and SHRU hydrophones were located at least 6 m above it. Moreover, the type-two noise was at maximum on hydrophones in the middle of the HLA, and no noise of this type was observed on the hydrophones at both ends of the array, which were fixed by heavy anchors (Newhall et al., 2007). All the observed features of type-two noise are consistent with hydrophones being dragged along the seafloor by NIW-induced near-bottom currents, with the stronger noise caused by the bigger displacements that occurred away from the anchors. This interpretation was proposed by Serebryany et al. (2008a, 2008b), who were the first to report observations of NIW-associated noise on several HLA hydrophones in the middle of the array.

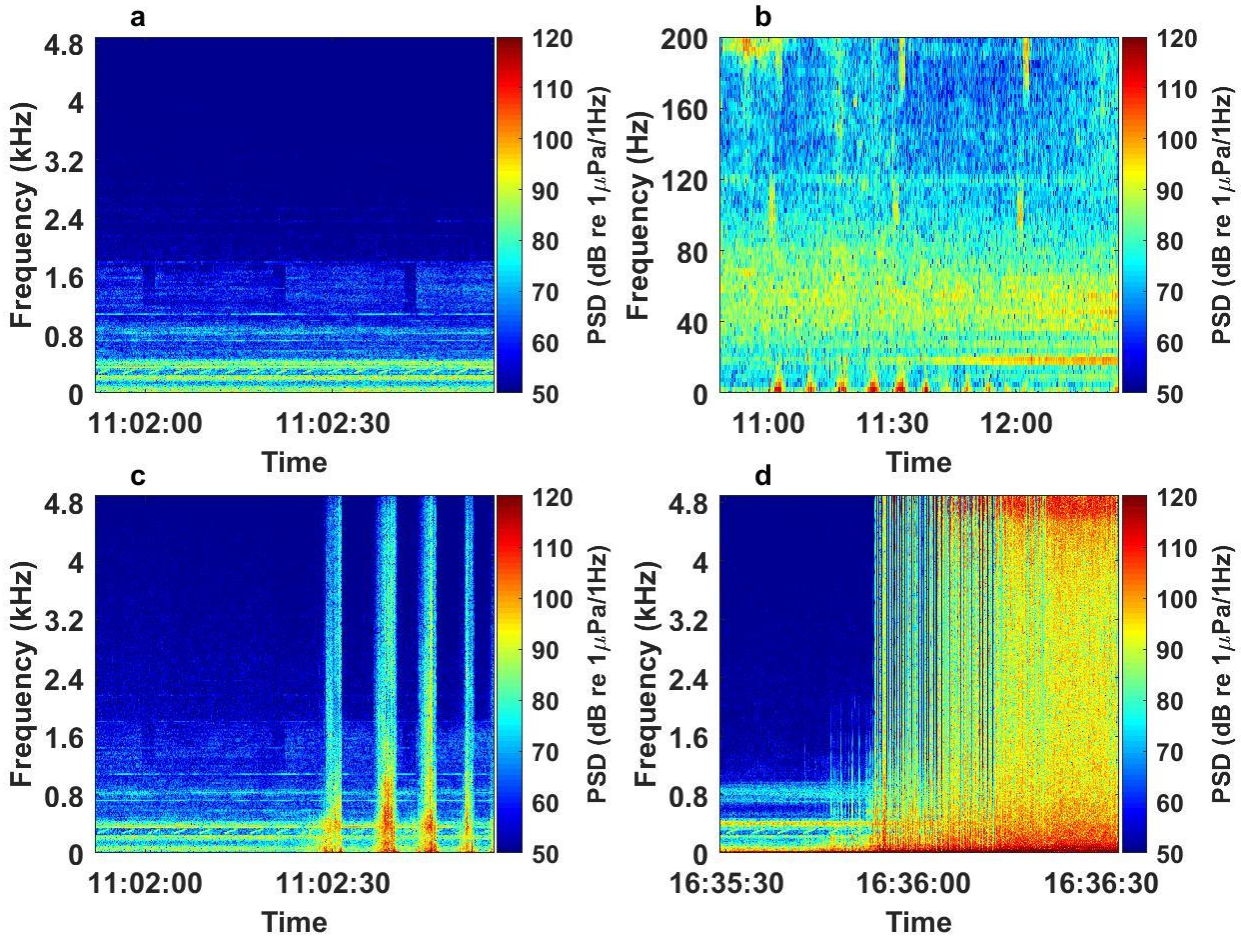

Figure 5.6. Spectrograms of acoustic field recorded by hydrophones on vertical (VLA) and horizontal (HLA) arrays during passage of a train of nonlinear internal waves. Spectrograms are shown of acoustic pressure on a VLA hydrophone at depth of 62 m (**a**); low-frequency part of the acoustic pressure on the same hydrophone (**b**); on a hydrophone in the middle of HLA (**c**);

and on single-hydrophone receiver SHRU5 (**d**). Time (GMT) on 19 August 2006 is shown in hours minutes, and seconds.

The third and most intense type of observed noise is illustrated in Figure 5.6d, which uses the SHRU5 data. We interpret this noise type as the noise generated by moving sediments that had been mobilized by the NIW-induced near-bottom currents. After sediment particles leave the seafloor, they generate acoustic waves (noise) by colliding with each other and with the stationary seabed as well as with near-bottom acoustic sensors and/or their housing. Mobilization of sediments and dynamics of the suspended sediment particles are controlled by the composition of surficial sediments and the near-bottom current velocity.

To our knowledge, NIW-induced sediment generated noise (SGN) has not been previously described. However, there is extensive literature on SGN produced by other kinds of currents such as river flow, orbital velocities in surface gravity waves, and tidal currents (Bassett, 2013; Thorne, 2014). SGN has been measured using underwater sensors and seismometers on dry land (Roth et al., 2016). SGN properties have been studied in laboratory experiments (Thorne, 1986), in rivers (Roth et al., 2016; Geay et al., 2017; Petrut et al., 2018) as well as in straits (Thorne, 1986, Bassett, 2013) and the surf zone at sea (Voulgarist et al., 1999). Bassett et al. (2013) investigated SGN caused by currents in a tidal channel in Puget Sound. They found that a near-bottom current velocity above a critical value of 50–60 cm/s was necessary to produce SGN and that the shape of the SGN spectrum depended on sediment grain size. SGN was typically most pronounced above 2 kHz with a maximum spectral density at frequencies of 10–15 kHz.

The threshold character, frequency content, and the value of the current velocity threshold (Section 3) of the type-three NIW-induced noise are consistent with the previously observed SGN due to tidal currents in the ocean, which supports our interpretation of the mechanisms of the type-three noise. The difference in the current velocity thresholds (~40 cm/s vs. 50–60 cm/s) can be attributed to a difference in the sediment grain sizes at the experiment sites on the New Jersey shelf and in Puget Sound.

Figure 5.7 compares power spectra and intensity of the NIW-induced noise on three hydrophones, where one of the three noise types dominates. We used the data obtained with

SHRU5, one VLA hydrophone, and one HLA hydrophone. These are the same sensors that were used in Figure 5.6 to illustrate the differences between the three noise types. Power spectra of the background ambient noise are usually modeled using the well-known Wenz curves (Wenz, 1962). When there were no NIWs in the vicinity of the sensors, all three hydrophones recorded signals with rather similar spectra at all frequencies above 10 Hz (Figure 5.7a). The measured spectra were close to the Wenz curve if contributions of the spectral peaks due to linear frequency modulated signals around 300 Hz and 500 Hz and other signals emitted by known research sound sources are excluded (Newhall et al., 2007; Lynch & Tang, 2008).

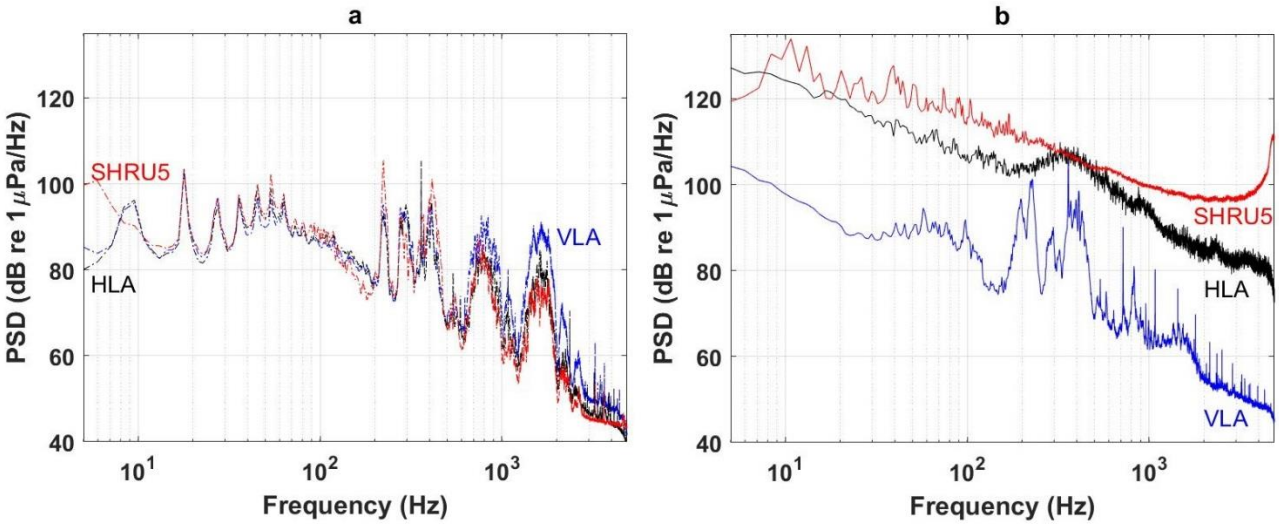

Figure 5.7. Power spectra of acoustic pressure recorded by SHRU5 and hydrophones on vertical and horizontal arrays when nonlinear internal waves are absent (**a**) or present (**b**). The power spectra are calculated for the same hydrophones as in Figure 5.6.

In the presence of an NIW train (Figure 5.7b), the spectrum of the acoustic pressure on the VLA hydrophone did not change appreciably, except at frequencies below 10 Hz. This is consistent with the flow noise properties. Signals from the research sources could still be clearly seen above the noise background. In contrast, very strong, broadband increase of noise level (Figure 5.7b) occurred on HLA, which was dragged along the seafloor by the NIW-induced

current. The spectrum retained manifestations of the research sources in the 300–1000 Hz frequency band. At SHRU5, where the velocity of the NIW-induced near-bottom current exceeded the threshold for type-three noise generation, there was a broadband increase of the spectral level of about 30 dB between 10 Hz and 2 kHz and a rather sharp increase of the spectral level (up to ~ 40-50 dB relative to the background noise level) at frequencies above 2 kHz (Figure 7b). The spectral maximum occurred at frequencies above the highest frequency that can be resolved with the 9750 Hz sampling rate of the SHRU5 measurements, as expected for sediment generated noise (Thorne, 1986; Bassett et al., 2013; Petrut et al., 2018). At SHRU5, NIW-induced SGN surpassed contributions of all other sources of sound at every frequency.

SGN is an acoustic manifestation of sediment mobilization by water flow. While NIW-induced SGN apparently has not been studied previously, there exists a large body of work on the effects that NIWs have on marine sediments on the continental shelf, and there is no doubt that sediment mobilization by NIWs does occur. It is known that the boundary layer at the footprint of NIW can became hydrodynamically unstable, and this instability results in an increase of the sediment resuspension rate (Carr & Davies, 2006). Moreover, any increase in the turbulent energy due to the hydrodynamic instability can maintain a higher sediment concentration in the water column. Bogucki et al. (1997) reported observations and analysis of the sediment resuspension/saltation produced by NIWs on the Californian continental shelf. Quaresma et al. (2007) studied sediment resuspension by NIWs using data obtained on the Portuguese continental shelf, where the bathymetry and sound speed profile are similar to those at the SW’06 site. It was shown that water turbidity and the concentration of entrained sediment particles in the water changed synchronously with the thermocline displacement. During the maximum thermocline displacement near the leading front of an NIW train, sediment grains were found at far as 35 m from the seafloor. Another example of strong variations in water turbidity due to sediment resuspension by NIWs and formation of an intermediate nepheloid layer were reported by Masunaga et al. (2015). Observations of NIW-induced sediment resuspension are supported by theory and by the results of numerical simulations (Cacchione & Southard, 1974; Bogucki & Redekopp, 1999; Stastna & Lamb, 2008; Olsthoorn & Stastna, 2014; Bourgault et al., 2014).

SGN theory is based on a model of collisions between two sediment particles or between a particle with a slab (obstacle) (Thorne & Foden, 1988; Bassett et al., 2013; Thorne, 2014). The

spectrum of the radiated sound has a maximum, and the centroid frequency of SGN $f_r \approx C/D^{0.9}$, where D is an effective diameter of sediment particles and C is a function of their material properties; for instance, $f_r \approx 15$ kHz for basalt particles with $D = 2.5$ mm. Acoustic intensity of SGN increases with current velocity and was found to be an acceptable proxy for bedload transport (Thorne, 2014). SGN theory, modeling, and experimental data are reviewed by Bassett et al. (2013) and Thorne (2014).

Recording and analyzing SGN can serve as minimally invasive, continuous means of measurement for sediment transport and for estimating dimensions of mobile particles (Thorne, 2014). This approach was applied to study sediment transport by various types of water flow, including rivers, tidal currents in straits, and surface gravity wave-induced flows in the surf zone (Thorne, 1986; Mason et al., 2007; Thorne, 2014; Geay et al., 2017; Petrut et al., 2018). Results of SGN analysis, including estimates of grain size distribution, agree well with the direct sampling methods (Petrut et al., 2018). Observations of NIW-induced noise bursts and identification of SGN as a dominant contribution to their intensity on near-bottom sensors, raise the possibility of extending the passive acoustic measurements of sediment transport to the sediment mobilization by strong NIWs on continental shelves. The inherent ability of the technique to provide long term series of autonomous observations is even more important on continental shelves than for measurements in rivers or in the surf zone. Moreover, measurements of the noise bursts with autonomous, moored, single-hydrophone receivers can potentially contribute to improved quantitative understanding of NIW-induced near-bottom currents as well as NIW amplitudes and their temporal and spatial variability on the continental shelf.

Sediment-generated noise has an ambient component, which results from sediment particles' collisions with each other and the seabed, as well as a sensor-related component due to particle impacts on the acoustic sensor or its housing. Observations of sediment transport in rivers with sensors on dry land (Roth et al., 2016) offer clear evidence of the ambient component of SGN. On the other hand, sensors are routinely augmented by pipes and plates to increase particle impacts for the purposes of measuring coarse gravel transport (Thorne, 2014). Further research is needed to quantify the relative weight of the ambient and sensor-related components of SGN in the NIW-generated noise bursts and the variation of the weight with distance to the seafloor.

Given its high intensity, NIW-induced SGN may present significant challenges for the continuous operation of near-bottom acoustic sensors deployed for underwater communication, detection and tracking of biological or man-made sound sources, or remote sensing of the water column and seabed properties. SGN would be equally detrimental whether ambient or sensor-related. Spectral and spatial characteristics of the NIW-induced noise need to be understood and considered during design and deployment of acoustic systems on continental shelves.

In this study, we used a network of temperature, current velocity, and acoustic sensors deployed on the continental shelf off of New Jersey to relate the occurrence of large, transient increases in acoustic noise intensity (noise bursts) to trains of strongly nonlinear internal waves and, more specifically, to individual localized, soliton-like waves that form the trains. The noise bursts occurred in sequences of 60–80 minutes, the duration of which equals the time it took an NIW train to travel past an observation point on the New Jersey shelf. Individual noise bursts lasted for 5–7 minutes and coincided in time with passage of a single soliton-like internal wave past the hydrophone. Very large increases in the spectral density and broadband intensity of noise, of up to 50 dB relative to background, were observed on hydrophones located 6–7 m above the seafloor. The peak acoustic intensity and the spectral content of the noise bursts were controlled by the amplitude of individual soliton-like internal waves and were most directly related to the velocity of the NIW-induced near-bottom currents.

The noise burst emergence and observed variations in their intensity and spectral content with water depth, hydrophone elevation above the seafloor, and NIW amplitude have been explained in terms of three noise generation mechanisms. The low-frequency (below a few tens of Hertz) component of the noise bursts represents the flow noise that occurs due to advection of turbulent pressure pulsations past an acoustic sensor. Hydrophones lying on the seafloor recorded broadband noise, which resulted from the hydrophones being dragged along the seafloor by NIW-induced currents. The strongest noise bursts were associated with sediment-generated noise (SGN). Acoustic waves are generated when sediment is mobilized by NIW currents, and sediment particles collide with each other, with the stationary seabed, and with acoustic sensors. SGN was most pronounced at frequencies above 2 kHz. A distinctive feature of SGN is its threshold character. NIW-induced near-bottom currents stronger than about 40 cm/s were found to be necessary to initiate SGN. Compared to previously described oceanic observations of SGN in tidal channels and the near-shore surf zone, NIW-induced SGN occurs

on the continental shelf at significantly larger water depths and drastically increases the extent of the seafloor area, where SGN occurrence should be expected.

NIW-generated noise bursts are one of the strongest reported acoustic effects of internal waves in the ocean. The noise bursts may present challenges to continuous acoustic communication and acoustic monitoring of the ocean using near-bottom sensors. On the other hand, measurements of the noise bursts with autonomous, single-hydrophone receivers can potentially contribute to improved quantitative understanding of NIW-induced near-bottom currents and sediment transport by internal waves on the continental shelf. Further research is needed to fully characterize the spectrum of NIW-induced acoustic noise, its depth-dependence, relative contributions of the ambient and sensor-related components of sediment generated noise as well as the directivity and correlation properties of the ambient component of the NIW-generated acoustic noise.

REFERENCES

1. Amiri-Simkooei, A. R., Koop, L., van der Reijden, K. J., Snellen, M., & Simons, D. G. (2019). Seafloor characterization using multibeam echosounder backscatter data: methodology and results in the North Sea. *Geosciences*, *9*(7), 292.
2. Auger, F., & Flandrin, P. (1995). Improving the readability of time-frequency and time-scale representations by the reassignment method. *IEEE Transactions on signal processing*, *43*(5), 1068-1089.
3. Apel, J. (2003). A new analytical model for internal solitons in the ocean. *Journal of Physical Oceanography*, *33***,** 2247–2268.
4. Apel, J. R., Ostrovsky, L. A., Stepanyants, Y. A., & Lynch, J. F. (2007). Internal solitons in the ocean and their effect on underwater sound. *Journal of the Acoustical Society of America*, *121* (2), 695–722
5. Badiey, M., Mu, Y., Lynch, J., Apel, J., & Wolf, S. (2002). Temporal and azimuthal dependence of sound propagation in shallow water with internal waves. *IEEE journal of oceanic engineering*, *27*(1), 117-129.
6. Badiey, M., Katsnelson, B. G., Lynch, J. F., Pereselkov, S., & Siegmann, W. L. (2005). Measurement and modeling of three-dimensional sound intensity variations due to shallow-water internal waves. *The Journal of the Acoustical Society of America*, *117*(2), 613-625.
7. Badiey, M., Katsnelson, B. G., Lynch, J. F., & Pereselkov, S. (2007). Frequency dependence and intensity fluctuations due to shallow water internal waves. *The Journal of the Acoustical Society of America*, *122*(2), 747-760.
8. Bassett, C., Thomson, J., & Polagye, B. L. (2013). Sediment-generated noise and bed stress in a tidal channel. *Journal of Geophysical Research: Oceans*, *118* (4), 2249–2265.
9. Bassett, C., Thomson, J., Dahl, P. H., & Polagye, B. (2014). Flow-noise and turbulence in two tidal channels. *Journal of the Acoustical Society of America*, *135* (4), 1764–1774.
10. Bourgault, D., Morsilli, M., Richards, C., Neumeier, U., & Kelley, D. E. (2014). Sediment resuspension and nepheloid layers induced by long internal solitary waves shoaling orthogonally on uniform slopes. *Continental Shelf Research*, *72*, 21–33.
11. Bogucki, D., Dickey, T., & Redekopp, L. G. (1997). Sediment resuspension and mixing by resonantly generated internal solitary waves. *Journal of Physical Oceanography*, *27* (7), 1181–1196.
12. Bogucki, D., & Redekopp, L. (1999). A mechanism for sediment resuspension by internal solitary waves. *Geophysical Research Letters*, *26* (9), 1317–1320.
13. M. S. Ballard, G. V. Frisk, and K. M. Becker, "Estimates of the temporal and spatial variability of ocean sound speed on the New Jersey shelf," J. Acoust. Soc. Am. **135**, 3316–3326 (2014).
14. Ballard M.S., K.M. Becker, and J.A. Goff, (2010) "Geoacoustic inversion for the New Jersey shelf: 3-D sediment model," IEEE J. Oceanic Eng. **35**, 28–42.
15. Bonnel, J., Dall'Osto, D. R., & Dahl, P. H. (2019). Geoacoustic inversion using vector acoustic modal dispersion. *The Journal of the Acoustical Society of America*, *146*(4), 2930-2930.

16. Baggeroer, A. B., Kuperman, W. A., & Schmidt, H. (1988). Matched field processing: Source localization in correlated noise as an optimum parameter estimation problem. *The Journal of the Acoustical Society of America*, *83*(2), 571-587.
17. Baraniuk, R. G., & Jones, D. L. (1995). Unitary equivalence: A new twist on signal processing. *IEEE transactions on signal processing*, *43*(10), 2269-2282.
18. Bonnel J., S.E. Dosso, D. Eleftherakis, and N.R. Chapman, "Trans-dimensional inversion of modal dispersion data on the New England Mud Patch," IEEE J. Ocean. Eng., in press (2019).
19. Bonnel, J., & Chapman, N. R. (2011). Geoacoustic inversion in a dispersive waveguide using warping operators. *The Journal of the Acoustical Society of America*, *130*(2), EL101-EL107.
20. Bonnel, J., Gervaise, C., Nicolas, B., & Mars, J. I. (2012). Single-receiver geoacoustic inversion using modal reversal. *The Journal of the Acoustical Society of America*, *131*(1), 119-128.
21. Bonnel, J., Caporale, S., & Thode, A. (2017). Waveguide mode amplitude estimation using warping and phase compensation. *The Journal of the Acoustical Society of America*, *141*(3), 2243-2255.
22. Bonnel J., S. E. Dosso, and N. R. Chapman, (2013) "Bayesian geoacoustic inversion of single hydrophone light bulb data using warping dispersion analysis," J. Acoust. Soc. Am. **134**, 120–130 (2013).
23. Bonnel J., Y.-T. Lin, D. Eleftherakis, J. A. Goff, S. Dosso, R. Chapman, J. H. Miller, and G. R. Potty, (2018) "Geoacoustic inversion on the New England Mud Patch using warping and dispersion curves of high-order modes," J. Acoust. Soc. Am. **143**, EL405–EL411 (2018).
24. Brooks L. A. and P. Gerstoft, "Green's function approximation from cross-correlations of 20–100 Hz noise during a tropical storm," J. Acoust. Soc. Am. **125**(2), 723-734 (2009).
25. Brooks L. A., P. Gerstoft, and D. P. Knobles, "Multichannel array diagnosis using noise cross-correlation," J. Acoust. Soc. Am. **124**(4), EL203–EL209 (2008).
26. Brown, M. G., Godin, O. A., Zang, X., Ball, J. S., Zabotin, N. A., Zabotina, L. Y., & Williams, N. J. (2016). Ocean acoustic remote sensing using ambient noise: Results from the Florida Straits. *Geophysical Journal International*, *206*(1), 574-589.
27. Brekhovskikh L. M., *Waves in Layered Media* (Academic, New York, 1960), Secs. 3, 4, 25, 29, 31.
28. Brekhovskih, L. M. and Lysanov, YP (2003) Fundamentals of Ocean Acoustics, 3-rd Ed. *Amer. Inst. Phys*.
29. Brekhovskikh L. M and O. A. Godin, *Acoustics of Layered Media. 2: Point Sources and Bounded Beams*, 2nd ed. (Springer, Berlin, 1999), Secs. 4.5, 7.2, 7.4.
30. Brown M. G., O. A. Godin, N. J. Williams, N. A. Zabotin, L. Zabotina, and G. J. Banker, (2017) "Acoustic Green's function extraction from ambient noise in a coastal ocean environment," *Geophys. Res. Lett.*, vol. 41, pp. 5555–5562, 2014.Chapman, N. An experimental benchmark for geoacoustic inversion methods. *The Journal of the Acoustical Society of America*, *142*(4), 2621-2621.

31. *Chapman, S. Chin-Bing, D. King* and *R.B. Evans*, (2003) *Benchmarking geoacoustic* inversion methods for range-dependent waveguides, *IEEE J. Oceanic Eng., 28, 320–330.*
32. Cacchione, D. A., & Southard, J. B. (1974). Incipient sediment movement by shoaling internal gravity waves. *Journal of Geophysical Research, 79* (15), 2237–2242.
33. Carr, M., & Davies, P. A. (2006). The motion of an internal solitary wave of depression over a fixed bottom boundary in a shallow, two-layer fluid. *Physics of Fluids, 18,* 016601, doi:10.1063/1.2162033.
34. Collins M. D., R. J. Cederberg, D. B. King, and S. A. Chin-Bing, (1996) "Comparison of algorithms for solving parabolic wave equations," *J. Acoust. Soc. Am.*, vol. 100, pp. 178–182, 1996.
35. Colosi, J. A., Scheer, E. K., Flatté, S. M., Cornuelle, B. D., Dzieciuch, M. A., Munk, W. H., Worcester, P. F., Howe, B. M., Mercer, J. A., Spindel, R. C., & Metzger, K. (1999). Comparisons of measured and predicted acoustic fluctuations for a 3250-km propagation experiment in the eastern North Pacific Ocean. *Journal of the Acoustical Society of America, 105*(6), 3202–3218.
36. Cohen L. (1995) Time-frequency analysis, Prentice hall, 299 P
37. Dong, H., Badiey, M., & Chapman, N. R. (2016). Geoacoustic Inversion of Airgun Data Under Influence of Internal Waves. *IEEE Journal of Oceanic Engineering*, *42*(3), 632-638.
38. Doolittle, R., Tolstoy, A., & Buckingham, M. (1988). Experimental confirmation of horizontal refraction of cw acoustic radiation from a point source in a wedge-shaped ocean environment. *The Journal of the Acoustical Society of America*, *83*(6), 2117-2125.
39. Dolan, A. (2003). A general GA toolkit implemented in Java, for experimenting with genetic algorithms and handling optimization problems.
40. Dosso S. E. (2002), Quantifying uncertainty in geoacoustic inversion J. Acoust. Soc. Am. V. 111 P. 129
41. Fallat M R and Nielson P L (2000) Hybrid geoacoustic inversion of broadband Mediterranean Sea data, J. Acoust. Soc. Am. V.107, P. 1967-77
42. Fink, M. (1992) "Time reversal of ultrasonic fields. I. Basic principles," *IEEE Trans. Ultrason. Ferroelectr. Freq. Control*, vol. 39, pp. 555–566, 1992.
43. Fink M., D. Cassereau, A. Derode, C. Prada, P. Roux, M. Tanter, J.-L. Thomas, and F. Wu, (2000) "Time-reversed acoustics," *Rep. Progr. Phys.*, vol. 63, pp. 1933–1995,.
44. Frisk G.V., K.M. Becker, S.D. Rajan, C.J. Sellers, K. Von Der Heydt, C.M. Smith, and M.S. Ballard, "Modal mapping experiment and geoacoustic inversion using sonobuoys," IEEE J. Oceanic Eng. **40**(3), 607–620 (2014).
45. Garnier, J., & Papanicolaou, G. (2016). *Passive imaging with ambient noise*. Cambridge University Press.
46. Gebbie, J., Siderius, M., Nielsen, P. L., & Miller, J. (2014). Passive localization of noise-producing targets using a compact volumetric array. *The Journal of the Acoustical Society of America*, *136*(1), 80-89.

47. Godin, O. A., Zabotin, N. A., & Goncharov, V. V. (2010). Ocean tomography with acoustic daylight. *Geophysical Research Letters*, *37*(13).
48. Godin, O. A., Katsnelson, B. G., Qin, J., Brown, M. G., Zabotin, N. A., & Zang, X. (2017). Application of time reversal to passive acoustic remote sensing of the ocean. *Acoustical Physics*, *63*(3), 309-320.
49. Godin O. A., B. Katsnelson, and T. W. Tan, (2019) "Normal mode dispersion and time warping in the coastal ocean," J. Acoust. Soc. Am. **146**(3), EL205–EL211 (2019).
50. Godin O. A., "A 2-D description of sound propagation in a horizontally-inhomogeneous ocean," J. Comput. Acoust. **10**, 123–151 (2002).
51. Godin, O. A., Brown, M. G., Zabotin, N. A., Zabotina, L. Y., & Williams, N. J. (2014). Passive acoustic measurement of flow velocity in the Straits of Florida. *Geoscience Letters*, *1*(1), 16.
52. Godin O. A., "Recovering the acoustic Green's function from ambient noise cross-correlation in an inhomogeneous moving medium," Phys. Rev. Lett. **97**, 054301 (2006).
53. Godin O.A., "Acoustic noise interferometry in a time-dependent coastal ocean," J. Acoust. Soc. Am. **143**(2), 595-604 (2018).
54. Godin O. A., M. G. Brown, N. A. Zabotin, L. Zabotina, and N. J. Williams, "Passive acoustic measurement of flow velocity in the Straits of Florida," Geosci. Lett. **1**, Art. 16 (2014).
55. Geay, T., Belleudy, P., Gervaise, C., Habersack, H., Aigner, J., Kreisler, A., Seitz H., & Laronne, J. (2017). Passive acoustic monitoring of bed load discharge in a large gravel bed river. *Journal of Geophysical Research: Earth Surface*, *122* (2), 528–545. doi:10.1002/2016JF004112.
56. Godin, O. A., Voronovich, A. G., & Goncharov, V. V. (2006). Refraction of sound in a horizontally inhomogeneous, time dependent ocean. *IEEE Journal of Oceanic Engineering*, *31* (2), 384–401.
57. Goff J. A., B. J. Kraft, L. A. Mayer, S. G. Schock, C. K. Sommerfield, H. C. Olson, S. P. S. Gulick, and S. Nordfjord, (2004) "Seabed characterization on the New Jersey middle and outer shelf: Correlatability and spatial variability of seafloor sediment properties," Mar. Geol. **209**, 147–172.
58. Harrison C. H., "Acoustic shadow zones in the horizontal plane," J. Acoust. Soc. Am. **65**, 56–61 (1979).
59. Jackson D. R., and D. R. Dowling, (1991) "Phase-conjugation in underwater acoustics," *J. Acoust. Soc. Am.*, vol. 89, pp. 171–181.
60. Ioana, C., Quinquis, A., & Stephan, Y. (2006). Feature extraction from underwater signals using time-frequency warping operators. *IEEE Journal of Oceanic Engineering*, *31*(3), 628-645.
61. Jiang, Y. M., Chapman, N. R., & Gerstoft, P. (2010). Estimation of geoacoustic properties of marine sediment using a hybrid differential evolution inversion method. *IEEE Journal of Oceanic Engineering*, *35*(1), 59-69.

62. Jiang, Y. M., & Chapman, N. R. (2008). Bayesian geoacoustic inversion in a dynamic shallow water environment. *The Journal of the Acoustical Society of America*, *123*(6), EL155-EL161.
63. Kaiser, J., & Schafer, R. (1980). On the use of the I_0-sinh window for spectrum analysis. *IEEE Transactions on Acoustics, Speech, and Signal Processing*, *28*(1), 105–107.
64. Katsnelson, B. G., Grigorev, V., Badiey, M., & Lynch, J. F. (2009). Temporal sound field fluctuations in the presence of internal solitary waves in shallow water. *Journal of the Acoustical Society of America*, *126* (1), EL41–EL48.
65. Katsnelson B., Petnikov V., Lynch J. Fundamentals of shallow water acoustics. – Springer Science & Business Media, 2012.
66. Kim S., G. F. Edelmann, W. A. Kuperman, W. S. Hodgkiss, H. C. Song, and T. Akal, (2001) "Spatial resolution of time-reversal arrays in shallow water," *J. Acoust. Soc. Am.*, vol. 110, pp. 820–829,
67. Korakas A. and F. Sturm, "On the feasibility of a matched-field inversion in a three-dimensional oceanic environment ignoring out-of-plane propagation," IEEE J. Oceanic Eng. **36**, 716–727 (2011).
68. Kraft, B. J., Overeem, I., Holland, C. W., Pratson, L. F., Syvitski, J. P., & Mayer, L. A. (2006). Stratigraphic model predictions of geoacoustic properties. *IEEE Journal of Oceanic Engineering*, *31*(2), 266-283
69. Kuperman W. A., W. S. Hodgkiss, H. C. Song, T. Akal, C. Ferla, and D. R. Jackson, (1998) "Phase conjugation in the ocean: Experimental demonstration of an acoustic time-reversal mirror," *J. Acoust. Soc. Am.*, vol. 103, pp. 25–40, 1998
70. LeBlanc, L. R., & Middleton, F. H. (1980). An underwater acoustic sound velocity data model. *The Journal of the Acoustical Society of America*, *67*(6), 2055-2062.
71. Li F., X. Yang, Y. Zhang, W. Luo, and W. Gan, "Passive ocean acoustic tomography in shallow water," J. Acoust. Soc. Am. **145**(5), 2823-2830 (2019).
72. Lobkis O. I. and R. L. Weaver, (2001)"On the emergence of the Green's function in the correlations of a diffuse field," *J. Acoust. Soc. Am.*, vol. 110, pp. 3011–3017,
73. Lynch, J., & Tang, D. (2008). Overview of Shallow Water 2006 JASA EL Special Issue Papers. *Journal of the Acoustical Society of America*, *124* (3), EL63–EL65.
74. Mason T., Priestley D., & Reeve, D. E. (2007). Monitoring near-shore shingle transport under waves using a passive acoustic technique. *Journal of the Acoustical Society of America*, *122* (2), 737–746.
75. Masunaga, E., Homma, H., Yamazaki, H., Fringer, O. B., Nagai, T., Kitade, Y., & Okayasu, A. (2015). Mixing and sediment resuspension associated with internal bores in a shallow bay. *Continental Shelf Research*, *110*, 85–99.
76. Newhall A. E., T. F. Duda, K. vond der Heydt, J. D. Irish, J. N. Kemp, S. A. Lerner, S. P. Liberatore, Y.T. Lin, J. F. Lynch, A. R. Maffei, A. K. Morozov, Al Shmelev, C. J. Sellers, and W. E. Witzell, "Acoustic and Oceanographic Observations and Configuration Information for the WHOI Moorings from the SW06 Experiment." No. WHOI-2007-04. Woods Hole Oceanographic Institution MA (2007).

77. Ozaktas, H. M., Erkaya, N., & Kutay, M. A. (1996). Effect of fractional Fourier transformation on time-frequency distributions belonging to the Cohen class. *IEEE signal processing letters*, *3*(2), 40-41.
78. Olsthoorn, J., & Stastna, M. (2014). Numerical investigation of internal wave-induced sediment motion: Resuspension versus entrainment. *Geophysical Research Letters*, *41* (8), 2876–2882.
79. Petrov, P. S. (2014, May). A method for single-hydrophone geoacoustic inversion based on the modal group velocities estimation: Application to a waveguide with inhomogeneous bottom relief. In *Proceedings of the International Conference Days on Diffraction 2014* (pp. 186-191). IEEE.
80. Petrut, T., Geay, T., Gervaise, C., Belleudy, P., & Zanker, S. (2018). Passive acoustic measurement of bedload grain size distribution using self-generated noise. *Hydrology and Earth System Sciences*, *22* (1), 767–787.
81. Porter M. B., The KRAKEN Normal Mode Program, La Spezia, Italy (SACLANT Undersea Research Centre SM-245, 1991).
82. Potty G. R., J. H. Miller, J. F. Lynch, and K. B. Smith, (2000) "Tomographic inversion for sediment parameters in shallow water," J. Acoust. Soc. Am. **108**, 973–986.
83. Qin J.-X., B. Katsnelson, O. Godin, and Z.-L. Li, "Geoacoustic inversion using time reversal of ocean noise," Chin. Phys. Lett. **34**(9), 094301 (2017).
84. Rajan S. D. and K. M. Becker, (2010) "Inversion for range-dependent sediment compressional-wave-speed profiles from modal dispersion data," IEEE J. Oceanic Eng. **35**, 43–58.
85. Roux P. and W. A. Kuperman (2005), "Time reversal of ocean noise," *J. Acoust. Soc. Am.*, vol. 117, pp. 131–136, 2005.
86. Roux P., W. A. Kuperman, and NPAL Group, "Extracting coherent wave fronts from acoustic ambient noise in the ocean," J. Acoust. Soc. Am. **116**, 1995–2003 (2004).
87. Roux, P., Sabra, K. G., Kuperman, W. A., & Roux, A. (2005). Ambient noise cross correlation in free space: Theoretical approach. *The Journal of the Acoustical Society of America*, *117*(1), 79-84.
88. Roth, D. L., Brodsky, E. E., Finnegan, N. J., Rickenmann, D., Turowski, J. M., & Badoux, A. (2016). Bed load sediment transport inferred from seismic signals near a river. *Journal of Geophysical Research: Earth Surface*, *121*(4), 725–747. doi:10.1002/2015JF003782.
89. Sabra K. G., P. Roux, and W. A. Kuperman, "Emergence rate of the time-domain Greens function from the ambient noise cross-correlation function," J. Acoust. Soc. Am. **118**, 3524–3531 (2005).
90. Sabra K. G., P. Roux, A. M. Thode, G. L. D'Spain, W. S. Hodgkiss, and W. A. Kuperman, "Using ocean ambient noise for array self-localization and self-synchronization," IEEE J. Oceanic. Eng. **30**, 338–347 (2005).
91. Serebryany, A. N., Furduev, A. V., Aredov, A. A., & Okhrimenko, N. N. (2005). Ambient noise generated by large-amplitude internal waves in the ocean. *Doklady Earth Sciences*, *402* (4), 654–657.

92. Serebryany, A. N., Newhall, A., & Lynch, J. F. (2008a). Observations of noise generated by nonlinear internal waves on the continental shelf during the SW06 experiment. *Journal of the Acoustical Society of America, 123* (5), 3589–3589.
93. Serebryany, A., Lynch, J., & Newhall, A. (2008b). Underwater noise generation by nonlinear internal waves on the Atlantic shelf of USA during the experiment "SHALLOW WATER 2006". *Proceedings of the Russian Acoustical Society*, *9*, 217–227.
94. Siderius M, Harrison C. and Porter M. (2006) A passive fathometer technique for imaging seabed layering using ambient noiseJ. Acoust. Soc. Am. V.120, P. 1315
95. Simmen, J., Flatté, S. M., & Wang, G. Y. (1997). Wavefront folding, chaos, and diffraction for sound propagation through ocean internal waves. *Journal of the Acoustical Society of America*, *102*(1), 239–255.
96. Stastna, M., & Lamb, K. G. (2008). Sediment resuspension mechanisms associated with internal waves in coastal waters. *Journal of Geophysical Research: Oceans*, *113*(C10), C10016.
97. Strasberg, M. (1979). Nonacoustic noise interference in measurements of infrasonic ambient noise. *Journal of the Acoustical Society of America*, **66**(5), 1487–1493.
98. S. N. Sergeev, A. S. Shurup, O. A. Godin, A. I. Vedenev, V. V. Goncharov, P. Yu. Mukhanov, N. A. Zabotin, and M. G. Brown, "Separation of acoustic normal modes in the Florida Straits using noise interferometry," Acoust. Phys. **63**, 76–85 (2017).
99. Shapiro, N. M., Campillo, M., Stehly, L., & Ritzwoller, M. H. (2005). High-resolution surface-wave tomography from ambient seismic noise. *Science*, *307*(5715), 1615-1618.
100. Tan T., O. A. Godin, M. G. Brown, and N. A. Zabotin, "Characterizing the seabed in the Straits of Florida by using acoustic noise interferometry and time warping," J. Acoust. Soc. Am., submitted (2019).
101. Tan, T., Godin, O. A., Lefebvre, A., Beaute, W., Katsnelson, B. G., & Yarina, M. (2018, November). Characterizing the seabed by using noise interferometry and time warping. In *Proceedings of Meetings on Acoustics 176ASA* (Vol. 35, No. 1, p. 070001). ASA.
102. Tang, D., Moum, J. N., Lynch, J. F., Abbot, P., Chapman, R., Dahl, P. H., Duda, T. F., Gawarkiewicz, G., Glenn, S., Goff, J. A., Graber, H., Kemp, J., Maffei, A., Nash, J. D., & Newhall, A. (2007). Shallow Water '06: A joint acoustic propagation/nonlinear internal wave physics experiment. *Oceanography*, *20*(4), 156–167. https://doi.org/10.5670/oceanog.2007.16.
103. Thorne, P. D. (1986). Laboratory and marine measurements on the acoustic detection of sediment transport. *Journal of the Acoustical Society of America, 80*(3), 899–910.
104. Thorne, P. D. (2014). An overview of underwater sound generated by interparticle collisions and its application to the measurements of coarse sediment bedload transport. *Earth Surface Dynamics*, *2* (2), 531–543.
105. Thorne, P. D., & Foden, D. J. (1988). Generation of underwater sound by colliding spheres. *Journal of the Acoustical Society of America*, *84*, 2144–2152.

106. Twaroch, T., & Hlawatsch, F. (1998). Modulation and warping operators in joint signal analysis. In *Proceedings of the IEEE-SP International Symposium on Time-Frequency and Time-Scale Analysis (Cat. No. 98TH8380)* (pp. 9-12). IEEE.

107. Thode, A., Bonnel, J., Thieury, M., Fagan, A., Verlinden, C., Wright, D., ... & Crance, J. (2017). Using nonlinear time warping to estimate North Pacific right whale calling depths in the Bering Sea. *The Journal of the Acoustical Society of America*, *141*(5), 3059-3069.

108. Tolstoy, A., Chapman, N. R., & Brooke, G. (1998). Workshop'97: Benchmarking for geoacoustic inversion in shallow water. *Journal of Computational Acoustics*, *6*(01n02), 1-28.

109. Voulgarist, G., Workman, M., & Collins, M. (1999). Measurement techniques of shingle transport in the nearshore zone. *Journal of Coastal Research,15*(4), 1030–1039.

110. Wan L., M. Badiey, and D. P. Knobles, "Geoacoustic inversion using low frequency broadband acoustic measurements from L-shaped arrays in the Shallow Water 2006 Experiment," J. Acoust. Soc. Am. **140**(4), 2358–2373 (2016).

111. Wang, Y., & Zhao, X. F. (2019). Theoretical framework for geoacoustic inversion by adjoint method. *Chinese Physics B*, *28*(10), 104301.

112. Wang, D., Zhang, L., Bao, C., Ma, S., & Wang, Y. (2019, June). A Comparative Study for Shallow Water Match-field Inversion Using Surrogate Models. In *OCEANS 2019-Marseille* (pp. 1-6). IEEE

113. Wapenaar K. (2004), "Retrieving the elastodynamic Green's function of an arbitrary inhomogeneous medium by cross correlation," *Phys. Rev. Lett.*, vol. 93, 254301.

114. Weaver, R. L., & Lobkis, O. I. (2001). Ultrasonics without a source: Thermal fluctuation correlations at MHz frequencies. *Physical Review Letters*, *87*(13), 134301.

115. Weaver, R. L., & Lobkis, O. I. (2004). Diffuse fields in open systems and the emergence of the Green's function (L). *The Journal of the Acoustical Society of America*, *116*(5), 2731-2734.

116. Webb, S. C. (1988). Long-period acoustic and seismic measurements and ocean floor currents. *IEEE Journal of Oceanic Engineering*, *13* (4), 263–270.

117. Wenz, G. M. (1962). Acoustic ambient noise in the ocean: spectra and sources. *Journal of the Acoustical Society of America*, *34* (12), 1936–1956.

118. Weinberg H. and R. Burridge, "Horizontal ray theory for ocean acoustics," J. Acoust. Soc. Am. **55**, 63–79 (1974).

119. Woolfe K. F., S. Lani, K. G. Sabra, and W. A. Kuperman, (2015) "Monitoring deep-ocean temperatures using acoustic ambient noise," Geophys. Res. Lett. **42**, 2878–2884.

120. Xu, L., Yang, K., & Yang, Q. (2019). Geoacoustic Inversion Using Physical–Statistical Bottom Reverberation Model in the Deep Ocean. *Acoustics Australia*, 1-9.

121. Xue, J., Graber, H. C., Romeiser, R, & Lund, B. (2014). Understanding internal wave-wave interaction patterns observed in satellite images of the Mid-Atlantic Bight. *IEEE Transaction on Geoscience and Remote Sensing, 52* (6), 3211–3219.

122. Yang T. C., (2003) "Temporal resolutions of time-reversal and passive-phase conjugation for underwater acoustic communications," *IEEE J. Ocean. Eng.*, vol. 28, pp. 229–245.

123. Zang, X., Brown, M. G., & Godin, O. A. (2015). Waveform modeling and inversion of ambient noise cross-correlation functions in a coastal ocean environment. *The Journal of the Acoustical Society of America*, *138*(3), 1325-1333

124. Zhou, J. X., Zhang, X. S., & Rogers, P. (1991). Resonant interaction of sound waves with internal solitons in the coastal zone. *Journal of the Acoustical Society of America*, *90*(4), 2042–2054.

125. Zverev V. A., P. I. Korotin, and A. A. Stromkov (2008) , "Numerical time reversal of waves," *Acoust. Phys*., vol. 54, pp. 58–64.

REPORT DOCUMENTATION PAGE

Form Approved
OMB No. 0704-0188

1. REPORT DATE *(DD-MM-YYYY)*	2. REPORT TYPE	3. DATES COVERED *(From - To)*
07/23/2020	Final	4/28/2016-04/27/2020

4. TITLE AND SUBTITLE
Single-Element Passive Time Reversal Mirror in Shallow Water Acoustics

5a. CONTRACT NUMBER

5b. GRANT NUMBER
N62909-16-1-2079

5c. PROGRAM ELEMENT NUMBER

6. AUTHOR(S)
Boris Katsnelson

5d. PROJECT NUMBER

5e. TASK NUMBER

5f. WORK UNIT NUMBER

7. PERFORMING ORGANIZATION NAME(S) AND ADDRESS(ES)
ve, 199, Haifa, 3498838, Israel

8. PERFORMING ORGANIZATION REPORT NUMBER

9. SPONSORING/MONITORING AGENCY NAME(S) AND ADDRESS(ES)
Office of Naval Research Global
86 Blenheim Crescent
Ruislip MX HA4 7HB
United Kingdom

10. SPONSOR/MONITOR'S ACRONYM(S)
ONRG/NICOP

11. SPONSOR/MONITOR'S REPORT NUMBER(S)

12. DISTRIBUTION/AVAILABILITY STATEMENT
Approved for public release; Distribution without limitations

13. SUPPLEMENTARY NOTES

14. ABSTRACT
This project investigates a new approaches (Time reversal Mirror and Warping transform) for analysis of cross correlation functions of the noise field is shallow water, and for geoacoustic inversion. Data of experiment SW06 are used, results of inversion are reasonable and give good agreement with other data where comparison is possible. In experiment SW06 anomalously strong noise signals (moise burst) were registered, initiated by sediment saltation due to nonlinear internal waves (NIW trains).

15. SUBJECT TERMS
ambient sound/noise, noise cross correlation function, time reversal mirror, warping transform, geoacoustic inversion, shallow wate

16. SECURITY CLASSIFICATION OF:			17. LIMITATION OF ABSTRACT	18. NUMBER OF PAGES	19a. NAME OF RESPONSIBLE PERSON
a. REPORT	b. ABSTRACT	c. THIS PAGE			19b. TELEPHONE NUMBER *(Include area code)*